

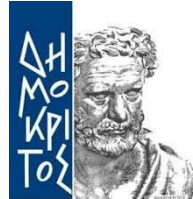


National Technical
University of Athens
School of Applied
Mathematical and Physical
Sciences
School of Mechanical
Engineering

NCSR “DEMOKRITOS”

Institute of Nuclear and
Particle Physics

Institute of Nanoscience
and Nanotechnology



Interdepartmental MSc “Physics and Technological Applications”

Semiconductor Detector Study for Detecting Fusion Neutrons using Geant4 Simulations

MASTER THESIS
of Kalliopi Kaperoni

Supervisor: Maria Diakaki

Athens, June 2022

Περίληψη

Οι ακριβείς μελέτες νετρονίων σε αντιδραστήρες σύντηξης είναι απαραίτητες ώστε να καθοριστεί η εξέλιξη της αντίδρασης καθώς και θέματα ασφαλείας. Οι ακραίες περιβαλλοντικές συνθήκες ενός τέτοιου αντιδραστήρα, όπως ο πειραματικός αντιδραστήρας ITER που αναπτύσσεται αυτή τη στιγμή, απαιτούν ανθεκτικά διαγνωστικά συστήματα τα οποία να αντέχουν τις υψηλές ροές ακτινοβολίας, θερμοκρασίες μέχρι 340°C και ισχυρά μαγνητικά πεδία. Πολλά διαγνωστικά συστήματα έχουν προταθεί για να εγκατασταθούν σε ένα τέτοιο αντιδραστήρα και ένα από αυτά είναι οι ανιχνευτές ημιαγωγών νετρονίων, οι οποίοι επιδεικνύουν πολλά υποσχόμενα χαρακτηριστικά ως αναφορά την λειτουργία τους σε τέτοιες συνθήκες. Το πυρίτιο Si, το διαμάντι (C) και το SiC αποτελούν τα πιο μελετημένα και αναμενόμενα υλικά για την κατασκευή ανιχνευτών με υψηλή απόδοση και ανθεκτικότητα στην ακτινοβόληση. Ο αντιδραστήρας ITER αναμένεται να λειτουργήσει με καύσιμο D-D για το προσεχές μέλλον, έτσι η ανίχνευση 2.45MeV νετρονίων με κατάλληλους ανιχνευτές είναι υψηλής και άμεσης σημασίας.

Στην παρούσα εργασία έγινε η μελέτη της αλληλεπίδρασης των νετρονίων ενέργειας 2.45MeV με ανιχνευτές πυριτίου διαμαντιού και SiC, χρησιμοποιώντας προσομοιώσεις GEANT4, με σκοπό να συγκριθεί η συνάρτηση απόκρισης τους. Μια πειραματική μελέτη θα ακολουθήσει στην εγκατάσταση παραγωγής νετρονίων του επιταχυντή TANDEM στο Ι.Π.Σ.Φ του ΕΚΕΦΕ "Δημόκριτος", με ανιχνευτές που θα προμηθευτούν από την κατασκευαστική εταιρία CIVIDEC GmbH, οπότε η γεωμετρία των προσομοιώσεων χτίστηκε ανάλογα. Με σκοπό να γίνει η σωστή αναπαράσταση της απόκρισης των ανιχνευτών, η δέσμη νετρονίων πρέπει να είναι όσο πιο ρεαλιστική γίνεται. Στο πείραμα τα νετρόνια θα παραχθούν μέσω αντιδράσεων $^3\text{H}(p, n)$ σε έναν στόχο TiT παράγοντας μια ημιμονοεργειακή δέσμη νετρονίων 2.45MeV. Λόγω της χαμηλής ενεργού διατομής της αντίδρασης εφαρμόστηκαν μεροληπτικές τεχνικές στην προσομοίωση ώστε να αυξηθεί ο αριθμός των γεγονότων και έτσι να παραχθεί μια ρεαλιστική δέσμη νετρονίων. Όταν αυτή η δέσμη αλληλεπιδρά με το επιλεγμένο υλικό του ανιχνευτή η στατιστική συνεχίζει να είναι εξαιρετικά χαμηλή έτσι υπήρχε μεγάλη ανάγκη για εφαρμογή περαιτέρω μεροληπτικών τεχνικών στα δευτερογενή νετρόνια στον όγκο του ανιχνευτή. Η εφαρμογή αυτών των τεχνικών και στην παραγωγή και στην ανίχνευση νετρονίων προσθέτει ένα συστηματικό σφάλμα στα τελικά φάσματα και αποκλίσεις από την αναλογική περίπτωση. Πραγματοποιήθηκε μια πληθώρα από ελέγχους για την επιλογή του κατάλληλου πολλαπλασιαστικού παράγοντα στα πρωτόνια και στα νετρόνια, περιορίζοντας την απόκλιση στα 15%. Τέλος παρουσιάζεται η απόδοση και η συνάρτηση απόκρισης για τον ανιχνευτή με C και SiC. Οι έλεγχοι που πραγματοποιήθηκαν, οι παράμετροι που επηρεάζουν τον πολλαπλασιαστικό παράγοντα καθώς και τα κύρια αποτελέσματα και οι μελλοντικές προοπτικές θα παρουσιαστούν και θα συζητηθούν.

Abstract

Accurate measurements of neutrons in fusion reactors are essential, in order to determine the feasibility and progress of the reaction as well as safety issues. The extreme environmental conditions of such a reactor, like the International Thermonuclear Experimental Reactor (ITER), which is developed at the moment, require resilient diagnostic systems, withstanding high radiation fluxes, temperatures up to 340°C and strong magnetic fields. A number of diagnostic systems are proposed to be installed in such a facility, one of which is based on the semiconductor neutron detectors which exhibit promising characteristics for operation in such conditions. Silicon, Diamond and Silicon Carbide are the most studied and anticipated materials for constructing detectors with high efficiency and irradiation resistance. The ITER fusion reactor is expected to run D-D plasma measurements in the near future, so the detection of 2.45MeV neutrons with appropriate detectors is of great and immediate importance.

In the present work the study of the interaction of 2.45MeV neutrons interactions with a silicon, diamond and silicon carbide detector was made, using GEANT4 simulations, in order to compare their response function. An experimental study will follow at the neutron production facility of the TANDEM accelerator of the I.N.P.P. of the NCSR “Demokritos”, with detectors provided by CIVIDEC Instrumentation GmbH, so the geometry of the simulations was built accordingly. In order to properly simulate the detector responses, the neutron beam needs to be as realistic as possible. For the experiment the neutrons will be produced via ${}^3\text{H}(p, n)$ reactions in a TiT target producing a quasi-monoenergetic neutron beam of 2.45MeV. Due to the low cross section of the reaction, biasing techniques were implemented in the simulation to increase the counting rate and thus producing a realistic neutron beam. When this beam interacts with the chosen detector material, the statistics continue to be extremely low, so the need arose for further biasing the secondary neutron particles inside each detector. Implementing biasing techniques both in neutron production and detection adds a systematic error to the resulting spectra and a deviation from the unbiased case. Various tests for choosing the suitable biasing factor were performed both in proton and neutron biasing confining the deviation at mostly 15%. Finally the efficiency and the response function for the C, SiC detector is presented. The performed tests, the parameters affecting the choice of biasing factor, the main results and future perspectives will be shown.

Contents

1	Introduction	5
1.1	Motivation	5
1.2	Nuclear Fusion	6
1.3	ITER	10
1.3.1	Neutron Detector Needs for ITER	11
2	Neutron interactions with semiconductor detectors	13
2.1	Semiconductor Neutron Detectors	13
2.2	Diamond Detector	15
2.3	Si Detector	17
2.4	SiC Detector	18
2.5	Neutron interactions	19
2.5.1	Neutron interactions in Diamond	21
2.5.2	Neutron interactions in Si	25
2.5.3	Neutron interactions in SiC	26
3	Simulated detector response to fusion neutrons	29
3.1	The GEANT4 Monte Carlo code	29
3.2	Simulated neutron energy deposition in semiconductor sensors	31
3.2.1	Diamond Detector	31
3.2.2	Silicon Detector	36
3.2.3	Silicon Carbide Detector	39
3.3	Simulated gamma ray energy deposition in semiconductor sensors	41
4	Preparation of experiment at the NCSR “Demokritos”	46
4.1	Experimental setup	46
4.1.1	The neutron beam production	47
4.1.2	The detector setup	50
4.2	Geant4 simulations	51
4.2.1	Biasing Technique	52
4.2.1.1	Biasing the neutron production	54
4.2.1.2	Biasing the neutron detection	59
4.2.1.3	Optimum combined result	68
4.3	Comparison of the sensors’ response	77
5	Conclusions and future perspectives	80

Chapter 1

Introduction

In this chapter an introduction to nuclear fusion is made and the International Thermonuclear Experimental Reactor (ITER), which is constructed at the moment is presented. The importance of neutron detection as well as the proposed diagnostics systems to be installed, which will be able to withstand the extreme environmental conditions of fusion are described.

1.1 Motivation

Producing energy through nuclear fusion has been an interesting subject worldwide. The difficulties in producing fusion energy arise from the extremely high temperatures ($10^9 K$ or even higher) and strong magnetic fields which are required for plasma confinement. Experiments have been conducted since the 1950's in order to produce fusion power but with no significant results. However with the technological advances such a reactor is now considered to be possible.

Since 2005 ITER (International Thermonuclear Experimental Reactor), an experimental fusion reactor, is being build in France, in order to produce energy through D-T fusion. For the upcoming years, there will be tests performed in D-D plasma, with the production of 2.45MeV neutrons, whereas at 2035 according to ITER schedule, D-T fusion experiments are going to begin, producing 14MeV neutrons. ITER is aiming to demonstrate the feasibility of nuclear fusion in a reactor-scale tokamak plasma configuration operating with a magnetic field of 5.3T, plasma current of 15MA, pulse duration of 300 to 500s, and production of up to 500 to 700 MW of fusion power.

The only way to measure the efficiency of such reactor is through detecting the fast neutrons produced during the reaction. Therefore, there is a need for constructing special neutron detectors, with increased efficiency and irradiation resistance. One of the numerous diagnostics systems proposed, are semiconductor detectors which exhibit promising characteristics. These detectors need to be operational at the harsh environmental conditions of the fusion reactor, exhibit a high energy resolution and can be produced in a large scale.

Diamond and silicon based semiconductor detectors are often used for neutron appli-

cations. Diamond detectors with their excellent physical and electrical properties are the popular choice when high energy resolution, irradiation resistance and hardness is required. Silicon (Si) being the most dominant semiconductor, used in microelectronics as well as neutron applications, cannot be excluded when a massive detector production is required. Its low production cost and a relatively low Z for gamma-ray moderation, makes it a material of choice in numerous experiments. In addition, over the last decades, there has been a development of a more resistant material than diamond, silicon carbide (SiC). It is used for applications in harsh environmental conditions, with extreme temperatures and intense radiation. Its properties make it able to withstand temperatures even above $400^{\circ}C$.

Consequently, there is a need to study the performance of a Si, diamond and SiC detector in fusion neutrons. The purpose of this thesis is to describe the characteristics of each detector and examine their interactions with 2.45MeV neutrons. Geant4 is the best simulation toolkit for this kind of work. With the recently added neutron libraries, it provides reliable data for a complete and realistic analysis.

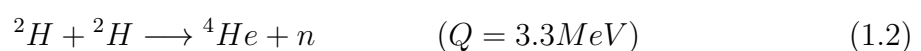
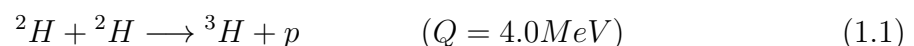
1.2 Nuclear Fusion

Nuclear fusion is the reaction between two light nuclei to form a heavier one, with simultaneous energy release. Fusion powers the sun and other stars and therefore consists one of the most crucial reactions in nuclear physics. Understanding and achieving controlled fusion has been in progress since 1950. Building a nuclear reactor which produces fusion power, is both a technological and physical challenge.

As an energy source nuclear fusion has several advantages such as: Light elements are in abundance and easy to obtain, also fusion products are usually stable and light nuclei, in contrast to heavy and radioactive nuclei which are produced in fission. However there is one considerable disadvantage, before light nuclei can be combined, they need to overcome their Coulomb barrier.

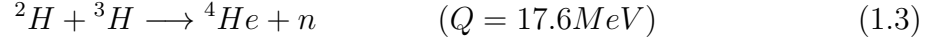
Experimentally the only way to induce nuclear fusion is through heating a gas chamber, until the thermal energy released is large enough, for the probability of two nuclei approaching one another and collide with energy higher than Coulomb barrier to be high. This process is called thermonuclear fusion. Specifically in deuterium (D) tritium (T) fusion the Coulomb barrier is approximately 3.6MeV. For the mean kinetic energy per gas molecule ($\frac{3}{2}kT$) to be equal with the $\frac{1}{2}$ of 3.6MeV an energy of $kT=1.2MeV$ is required. At room temperature $kT=0.025eV$, so this process requires $T=10^9K$. [1]

One of the basic fusion reactions is D-D fusion.



Both reactions have 50% chance of happening. In [1.2](#), where this project focuses, a 2.45 MeV neutron is produced with energy distribution as shown in figure [1.1](#).

An equally and perhaps more important reaction is D-T fusion:



Where a higher energetic neutron of 14MeV is produced with energy distribution as shown in figure 1.2.

The initial kinetic energy of the particles is small (in the range of 1-10keV) compared to the Q value (several MeV), so we can assume that the energy release and the final total energy of the product particles will be equal to the Q value.

$$\frac{1}{2}m_b u_b^2 + \frac{1}{2}m_Y u_Y^2 \simeq Q \quad (1.4)$$

Where b the light particle and Y the heavy one.

Neglecting the initial motions, the final momenta are equal and opposite.

$$m_b u_b \simeq m_Y u_Y \quad (1.5)$$

And thus:

$$\frac{1}{2}m_b u_b^2 \simeq \frac{Q}{1 + \frac{m_b}{m_Y}} \quad (1.6)$$

$$\frac{1}{2}m_Y u_Y^2 \simeq \frac{Q}{1 + \frac{m_Y}{m_b}} \quad (1.7)$$

We can extract that the light particle will take the larger share of the energy.

The ratio of the kinetic energies is:

$$\frac{\frac{1}{2}m_b u_b^2}{\frac{1}{2}m_Y u_Y^2} \simeq \frac{m_Y}{m_b} \quad (1.8)$$

Consequently in D-T fusion the product neutron will have 80% of the total energy and respectively in D-D fusion the 75%. Hence the product neutron is the energy carrier and the only output in those fusion reactions. Analysis and study of these neutrons, can provide evidence about the feasibility and progress of the reaction by giving information about the plasma state.

The essence of controlling fusion reactions and extracting usable energy as mentioned is the heating of the fuel in temperatures of order 10^8 K while simultaneously maintaining a high enough density for a long enough time that the rate of fusion reactions will be large enough to generate the desired power. In such high temperatures the atoms are ionised, so the fuel is not a mixture of positive and negative ions but an electrically neutral plasma. One of the main challenges is the confinement of the plasma for enough time. Tokamak reactors, such as ITER, use magnetic confinement. In a Tokamak system the constant heating of the fuel can be achieved through powerful magnetic fields, which confine the alpha particles and reheat the fuel, until ignition happens and the reaction is self sustained. Until ignition occurs, plasma loses continuous energy through Bremsstrahlung, in which Coulomb scattering of two particles produces an acceleration, which in turn gives rise to the emission of radiation. The largest accelerations are suffered by the electrons, which consequently affect the ions, since they are practically in thermal equilibrium. [1]

Fusion power can be measured in terms of the steady state fusion power gain or the Q factor defined as the ratio of the fusion power output to the input power, (the auxiliary power supplied from outside to sustain the reaction) $Q = P_{output}/P_{input}$. So, for fusion power to be successful the minimum criterion is $Q > 1$. The $Q = 1$ state is called break even condition where the output power equals the auxiliary input power. The record for the Q factor has the JET (Joint European Torus) tokamak reactor in the UK, with $Q = 0.67$. [2]

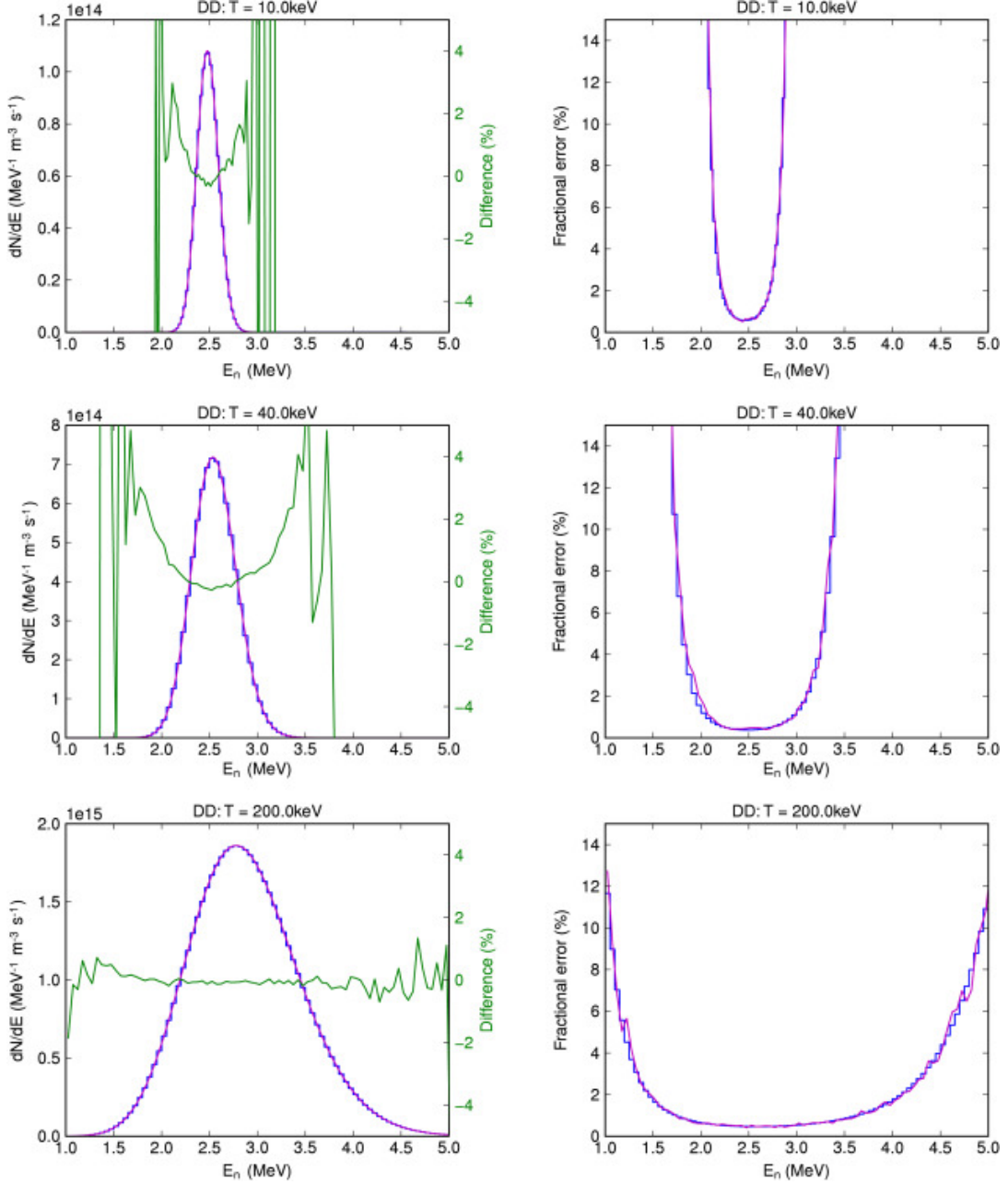


Figure 1.1: Neutron energy spectra of different temperatures, for the DD fusion reaction spectrum. The left column of the figures show a comparison between the average of the DRESS spectra (magenta line) and the analytical result (blue line) as well as the difference between the two spectra (green line). The right column shows a comparison between the average of the Monte-Carlo error and the root mean square of the differences between the analytical spectrum and the DRESS spectra. [3]

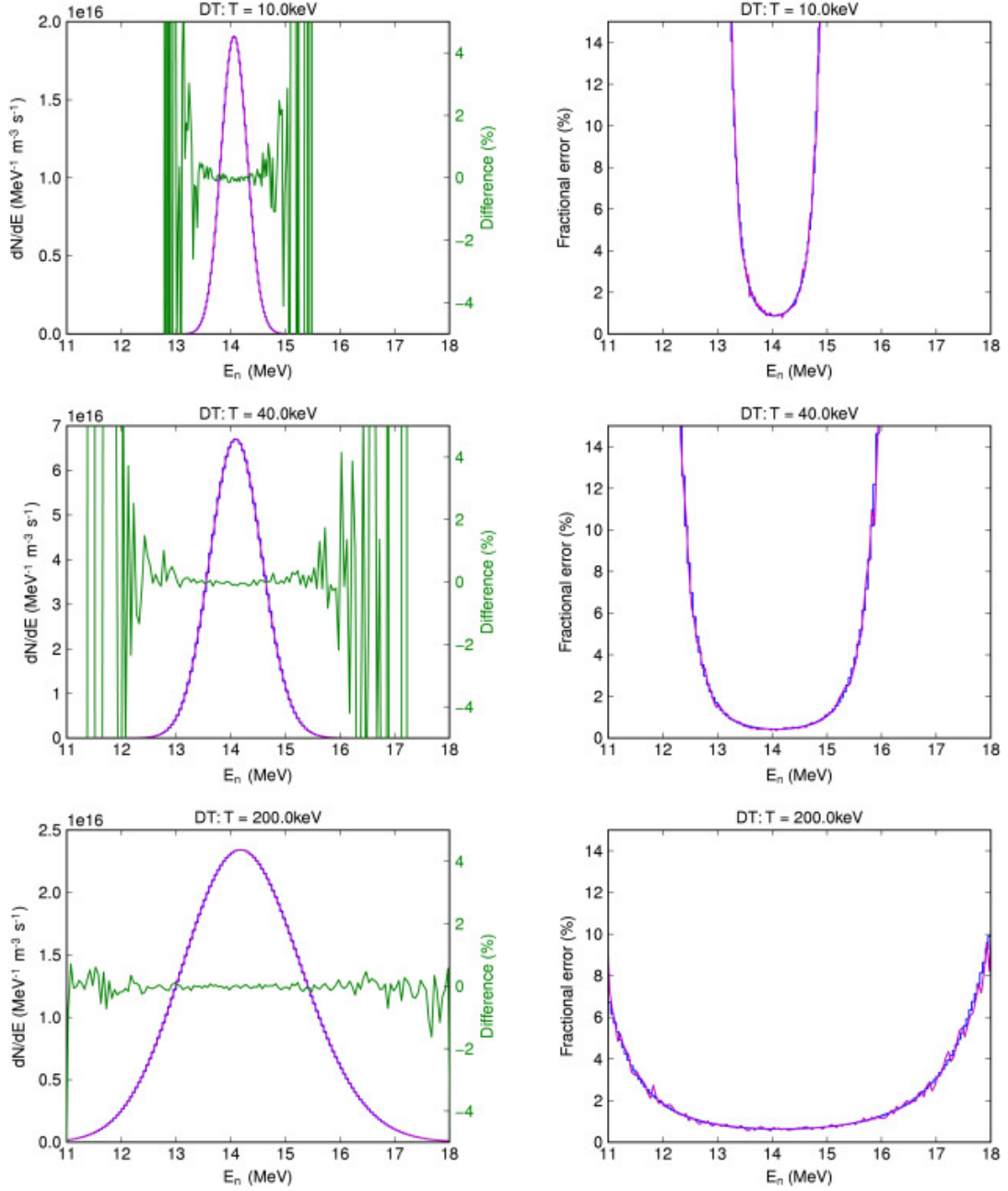


Figure 1.2: Neutron energy spectra of different temperatures, for the DT fusion reaction spectrum. The left column of the figures show a comparison between the average of the DRESS spectra (magenta line) and the analytical result (blue line) as well as the difference between the two spectra (green line). The right column shows a comparison between the average of the Monte-Carlo error and the root mean square of the differences between the analytical spectrum and the DRESS spectra. [3]

As previously mentioned neutrons carry important information about fusion and thus measuring them in a controlled fusion reactor is considered one of the most crucial diagnostics. Neutrons provide information about the estimation of the Q factor, plasma physics, protection and control issues. Since they are neutral particles they can easily escape the tokamak's magnetic fields and be detected by special detectors. Evaluating neutron emissivity delivers information on the alpha birth source which provides data about heating of the plasma and thus the progress of the reaction. In addition, neutron

fluence delivers information on the damage expected on the materials facing the plasma. Another important parameter is the fuel ratio, the quantity nT/nD on the D-T plasma which is measured by neutron spectroscopy and provides the temperature of plasma ions. [4]

At ITER experimental fusion reactor which is presented in the next section, various neutron diagnostics systems are to be installed in order to measure the parameters mentioned above. The neutron detectors are expected to measure neutron fluence with 10% accuracy, with a temporal resolution of 1ms and spatial resolution of 200mm.

1.3 ITER

The International Thermonuclear Experimental Reactor (ITER), is an international experiment aiming to construct a tokamak fusion reactor, taking place at the south of France. The construction of ITER started in 2014 and until 2025 D-D fusion experiments will be conducted. The first D-T plasma operations, according to ITER official schedule, are to begin in 2035. The reactor is being built by seven country members (China, European Union, India, Japan, Korea, Russia, and the United States) and its gain is to produce $Q \geq 10$. It will be the largest fusion machine, with major radius of 6.2m and minor radius of 2.0m, operating in a magnetic field of 5.3T, plasma current of 15MA. The ultimate goal is the production of 500-700MW fusion power. [5]

As mentioned in 1.2 neutron flux measurements in a fusion reactor provide crucial information. So, approximately over 40 diagnostic systems are to be installed at ITER as shown in figure 1.3 , to perform various measurements, which are essential for monitoring all the stages of the reactor.

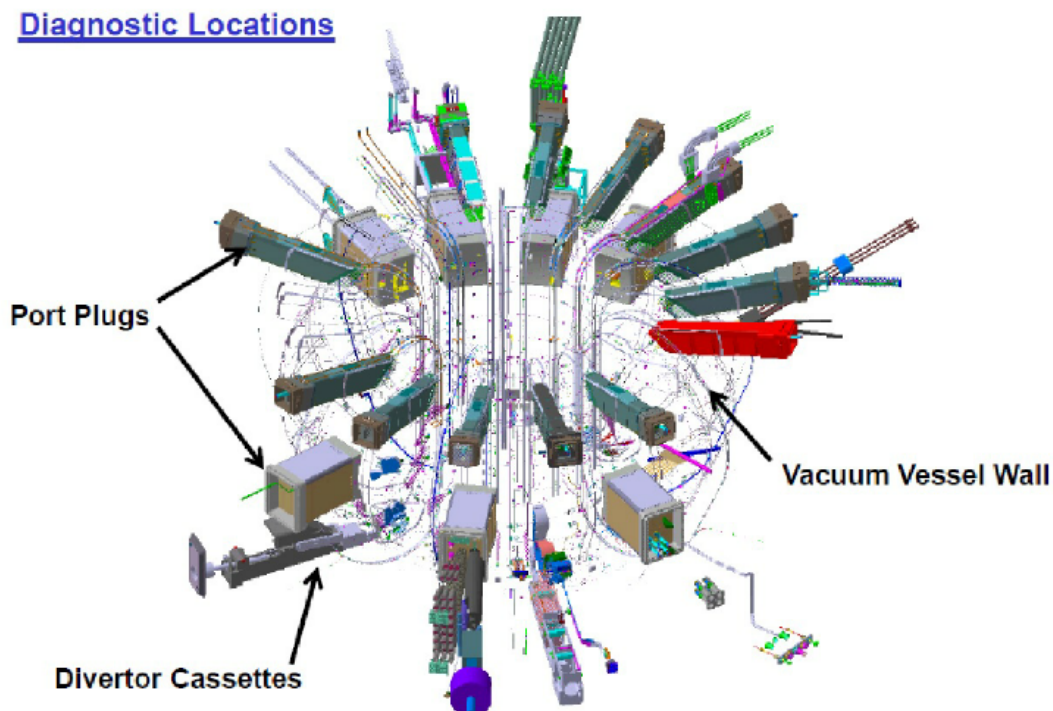


Figure 1.3: Diagnostics locations on ITER [4]

These diagnostic systems will have to withstand: High neutron flux (up to $10^{14}n/cm^2$ with 14MeV neutrons, for D-T fusion), high temperatures due to plasma irradiation, magnetic fields up to 6T as well as electromagnetic noise due to auxiliary radiofrequency heating systems. More analytically, during ITER's full power discharges, $10^{21}n/cm^2$ fusion neutrons per second will be produced with fluxes up to $10^9 - 10^{14}n/cm^2$ in the locations of different sensors. A large number of detectors will be placed in the vacuum vessel and in the port plugs which will be constantly held at temperatures from $70^\circ C$ to $100^\circ C$. During shutdown periods, the vacuum vessel will be baked for tritium removal in temperatures $200^\circ C$ and the divertor at $340^\circ C$. Neutron detectors in these areas will typically need to survive vacuum vessel baking. No maintenance is foreseen for these detectors for the whole ITER life cycle, so there is a great need for resilient materials able to withstand these harsh environmental conditions. Table 1.1 summarises these environmental conditions for every diagnostic system, whereas table 1.2 shows the neutron measurement each diagnostic will perform. [5]

1.3.1 Neutron Detector Needs for ITER

At ITER seven neutron diagnostics sub systems will be installed in different parts of the reactor, in order to provide multiple measurements. These diagnostics are: [4]

1. Radial neutron camera, RNC
2. Vertical neutron camera, VNC
3. Microfission chambers, MFC
4. Neutron flux monitor, NFM
5. Divertor neutron flux monitor, DNFMs
6. Neutron activation system, NAS
7. High-resolution neutron spectrometer, HRNS

The last two detection systems will not be exposed to high temperatures, magnetic fields, and radiation fluxes. The remaining neutron diagnostics will have (some or all) detectors installed inside the ITER vacuum vessel or port plugs. These detector will face severe environmental conditions in terms of both radiation and temperature as shown in 1.1. Development of such detectors is a technological challenge.

Diagnostic System	Neutron Flux ($n \cdot cm^{-2} \cdot s^{-1}$)	Operating Temperature $^\circ C$	Baking Temperature $^\circ C$	Magnetic Field in Normal Operation (T)
RNC (in-port)	10^{11}	70	240	0.5
RNC (ex-port)	10^8	40	-	0.1
VNC	10^{10}	70	240	1.5
MFC	10^{13}	70	240	4
NFM(in-port)	10^9	70	240	1
DNFM(in-port)	10^{14}	70	340	4

Table 1.1: Predictions of environmental conditions at ITER [5].

Diagnostic	Parameter
Radial neutron camera	Neutron/alpha source profile Total neutron source strength Ion temperature profile Fuel ratio Neutron fluence on first wall
Vertical neutron camera	Neutron/alpha source profile Total neutron source strength Ion temperature profile Fuel ratio Neutron fluence on first wall
Microfission chambers	Total neutron source strength Neutron fluence on first wall
Neutron flux monitor	Total neutron source strength Neutron fluence on first wall
Neutron activation system	Total neutron source strength Neutron fluence on first wall
High-resolution neutron spectrometer	Plasma Core Ion temperature Core Plasma Fuel Ratio
Divertor neutron flux monitor	Total neutron source strength Neutron fluence on the Divertor

Table 1.2: ITER neutron diagnostics and related neutron parameters [4].

Semiconductor detectors will be utilised in the radial neutron camera diagnostics. Silicon (Si), germanium (Ge), diamond, and other similar materials have been proposed for neutron measurements. Among them, diamond shows increased radiation hardness, which is a crucial parameter for ITER conditions and provides the ability to distinguish deuterium-tritium neutrons and determine their energy distribution. At the moment, almost 100 diamond detectors with dimensions 4x4x0.5mm are manufactured to be installed in various ITER locations. However, research for the most suitable material in terms of both efficiency and hardness is open.

In this work semiconductor detectors based on diamond (C), Si and SiC technology were studied, in order to compare their response to D-D fusion neutrons (2.45MeV). In the next chapters a description of these detectors is made as well as an overview of their interactions with neutrons. Next, a presentation of the Geant4 simulation toolkit is made, as well as the experimental set-up, followed by the numerous tests performed and the results.

Chapter 2

Neutron interactions with semiconductor detectors

In this chapter semiconductor detectors and their interactions with neutrons are analysed. First some basic properties of semiconductor detectors are presented, followed by an introduction to diamond, silicon and silicon carbide detectors, along with their characteristics. Finally the neutron interactions with each detector material are presented analytically with their corresponding energy deposition spectra deriving from theoretical or experimental studies, so the bibliography for future references is established.

2.1 Semiconductor Neutron Detectors

Semiconductor detectors are most commonly used when excellent energy resolution is required. Their unique characteristics are making them proper candidates for various environments and applications. Semiconductor's density is high so they have a large stopping power. As a result, they are able to collect the charge particles by the radiation in much smaller volumes than those needed by scintillators or gas detectors. Consequently, they are much smaller in size than the other types of radiation detectors. There are many environments that require the unique characteristics of these detectors, such as small size and weight, compactness, low battery consumption as well as their fast response.

The fundamental physical process in a semiconductor detector is the electron-hole pairs created by primary or secondary particles. The ionisation energy for one electron-hole pair in semiconductors is only about one-tenth of the analogous values for gas ion chambers, hence approximately 10 times more ionisation occurs in semiconductor devices than in ion chambers for the same energy deposition. The total number of the electron-hole pairs created is proportional to the energy transmitted by the radiation to the semiconductor. The probability per unit time that an electron-hole pair is thermally generated is:

$$P(T) = CT^{3/2} \exp(-E_g/2kT) \quad (2.1)$$

Where T is absolute temperature, E_g is the band gap energy, k is the Boltzmann constant and C is a proportionality constant characteristic of the material.

These e-h pairs induce an image charge on the electrodes that is integrated, resulting in a pulse that is processed by an external preamplifier and its readout electronics, and thus the energy of the incident radiation can be found. To collect these charge carriers an electric field must exist. The applied high voltage varies depending on the detector size and is typically hundreds or thousands of volts. This high voltage induces leakage current even in the absence of radiation because the semiconductor material itself has a finite conductivity. In order to reduce this leakage current, which translates in electromagnetic noise, a p-n junction method is implemented to pickup the signal corresponding to the radiation interaction, so the detector is practically a semiconductor diode. [6]

Despite the fact that semiconductor detectors were constructed for charge particle detection, in the recent years prototypes for neutron detection are developed. Neutron detectors play a crucial role in many applications, where neutron spectrum measurements and flux monitor are important, especially in high energy experiments and fusion facilities, for plasma diagnostics. Neutrons, being neutral particles, can be detected only by secondary particles. Therefore, the modern neutron detectors consist of many layers of different converter materials with high cross sections, so ionising particles are produced, which as mentioned above, consist the detector signal. Typically, the neutron converter is placed directly on to the semiconductor to increase efficiency and decrease energy attenuation of the reaction products. [7]. Another way for neutron detection is by using the detector itself as a conversion. The recoil nucleus produced usually by fast neutron scattering, ionises the surrounding material and the charge carriers are collected. In all of these detectors especially in microstructured electronics, metallization layers are required. These metal films are deposited to the detector and used as electrodes, providing a good electric contact. [8], [9]

Over the last years neutron semiconductor based detectors receive considerable attention due to their low operating voltage, high energy resolution and radiation resistance. One of their main disadvantage, especially in neutron detection, is that due to their high density, interactions with g-rays is favoured. Therefore, an ideal semiconductor candidate must have a high γ -rejection rate, ability to discriminate neutrons from gamma rays, fast response and resistant to high temperatures and extreme radiation conditions. [10]

Independent of which semiconductor material is employed, specific material properties are required to achieve high energy resolution, and high efficiency for both high temperatures and intense radiation environments. Some of them are: [11]

- Large bandgap energy for achieving very low leakage current.
- Small enough electron-hole pair generation energy ϵ , to ensure that the number of electron-hole pairs generated by a given ionising radiation is reasonably large for a higher signal-to-noise ratio.
- Low dielectric constant. This allows us to operate with a lower detector capacitance, for better energy resolution.
- High-purity, homogeneous, single-crystal, defect-free materials, to ensure full charge collection, low leakage current and better energy resolution.
- High atomic displacement energy. Damages to the crystalline lattice induced by

the radiation can cause incomplete charge collection and thus worsen the energy resolution, especially when the defects are generated by heavy charged particles or neutrons.

- High thermal conductivity. One of the approaches to increase the radiation hardness, is to cool down the detector itself. This requires the use of materials with good cooling properties. Moreover, a high thermal conductivity is useful to easily control the operating temperature.
- High breakdown field. This property affects the electrical properties of the semiconductor. Breakdown voltage defines the largest reverse voltage that can be applied without causing an exponential increase in the leakage current in the diode.

There is a number of materials proposed that have these properties. One of the most studied and widespread is diamond (see section 2.2). Its outstanding electrical properties provide a very high energy resolution, fast response as well as radiation and temperature resistance up to $200^{\circ}C$. As mentioned in 1.3 diamond detectors are proposed to be used at ITER since they exhibit the most promising characteristics.

An equally popular material is silicon (Si) (see section 2.3). The low production cost and a high technological know-how makes it a material of choice as an active detector. However in order to ensure a good neutron-gamma ray discrimination, a low thickness of the active sensor is necessary. In the usual parallel plate geometry for silicon detectors, such a low thickness comes usually at the expense of a high capacitance and therefore large electronic noise. So, ultra thin silicon detectors of $10\mu m$ thick with low capacitance are required in order to detect neutrons, which brings many technological and practical inconveniences. Also in contrast to diamond, its low hardness makes it unable to withstand harsh environmental conditions. [12]

A less known material for neutron detection is silicon carbide (SiC) (see section 2.4). These detectors were developed in the recent decades, for high-temperatures and harsh radiation conditions under which conventional semiconductor detectors are unable to perform. The reasoning behind investing in SiC technology lies within the excellent material properties deriving from the high strength of the Si-C bond. Studies have shown it can withstand temperature up to $700^{\circ}C$ [13], which makes it a perfect candidate for the harsh environmental conditions on fusion facilities.

From the discussion above it is clear that we need to perform extensive research for the material choice for semiconductor neutron detectors. In the next sections an analytical review of the diamond, Si and SiC detector is presented, as well as their interactions with neutrons (see section 2.5).

2.2 Diamond Detector

Diamond is made of the element Carbon with an atomic number $Z = 6$. Two stable isotopes of Carbon can be found in nature, ^{12}C and ^{13}C , where the natural abundance of ^{13}C is only 1.1 % ($\rho_C \sim 2g/cm^3$). The crystallization of Carbon atoms in a face-centered cubic (fcc) lattice, with two atoms at each lattice point, one at $[0,0,0]$ and the other at $[\frac{1}{4}, \frac{1}{4}, \frac{1}{4}]$ is classified as diamond. It exhibits the highest density of any matter on Earth, calculated to $3.52g/cm^3$. Its excellent electrical and physical properties make

it suitable for detector applications, in harsh environmental conditions. Its properties are summarised in table **2.1** and explained below.

At room temperatures diamond presents a bandgap $E_g = (5.470 \pm 0.05) \text{ eV}$ while common semiconductor detectors like Si or Ge exhibit a gap of 1.12 eV and 0.66 eV respectively. In the presence of an electric field, thermal generation of electron-hole pairs according to equation **2.1** generate a current known as dark or leakage current. The leakage current of the diamond detector is much lower than Si or Ge detectors, due to a smaller value of E_g and the high resistivity ($> 10^{13} \text{ Wcm}$) that diamond presents. The high electron and hole mobility and the high breakdown field (10 MVcm^{-1}), lead to a possibility of fast timing measurements with diamond detectors with subnanosecond response time. [14], [15]

The dielectric constant of diamond is $\epsilon=5.7$, which reflects its low capacitance. This is advantageous for high energy resolution measurements, as the capacitance for a given detector-geometry is lower than for most other semiconductor materials, like Si with $\epsilon = 11.9$. Also, from theoretical calculations, the energy to create an electron-hole pair in diamond is predicted to be $\epsilon = 11.6 \text{ eV/e-h}$ (this value varies according to different studies and is obviously dependent from the type of diamond detector used). A low dielectric constant combined with a high E_g as well as a relatively small electron-hole pair generation energy, leads to a high signal to noise ratio in favour of the diamond detector.

The C atoms in diamond are strongly bound to each other with 7.24 eV/bond respectively. The exceptional thermal conductivity of up to $20 \text{ Wcm}^{-1} \text{ K}^{-1}$ and the relatively high displacement energy threshold of approximately 43 eV/atom derive from these strong bonds. The latter contributes to diamond's good radiation hardness. A high fusion temperature (4100°C) combined with the high thermal conductivity, make diamond suited for operations with high temperatures. The low Z renders diamond scarcely sensitive to gamma radiation. This could be helpful when operating in mixed neutron-gamma fields, much like the conditions in high energy experiments or fusion reactors, in order to enhance and/or separate the neutron signals.

Natural diamond is quite rare and expensive, however it was used even for neutron detection applications, since 1941. Due to the high cost and the large differences in the responses, caused by the large variation of impurities, the interest has moved in artificial diamond detectors. Two types of artificial diamond are available nowadays, high pressure high temperature (HPHT) diamond and chemical vapour deposition (CVD) diamond. [15]

1. The HPHT technology essentially emulates the extreme pressure and temperature conditions, which lead to the formation of natural diamonds. As the name suggests graphite is converted into diamond in an environment of $1500 - 2000^\circ \text{C}$ and 50 - 100 kbar. The first artificial diamond was synthesised with this method in the 1950s. The diamonds resulting from this technique are in general not suited as material for detector applications, due to the high density of the crystal defects.
2. CVD technology was first performed in the beginning of 1960s. It does not require high pressure, the production is done at lower temperatures and it allows to grow diamond on a suitable seed. The principle of this method is based on chemical reactions occurring in a gas phase above a solid surface and consequently deposition

of material onto this surface. A gaseous mix of hydrogen and hydrocarbon are injected into a deposition chamber. The reactants are activated and free ions are produced. The diamond substrate introduced to the deposition chamber undergoes several chemical reactions producing the desired chemical composition [16]. If diamond is used as a seed for CVD growth, there are two categories according to the crystal synthesis.

- For the synthesis of poly-crystalline chemical vapour deposition (pCVD) material, diamond nano-crystals or poly-crystalline diamond are used as substrate. It is mainly used for detector tracking, however it is not suited for spectroscopic applications.
- For the synthesis of high quality single-crystal, chemical vapour deposition (sCVD) technique is used. The substrate used is usually a surface-treated HPHT diamond. High quality electronic grade diamonds are nowadays grown in this way.

2.3 Si Detector

Silicon is the element with an atomic number $Z = 14$, density $\rho = 2.329 \text{ g/cm}^3$ and it consists of 92.2 % ^{28}Si , 4.6 % ^{29}Si and approximately 3 % ^{30}Si . It is an abundant element found in the Earth's crust in various compounds. If a mass production for detectors which have uniform characteristics for a low production cost is desired, silicon is the ideal candidate. Its properties are summarised in table 2.1.

Silicon crystallises into a diamond face centred cubic (fcc) structure, in which the atoms are covalently bonded. Elements such as germanium, typically have the same structure. It has a bandgap of 1.12eV which means that pure silicon at room temperature is almost an insulator (as any other semiconductor) and its resistivity can be varied over a wide range by doping, from $\text{m}\Omega$ to $\text{k}\Omega$. It has a thermal conductivity of $1.5 \text{ W cm}^{-1} \text{ K}^{-1}$ and a high dielectric constant of 11.9. Its displacement energy can vary according to the manufacturing, between approximately 13-20 eV, so with the right polytype it can sustain high fluxes of radiation with reduced damage. However, during the manufacturing and doping of silicon semiconductors, impurities and defects arise. These can affect the electrical and mechanical properties of silicon as well as the detector performance. [17], [18]

Silicon semiconductors are used for various nuclear applications such as neutron detection. Silicon is a preferable material for neutron detection as it provides a relatively low Z for moderate γ -rays interaction probability and above all a high technological know-how thanks to the microelectronics industry based on silicon. One of the most efficient ways to produce a silicon semiconductor is planar technology. They consist of a planar diode detector with thin layer contacts and a layer of converter deposited on the surface. With this technique a high performance detector with reduced leakage current is produced. [7]

2.4 SiC Detector

Silicon Carbide (SiC) is the material build by both Si and C atoms and its density is about $\rho = 3.2g/cm^3$. Semiconductor detectors based on SiC are developed to function in high temperatures and extreme radiation conditions. The reason behind investing in SiC technology lies within the excellent material properties deriving from the high strength of Si-C bond.

As far as the manufacturing of SiC detectors is concerned, there is a large number of different crystal structures built from the same Si-C grouping, organised into diverse stacking sequences, known as polytypes. The most common polytypes of SiC, presently being developed for electronics, are 3C-SiC, 4H-SiC and 6H-SiC, where the numbers respond to the repetition of layers and ‘C’ and ‘H’ stand for cubic and hexagonal lattice, respectively. In table **2.1** the basic properties of the three most common SiC polytypes are presented. Thanks to the better electronic properties and higher energy bandgap, 4H polytype is usually preferred in both electronic devices and detector radiation applications.

All forms of SiC have material advantages such as elevated chemical and radiation tolerance, high thermal conductivity and displacement energy threshold, making it very suitable to operate in extreme environments. The bandgap of 3.23 eV at room temperature in 4H-SiC (Si has only 1.12 eV) considerably diminishes the number of electron-hole pairs resulting from thermal activation across the bandgap, which enables SiC-based electronic devices to operate at temperatures over $400^\circ C$. Studies conducted since 1950’s has shown that the detector is operational at temperatures up to $700^\circ C$ [19].

The high breakdown field ($3MVcm^{-1}$) of 4H-SiC material, permits in principle the detector to work always in the regime of saturated electron and hole drift velocities. When this condition can be coupled with high crystalline quality of the material, a good charge collection and energy resolution can be expected. Its relatively high yield strength (21GPa), which is a material property corresponding to the point at which the material begins to deform plastically without producing permanent deformation, shows a high resiliently.

Property	Si	Diamond	3C-SiC	4H-SiC	6H-SiC
Energy Bandgap (eV)	1.12	5.5	2.39	3.27	3.02
Thermal Conductivity (W/cmK)	1.5	20	3-5	3-5	3-5
Relative Dielectric Constant	11.9	5.5	9.7	9.7	9.7
Yield Strength (GPa)	7	53	21	21	21
Thermal Expansion Coefficient ($^{\circ}C10^{-6}$)	2.6	0.8	3.0	0.8-5.4	4.5
Electron Mobility (cm^2/Vs)	1200	1530 ± 160	750	400	800
Hole Mobility (cm^2/Vs)	420	2660 ± 160	40	90	115
Electron-hole creation energy (eV)	3.6	13	7.78	7.78	7.78
Threshold displacement energy (eV)	13-20	40-50	22-35	22-35	22-35
Chemical Stability	Fair	Fair	Excellent	Excellent	Excellent

Table 2.1: Material Properties of Si, Diamond and SiC basic polytypes. [20], [11]

2.5 Neutron interactions

Neutrons do not interact with Coulomb force since they are not electrically charged. They interact with matter via nuclear forces, as a consequence they are highly penetrating. They interact mainly through scattering (elastic,inelastic), capture (absorption) and fission with heavy nuclei . The neutron scattering involves changing the energy and direction of the incident neutron but the target nucleus remains with the same number of proton and neutrons. When neutron capture occurs the target nucleus absorbs the incident neutron and emits other particles instead. Depending on the neutron energy and the target nucleus one or all the above processes can occur. Neutrons may change significantly their directions or energies, produce charged secondary particles, gamma rays or even disappear completely. Table **2.2** summarises those interactions and its products.

Process	Reaction	Symbolism
Elastic scattering	${}^A_Z X + n \rightarrow {}^A_Z X + n$	(n,n)
Inelastic scattering	${}^A_Z X + n \rightarrow {}^A_Z X + n + \gamma$	(n,n γ)
Radioactive capture	${}^A_Z X + n \rightarrow {}^{A+1}_Z X + \gamma$	(n, γ)
Capture (n,a)	${}^A_Z X + n \rightarrow {}^{A-3}_{Z-1} X + \alpha$	(n, α)
Capture (n,p)	${}^A_Z X + n \rightarrow {}^A_{Z-1} X + p$	(n,p)
Capture (n,2n)	${}^A_Z X + n \rightarrow {}^{A-1}_Z X + 2n$	(n,2n)
Fission	${}^A_Z X + n \rightarrow Y + Z + \gamma$	(n,f)

Table 2.2: Neutron Interactions [7]

In **elastic scattering** the total energy of the incident neutron and target nucleus is conserved in the centre of mass frame. The neutron's energy loss in the interaction, is transmitted to the target nucleus in the form of kinetic energy, which may cause ionisation in the surrounding material and the direction of neutron is modified. Elastic scattering is important because it can occur without threshold in any neutron energy. An elastic scattering with incident neutron energy E_n and final energy E' gives the following ratio: [1]

$$\frac{E'}{E_n} = \frac{A^2 + 1 + 2A \cos \theta}{(A + 1)^2} \quad (2.2)$$

Where θ is the scattering angle and A the atomic mass. For no scattering ($\theta = 0$), $E'/E_n=1$. The maximum energy loss occurs for a head-on collision $\theta = 180^\circ$:

$$\left(\frac{E'}{E_n}\right)_{min} = \left(\frac{A - 1}{A + 1}\right)^2 \quad (2.3)$$

Another important equation is the energy transfer to the target nucleus: [7]

$$E_r = E_n \frac{4A^2}{(A + 1)^2} \cos^2 \theta \quad (2.4)$$

Where E_r is the energy that can be transferred to the target nucleus.

The energy transfer to the recoil nucleus increases if the mass number of the nucleus decreases and therefore is maximum for hydrogen atoms and high in light atoms. So in order to slow down the velocity of neutrons with the fewest number of collisions, a thin target with small A must be used.

In **inelastic scattering** (n,n' γ) the incident neutron is captured by the target nucleus, provided that neutron energy is high enough to excite the nucleus. The compound

nucleus then immediately decays with the ejection of a lower energy neutron and the residual nucleus changes to his ground state, with the emission of a gamma photon.

The energy of the resulting neutron E_f is given by the conservation laws of momentum and energy:

$$E_f = \frac{1}{(1+M)^2} \left[\omega \sqrt{E_i} \pm \sqrt{E_i(\omega^2 + M^2 - 1) - M(M+1)E_{ex}} \right]^2 \quad (2.5)$$

Where E_i is the incident neutron energy, M is the quotient of the target nucleus mass and the neutron mass, E_{ex} is the energy of the excited level of the residual nucleus and ω is:

$$\omega = \frac{1}{2} \left[(M+1) \sqrt{\frac{E_f}{E_i}} - (M-1) \sqrt{\frac{E_i}{E_f}} + \frac{ME_{ex}}{\sqrt{E_i E_f}} \right] \quad (2.6)$$

The valuable information here is that the quantity:

$$E_i(\omega^2 + M^2 - 1) - M(M+1)E_{ex} \quad (2.7)$$

must be ≥ 0 . This means that the neutron must have an energy above a threshold which should be at least equal with E_{ex} . The excited energy of the nucleus decreases with the increasing mass number of target nucleus. Neutrons with the energies in the ranges of 0.5MeV-5MeV can undergo inelastic scattering with light elements whereas for heavy elements neutrons in the range of keV are enough to cause inelastic scattering.

There are two categories of **neutron capture**, radioactive (n, γ) and non-radioactive (n,p),(n, α),(n,t),(n,2n),(n,d). In radioactive capture, the captured neutron excites the compound nucleus in a higher state, followed by immediate emission of gamma-rays. It is an exothermic reaction ($Q>0$) and it can occur for a wide range of neutron energies. As a rule, neutron capture cross section increases as the neutron velocity decreases. In non-radioactive capture, more than one neutron or charged particle emission is occurred. These reactions take place by quantum tunnelling since the energy of the incident neutrons is usually bellow the coulomb barrier of the compound nucleus. Their majority are endoenergetic reactions, so an energy threshold is required. However, there are some nuclei that can undergo an exothermic reaction such as 3H , ${}^{10}B$ and 7Li , whose high neutron cross section make them suitable for a converter layer, especially for thermal neutron detection.

A neutron capture could trigger **fission** if the interaction is with a heavy nucleus ($Z \geq 92$), where the compound nucleus may split into two daughter nuclei of lighter mass, followed by one or more fast neutrons release. This process can trigger a self sustain nuclear chain reaction. Nuclear fission power plants are based in this reaction, using heavy radioactive elements such as ${}^{233}U$, ${}^{235}U$, ${}^{239}Pu$ and ${}^{232}Th$.

2.5.1 Neutron interactions in Diamond

Thermal neutrons with energy 0.025eV, are usually detected by neutron capture. These thermal neutrons can be detected through a converter layer, usually ${}^{10}B$, taking advantage of the high cross section of ${}^{10}B(n_{th}, a){}_3^7Li$ reaction. The thermal neutron

cross section of this reaction is 3840 barn. Other converter layers often used are: ${}^3\text{H}$, ${}^7\text{Li}$, ${}^{157}\text{Gd}$ which also exhibit a high neutron capture cross sections.

Fast neutrons have a kinetic energy above 1MeV. They may lose their energy by scattering or capture, according to their initial, energy and when thermalised they can be captured by the processes mentioned above. In diamond detectors neutrons mainly interact with ${}^{12}\text{C}$ isotope, mostly though elastic and inelastic scattering up to 5MeV, while for higher neutron energies capture reactions channels become available, as shown in the table below. [21]

Nuclear Reaction	E_{th}	Q (MeV)
${}^{12}\text{C}(n, n'){}^{12}\text{C}$	0	0
${}^{12}\text{C}(n, n'){}^{12*}\text{C}$ (first excited state)	4.8	0
${}^{12}\text{C}(n, n'){}^{12*}\text{C}$ (second excited state)	8.2	0
${}^{12}\text{C}(n, n'){}^{12*}\text{C}$ (third excited state)	11.1	0
${}^{12}\text{C}(n, n'){}^{12*}\text{C}$ (fourth excited state)	13.76	0
${}^{12}\text{C}(n, \alpha){}^9\text{Be}$	6.2	-5.7
${}^{12}\text{C}(n, n')3\alpha$	7.9	-7.3
${}^{12}\text{C}(n, p){}^{12}\text{B}$	13.6	-12.6
${}^{12}\text{C}(n, d){}^{11}\text{B}$	14.9	-13.7
${}^{13}\text{C}(n, \alpha){}^{10}\text{Be}$	4.1	-3.8

Table 2.3: Neutron reactions in diamond [19]

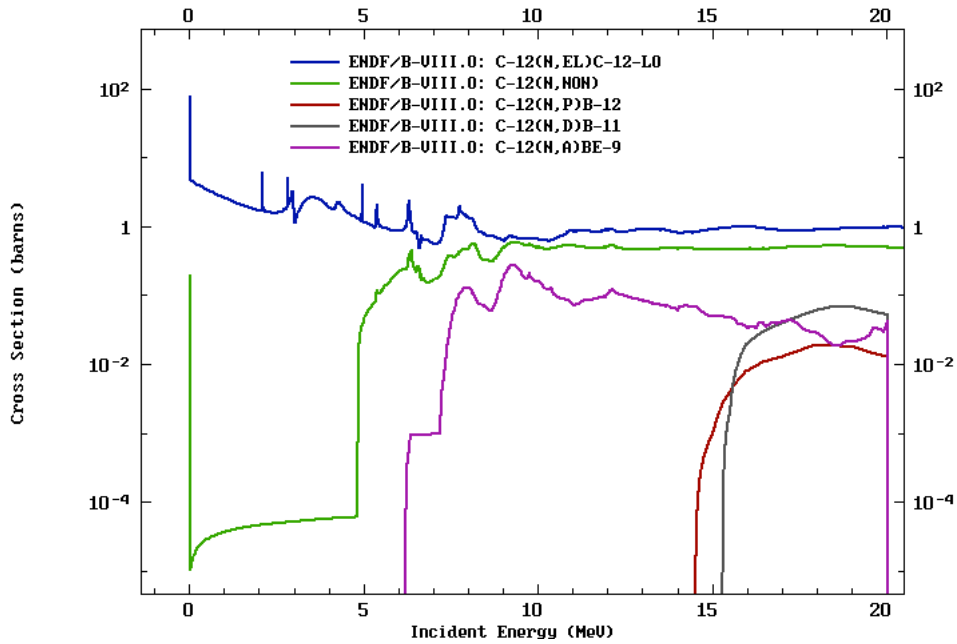


Figure 2.1: Neutron cross sections of (n,n),(n,n'),(n,p),(n,d),(n,a) reactions in ${}^{12}\text{C}$. Data obtained from ENDF database.

From figure 2.1, we can see that for neutron energies up to 20MeV elastic and inelastic scattering is dominant, hence in any collected spectrum we expect a strong contribution from scattering interactions. The energy deposition spectrum for the elastic interaction is the product of ionisation by the ^{12}C or ^{13}C recoil nuclei. The spectrum for low energy neutrons has the maximum of the distribution in the lower energies and a characteristic cut off at the maximum deposited energy determined by kinematics. For higher neutron energies (n,p),(n,d),(n,a) reactions appear as Gaussian peaks in the energy deposition spectrum as shown in figure 2.2.

The energy deposition due to the neutron elastic scattering is visible in the spectrum below 4 MeV. After this limit, (n,a) peaks with ^{12}C or ^{13}C are becoming visible. For 14 MeV neutrons, where most studies are focused, due to D-T fusion neutrons, the spectrum is shown in figure 2.6

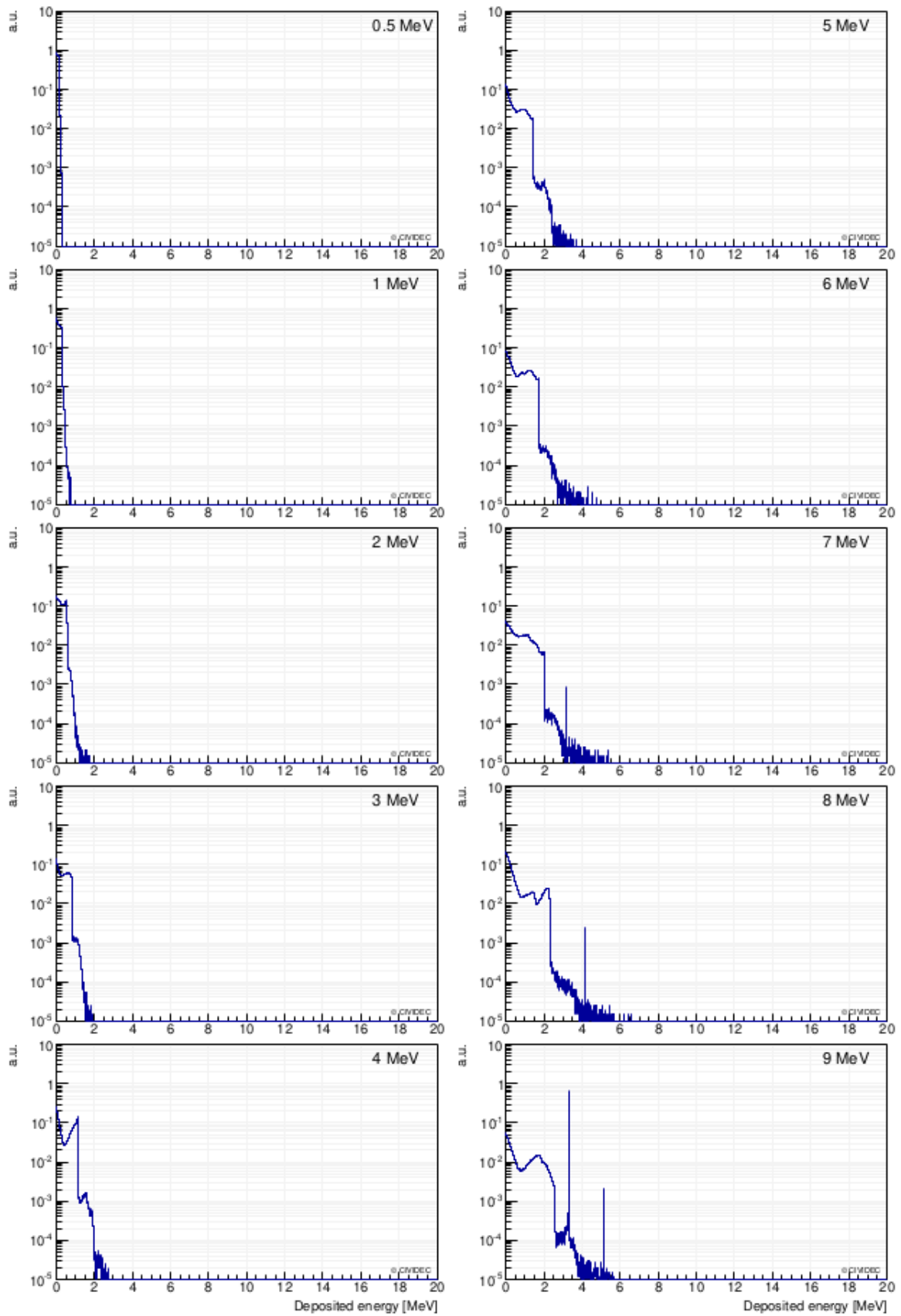


Figure 2.2: Energy deposition spectra of energies from $E_n=0.5$ to $E_n=9$ MeV in a $500 \mu\text{m}$ diamond detector [21]

2.5.2 Neutron interactions in Si

In silicon, the main reactions are elastic scattering with a momentum transfer to the Si recoil, as well as (n,p) and (n,a) capture reactions in ^{28}Si as presented in table 2.4. The cross sections of the main interactions which occur in those energies are represented in figure 2.3. For neutron energies lower than 3MeV to 4MeV only elastic scattering occurs. The maximum energy transfer to the recoil nucleus is approximately $0.13E_n$. The problem with this low energy transfer is the gamma-rays contamination. The standard threshold for photons is 500keV or higher, so in many cases the resulting signals of the silicon detector can not be distinguished from photon signals.

For neutrons with energies higher than 3.8MeV the maximum energy transfer is above the 500keV threshold. In addition, in small energies the elastic cross section is orders of magnitude higher than neutron capture reactions. All of the above lead us to the conclusion that in silicon detectors the reactions of interest are the ones producing charged particles, the probability of which increases with increasing energy. So, silicon detectors mainly take advantage of neutron interactions above 5MeV or 10MeV. [22].

Nuclear Reaction	E_{th} (MeV)	Q(MeV)
$^{28}\text{Si}(n, n')^{28}\text{Si}$	0	0
$^{28}\text{Si}(n, n')^{28*}\text{Si}$ (first excited state)	1.84	0
$^{29}\text{Si}(n, n')^{29*}\text{Si}$ (first excited state)	1.31	0
$^{30}\text{Si}(n, n')^{30*}\text{Si}$ (first excited state)	2.31	0
$^{28}\text{Si}(n, \alpha)^{25}\text{Mg}$	2.74	-2.65
$^{29}\text{Si}(n, \alpha)^{29}\text{Mg}$	0.035	-0.031
$^{28}\text{Si}(n, p)^{28}\text{Al}$	3.99	-3.85
$^{28}\text{Si}(n, d)^{27}\text{Al}$	9.70	-9.36

Table 2.4: Neutron interactions in ^{28}Si . [19], [23]

The energy deposition spectrum for 5MeV neutrons is presented in figure 2.4. We can see that in low energies elastic and inelastic scattering with ^{28}Si are dominating the distribution. For energy deposition above 1MeV the charged particles are beginning to lose energy inside the silicon crystal. Small peaks of (n,p) and (n,a) reactions are observed at approximately 1MeV and 2.5MeV respectively. For 14 MeV neutrons the energy deposition spectrum is presented in figure 2.7. In these energies we see clear peaks of $^{28}\text{Si}(n, \alpha)^{25}\text{Mg}$ reactions corresponding to the excited states of ^{25}Mg .

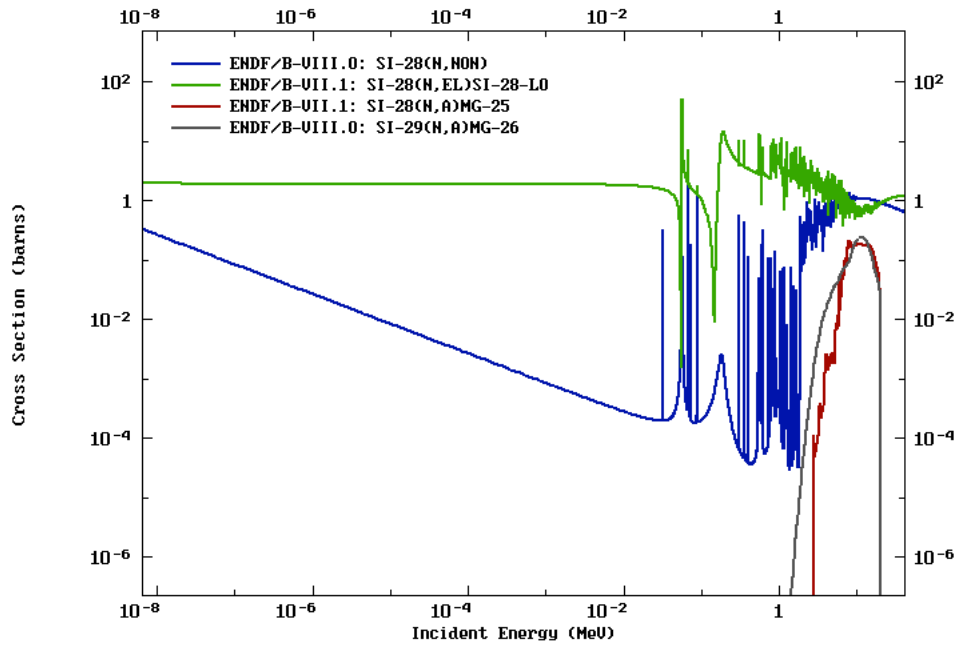


Figure 2.3: Neutron cross sections of (n,n),(n,n'),(n,a) reactions in ^{28}Si and (n,a) in ^{29}Si . Data obtained from ENDF database.

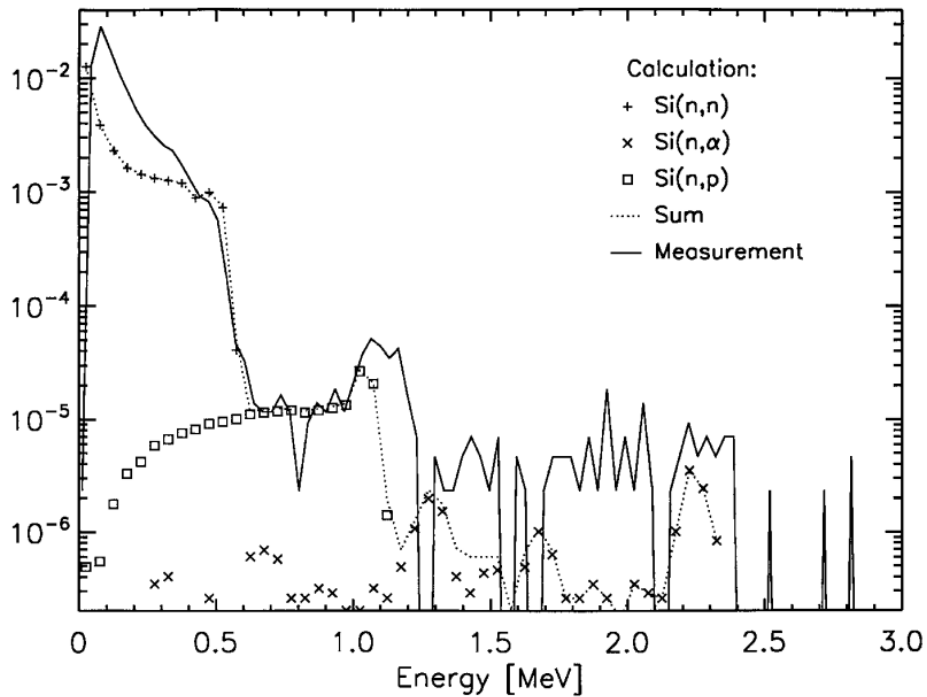


Figure 2.4: Calculated and measured energy deposition to 5MeV neutrons with count density per fluence [$\text{cm}^2\text{MeV}^{-1}$]. [22]

2.5.3 Neutron interactions in SiC

SiC interactions with neutrons, combine the reactions shown in tables 2.3 and 2.4. The energy deposition spectrum for 14MeV neutrons is shown in figure 2.5. For fast

neutrons with energy up to 14MeV, mostly the following nuclear reactions participate in the detector response deriving both from carbon and silicon nuclei.

- $^{12}\text{C}(n, n')^{12}\text{C}$ elastic scattering with $\sigma=778.62$ mbarn
- $^{12}\text{C}(n, n')^{12*}\text{C}$ inelastic with $\sigma=210.60$ mbarn
- $^{12}\text{C}(n, n')3\alpha$ with $\sigma=200$ mbarn
- $^{12}\text{C}(n, \alpha)^9\text{Be}$ with $\sigma=62.3$ mbarn
- $^{28}\text{Si}(n, n')^{28}\text{Si}$ elastic scattering with $\sigma=696.83$ mbarn
- $^{28}\text{Si}(n, n')^{28*}\text{Si}$ inelastic with $\sigma=1.03$ mbarn
- $^{28}\text{Si}(n, \alpha)^{25}\text{Mg}$ with $\sigma=197.12$ mbarn

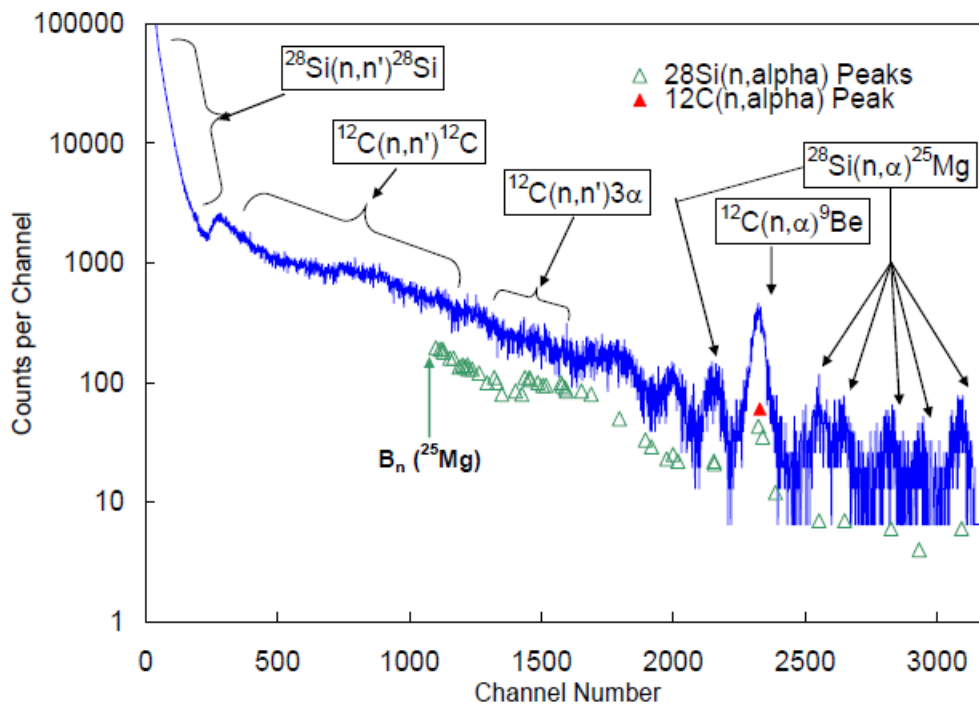


Figure 2.5: Silicon Carbide energy deposition spectrum to 14MeV neutrons. Channel number is directly proportional to energy deposited in the SiC active volume. [19]

At the low energy ranges of the spectrum, the continua for ^{28}Si and ^{12}C elastic and inelastic scattering dominate the detector response. At higher energies, specific reaction peaks are beginning to appear, with $^{13}\text{C}(n, \alpha)^{10}\text{Be}$ being the most prominent. Peaks corresponding to the $^{28}\text{Si}(n, \alpha)^{25}\text{Mg}$ reaction are also observed in the highest energy channels. Peaks that represent the production of excited states of ^{25}Mg can be seen in lower energies.

A comparison between a silicon carbide's detector with a diamond's and silicon's detector response for 14MeV neutrons is shown in figure 2.6 and 2.7. In all the spectra we can see that bellow 4MeV elastic scattering from ^{28}Si and ^{12}C dominate the response of the detectors. At higher energies the well defined peaks of neutron capture reactions are observable. SiC combines the characteristic peaks from both $^{13}\text{C}(n, \alpha)^{10}\text{Be}$ and

Chapter 3

Simulated detector response to fusion neutrons

In this chapter a brief introduction to GEANT4 Monte Carlo code is made, including the basic concepts of the simulation such as the geometry, Run, Event Track and Step. The simulation of the energy deposition of a neutron pencil beam of 2.45 MeV in a diamond, silicon and silicon carbide is presented and discussed both in void and air. Lastly, a research for a gamma ray energy energy deposition was made, to determine a possible threshold for the analysis, in order to exclude the typical 0.5MeV, 1MeV and 2MeV gamma rays.

3.1 The GEANT4 Monte Carlo code

Geant4 is a simulation toolkit first developed in 1993 using C++. It simulates the passage of particles through matter. Its areas of application include radiation physics, high energy experiments, nuclear and accelerator physics, as well as studies in medical and space science. This toolkit provides a variety of software components, which can be employed in a variety of settings, from simple studies of basic phenomena, to large scale experiments such as the Large Hadron Collider and other similar facilities. A documentation is provided which includes installation, user and reference guides and a set of training examples. Also a Web-based user forum is running, covering a variety of questions and issues which may arise. [25], [21]

For any simulation the user must define all the aspects of the problem. These include: the geometry of the system, the materials or compositions involved, the beam source (primary particles) and direction as well as the physics that is used. The description of physics in GEANT4 includes models for electromagnetic interactions of leptons, photons, hadrons, and ions, as well as the weak and strong interactions. The definition of particles and their interactions are specified with many different physics lists and packages which the program provides and the user chooses according to the physical problem. One or more processes can be assigned to a particle and one or more models can be registered for a given process. All the above are represented by C++ classes, which describe how certain interactions take place including kinematics, momentum, energy thresholds or any other specific features of the interaction, for example special definition of certain materials.

The geometry category offers the ability to describe both simple and complex geometrical structures and transports particles through the given materials. To begin the definition of the geometry the user must describe the mother volume in which all the additional shapes will be built. To describe a volume's shape the concept of solid is used and it contains specific values for the corresponding dimensions. To describe a volume's full properties, the term logical volume is used, which can hold other volumes inside it. It includes the geometrical properties of the solid and adds physical characteristics such as the material or magnetic field. The position of the volume is described by the term physical volume which places the logical volume inside a larger, containing volume. So, three basic concepts are used when defining the geometry: solid, logical and physical volume, where every function describes different properties and each volume can contain smaller volumes.

The simulation has several units to describe its sequence and the user has access to all of them. Run, Event, Track and Step are the basic units of the simulation. The largest is Run, which is a collection of simulated events. Run and Event share a common beam and detector implementation. When a run starts the geometry is optimised, the primary particles and their production is included and the required cross sections as well as energy ranges are calculated for the materials according to the physical processes. Before the event is processed, it contains information of the primary particles and after processing, it includes hits generated by the simulation as well as the tracks of the simulated particles. The objects from the event classes can be stored by the user for further down-processing.

Track category invokes the transportation procedure, which is independent of the particle type or physical process. In GEANT4 all physical processes associated with each particle are performed with steps. Steps are proposed by all the processes, including geometry and materials. The particles are followed step by step by the toolkit, until they interact with the geometry (producing secondary particles, which in turn are watched step by step) or exiting the mother volume. The sum of all produced steps consists a track while the sum of the primary and secondary particle tracks constitutes an event. The graphic representation of the event is described in figure 3.1

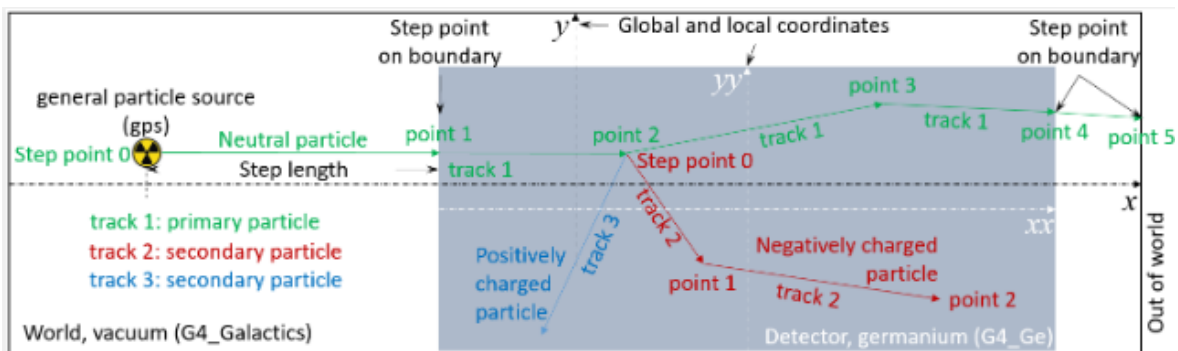


Figure 3.1: Graphic representation of an event. A particle track is the sum of all the steps while a step point represents where the particle is generated or changes direction. [26]

3.2 Simulated neutron energy deposition in semiconductor sensors

In this work using GEANT4 simulations, the interactions of 2.45MeV neutrons with a diamond, silicon and silicon carbide semiconductor detector were studied. For the set-up, a solid volume detector with dimensions $4mm \times 4mm \times 50\mu m$ was built along with the description of the materials for each sensor. The physics list used was the QGSP-BIC which focuses on hadronic elastic, inelastic and capture processes [27]. Also the hadronic high precision models (HadronicHP) were included manually. A monoenergetic neutron pencil beam of 10^9 primary particles, with 2.45MeV energy, was used to examine the energy deposition spectrum of the three materials. The simulation was first performed in void and then in air in order to examine the air contamination for more realistic conditions.

3.2.1 Diamond Detector

For the diamond detector the collected spectrum in void is presented in figure 3.2. Out of the 10^9 primary neutrons, approximately $8 \cdot 10^5$ interactions lead to energy deposition.

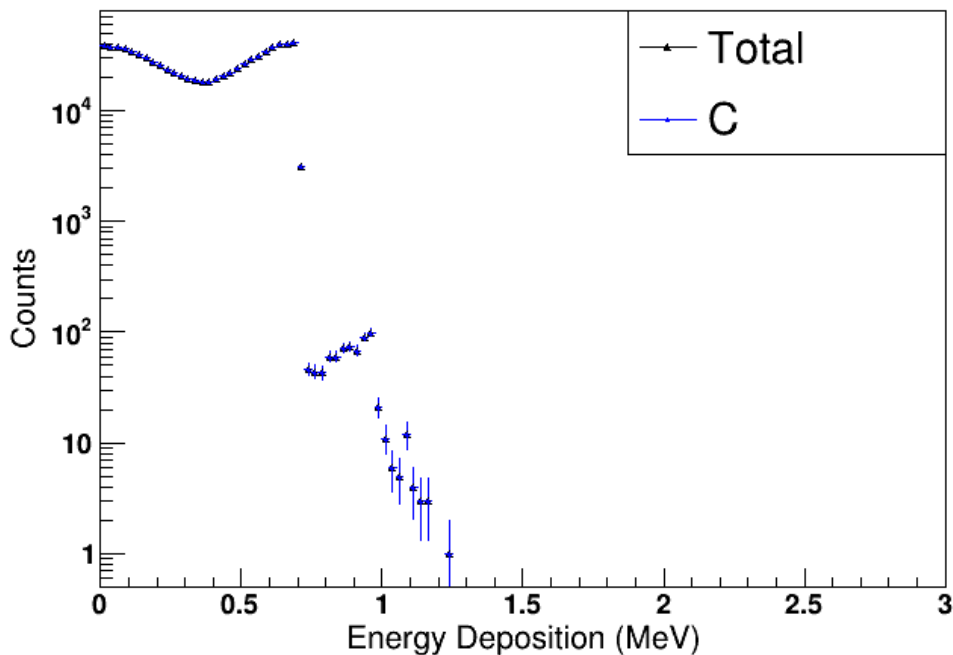


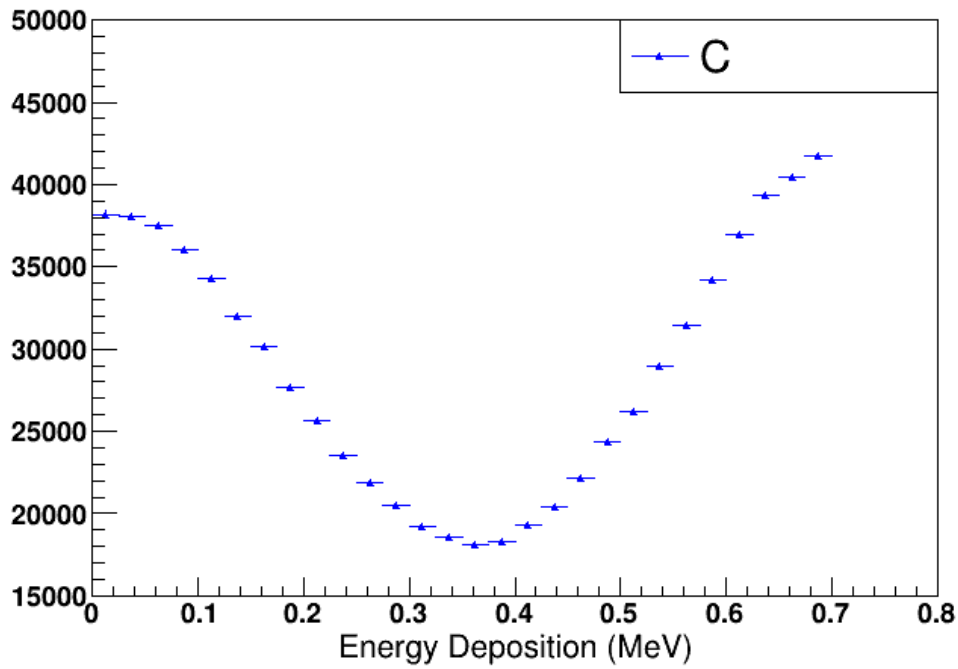
Figure 3.2: Energy deposition spectrum for a $50\mu m$ C detector to 2.45MeV neutrons in void, total of 809014 counts. The blue points represent the carbon recoils and the black the total energy deposition. The spectrum is dominated by neutron elastic scattering.

GEANT4 uses the NIST database for the atomic weight and isotopic composition of the elements [28]. Carbon consists of 98.93% of ^{12}C and 1.07% of ^{13}C , so we assume that the main neutron interactions occur with ^{12}C . In this energy according to table 2.3, the only reaction allowed is the elastic scattering. We observe the characteristic cut-off

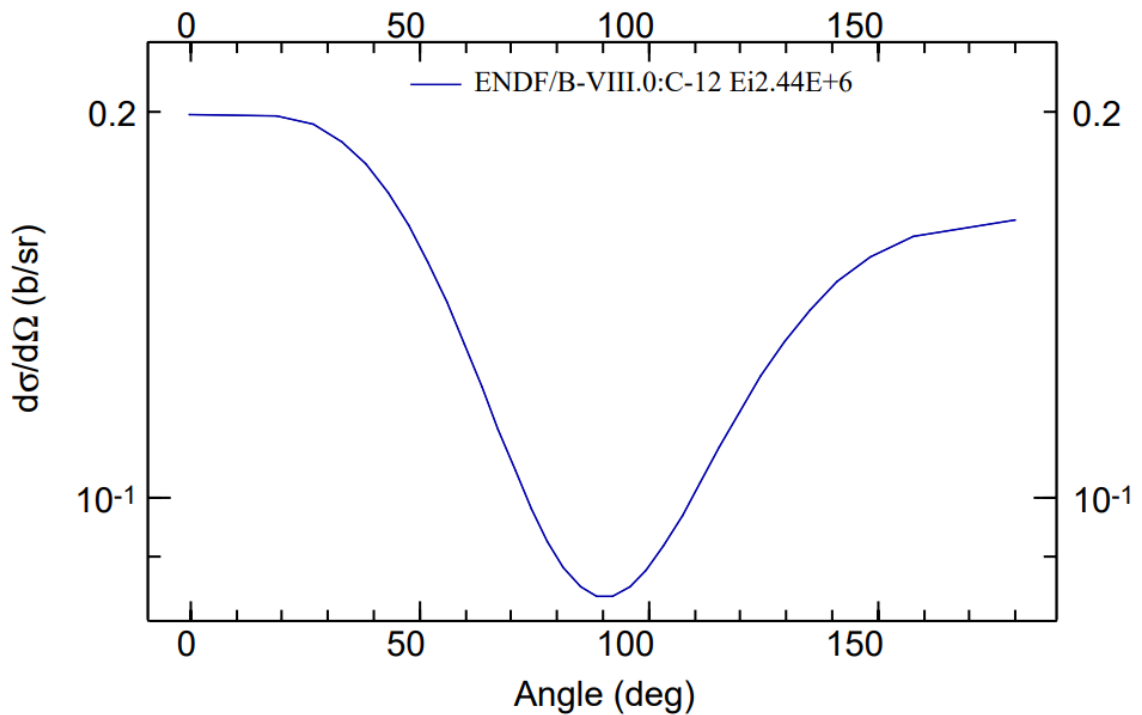
at the maximum deposited energy. According to kinematics, the recoil nucleus, for 2.45MeV neutrons, has the energy range of approximately 0 to a maximum of 0.7MeV. This is the energy range in the spectrum that acquires most of the counts. However we can see that the energy deposition exceeds the 0.7MeV limit for the elastic scattering and reaches almost 1.2MeV. The counting rate drops three orders of magnitude but these interactions exist. This is explained by double neutron scattering. Due to the size of the detector $4mm \times 4mm \times 50\mu m$ some neutrons find it possible to induce up to two elastic scatterings inside the volume. For example the first neutron will produce a 0.7MeV (the maximum energy allowed) recoil nucleus and will travel through the volume with 1.74MeV energy. This neutron due the non negligible dimensions of the volume has a possibility of interacting with elastic scattering with another carbon nucleus. This second interaction is possible to occur in small angles so the energy of the second recoil nucleus will be approximately from 0 to 0.5MeV giving a total of 1.2MeV. Of course, all the angle combinations are a possibility, however two consecutive interactions in high angles (two backscattering interactions) leaving the recoil nucleus at 1.4MeV (0.7MeV+0.7MeV) is unlikely to happen, that's why the spectrum has a maximum of 1.2MeV. The consecutive interactions in GEANT4 are read as one in the total energy deposition spectrum.

After the elastic scattering analysis, the shape of the spectrum must be examined. For this step the energy deposition spectrum was zoomed in the primary elastic region, as shown in figure 3.3a and compared to the angular distribution of neutrons, deriving from $^{12}C(n, n')^{12}C$ elastic scattering, obtained from ENDF evaluated data for 2.44MeV neutrons, shown in figure 3.3b. We observe that the shapes follow a similar distribution: For smaller angles ($0^\circ - 80^\circ$) neutrons lose a small fraction of their energy, hence the recoil nucleus corresponds to low energy depositions. Reaching the intermediate angles 90° from figure 3.3b we observe that the value $d\sigma/d\omega$ drops orders of magnitude, which is imprinted in the energy deposition spectrum 3.3a with a characteristic counts decrease. In big angles ($100^\circ - 180^\circ$) neutrons lose a significant portion of their kinetic energy so the lost energy transfers to the recoil nucleus leading to a higher energy deposition.

The two spectra exhibit some differences, in both high and low energies/angles, where they seem to be in reverse. While the majority of the counts is imprinted in the low energy deposition ranges (low neutron scattering angles) as expected from the angular distribution, the shape of the energy deposition (figure 3.3a) shows that the high energies (large neutron scattering angles) are favoured. This is explained with the sensor's thickness. Due to the non-negligible thickness and the highly symmetrical shape of the angular distribution, the energy deposition spectrum is slightly deformed. If the sensor's thickness is reduced, as shown in figure 3.4, the collected energy deposition spectrum and the angular distribution from figure 3.3b are in better agreement.



(a) Simulated 2.45 neutron energy deposition spectrum for a $50\mu\text{m}$ C detector, zoomed in the primary elastic region.



(b) Angular distribution of 2.44MeV neutrons deriving from elastic scattering with ^{12}C . Data obtained from ENDF database.

Figure 3.3: Comparison of 2.45MeV neutron angular distribution 3.3b and the energy deposition spectrum 3.3a for the elastic scattering of ^{12}C . Similar distribution is followed as expected from kinematics.

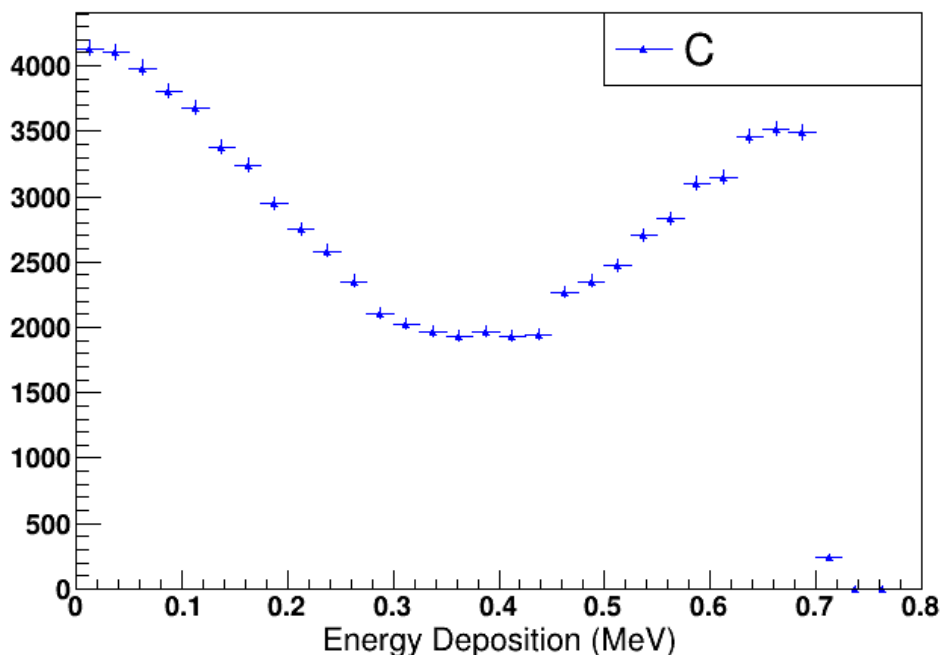


Figure 3.4: Simulated 2.45 neutron energy deposition spectrum for a $5\mu\text{m}$ diamond detector, zoomed in the primary elastic region. A better level of agreement is observed with the angular distribution figure 3.3b

We conclude that kinematics confirm the resulting spectra produced by GEANT4, thus we can claim that neutron cross section and angular distribution are calculated with high precision from the simulation.

When the whole geometry is in **air**, a number of interactions channels open. Air in GEANT4 constitutes of 0.0124% carbon, 75.52% nitrogen, 23.17% oxygen and 1.2% argon with a density of 1.204 mg/cm^3 . Due to their dominance, neutron interactions with ^{14}N , ^{16}O were examined. Both scattering and nuclear reactions occur, as shown in table 3.1. For the C sensor, when the whole geometry is in air, the spectrum shown in 3.5 was collected:

Nuclear Reaction	E_{th} (MeV)	Q(MeV)
$^{14}\text{N}(n, n')^{14}\text{N}$	0	0
$^{14}\text{N}(n, n')^{14*}\text{N}$ (first excited state)	2.478	0
$^{14}\text{N}(n, p)^{14}\text{C}$	0	0.6259
$^{14}\text{N}(n, \alpha)^{11}\text{B}$	0.1694	-0.1581
$^{16}\text{O}(n, n')^{16}\text{O}$	0	0
$^{16}\text{O}(n, \alpha)^{13}\text{C}$	2.35	-2.21

Table 3.1: Main neutron interactions with air for 2.45MeV neutron energy.

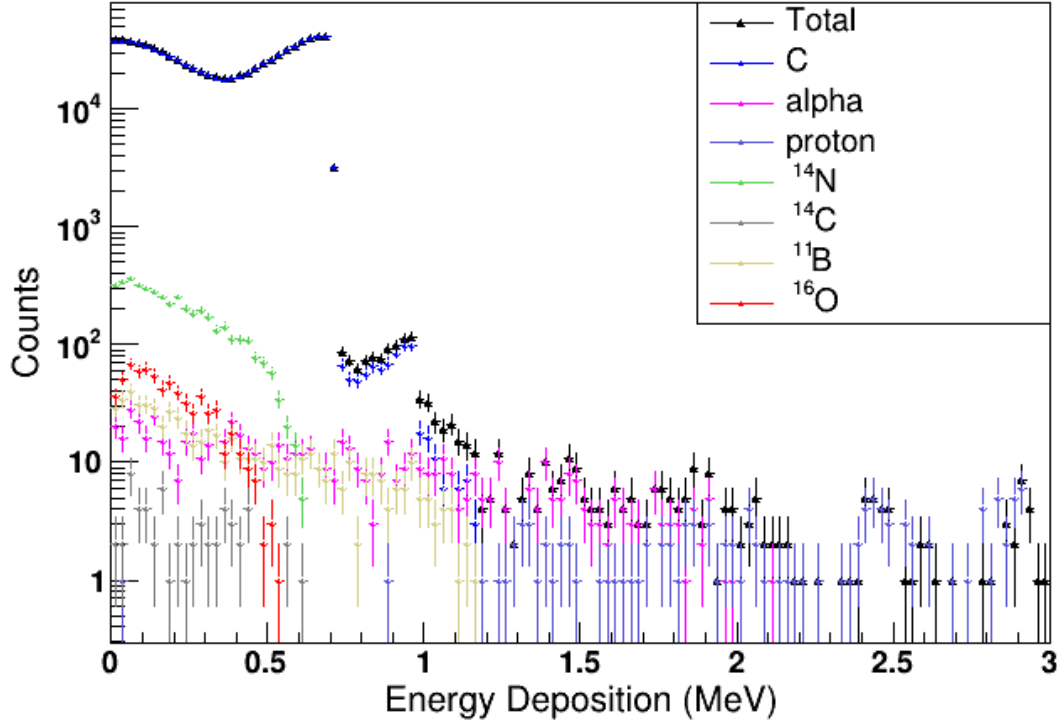


Figure 3.5: Energy deposition spectrum for a $50\mu\text{m}$ C detector for 2.45MeV neutrons in air (total of 816014 counts). ^{12}C recoil nucleus from elastic scattering are observed as well as ^{14}N , ^{14}C , ^{11}B , ^{16}O recoil nucleus with the produced charged particle (alpha or proton), deriving from all the other nuclear reactions with the basic air elements, as shown in 3.1. The detector from the neutron source has 1cm distance.

We observe that the elastic scattering region produced by ^{12}C recoils, as expected, has the same shape and energy ranges as in void 3.2. Scattering from ^{14}N results in neutron energy from 1.835MeV to 2.45MeV and recoil nucleus from approximately 0MeV to 0.615MeV . Scattering from ^{16}O results in neutron energy from 1.903MeV to 2.45MeV and recoil nucleus from approximately 0MeV to 0.547MeV .

The protons observed derive from the $^{14}\text{N}(n,p)^{14}\text{C}$ reaction, which are expected in the energy range $2.3 - 3.073\text{ MeV}$ (from kinematics) . The ^{14}C recoils are expected from 0.003MeV to 0.696MeV .

The alpha particles derive from both $^{14}\text{N}(n,\alpha)^{11}\text{B}$ and $^{16}\text{O}(n,\alpha)^{13}\text{C}$ reactions. The expected energy ranges through kinematics are: $1.08\text{MeV}-2.128\text{MeV}$ and $0.006-0.199$ respectively. The corresponding ^{11}B recoil nucleus energy is expected in the range $0.164\text{MeV}-1.212\text{MeV}$, while the ^{13}C one in the range $0.036\text{MeV}-0.229\text{MeV}$.

All the above are verified by the simulated spectrum 3.5. The energies match the theoretical values and the energy deposition is explained by kinematics. We observe that the total energy deposition spectrum is contaminated by the air interactions as expected. The primary elastic region's shape remains intact, however slightly energy differences are observed due to the ^{14}N .

3.2.2 Silicon Detector

The silicon detector was examined in the same conditions as the diamond. A $4\text{mm} \times 4\text{mm} \times 50\mu\text{m}$ silicon detector's interactions were simulated with a neutron pencil beam, including 10^9 primary particles in void. From the NIST library silicon constitutes of 92.23% ^{28}Si , 4.6% of ^{29}Si and 3% of ^{30}Si . The dominant is ^{28}Si , however all three isotopes must be examined. For 2.45MeV neutrons according to table 2.4 for Si interactions, both elastic scattering and inelastic scattering occurs for the first excited state in all three isotopes. Also $^{29}\text{Si}(n, \alpha)^{26}\text{Mg}$ is allowed but with a small cross section according to figure 2.3. The resulted spectrum is presented in figure 3.6.

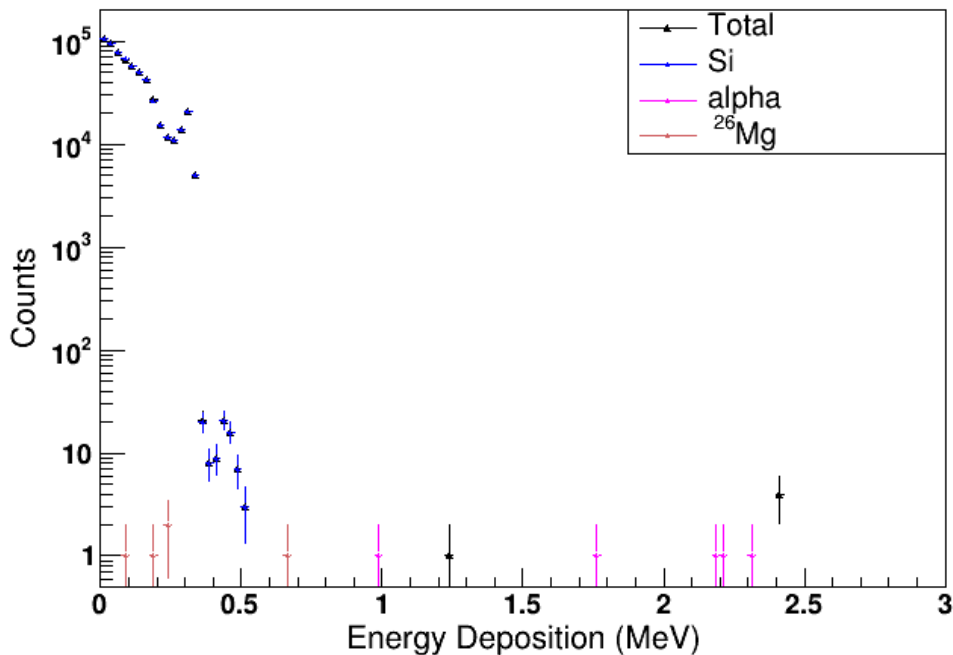


Figure 3.6: Energy deposition spectrum for a $50\mu\text{m}$ Si detector for 2.45MeV neutrons in void, total of 602727 counts. The blue and brown point represent the silicon and ^{26}Mg recoils, the pink the alpha particles and the black the total energy deposition

Neutron elastic scattering with ^{28}Si nucleus produces a recoil from almost 0 to 0.33MeV, while for inelastic the maximum recoil energy is 0.185MeV. For ^{29}Si the energy ranges for elastic are from 0 to 0.31MeV, while for inelastic the maximum recoil energy is 0.22MeV. For ^{30}Si the expected energies for elastic are from 0 to 0.309 MeV, while for inelastic the maximum recoil energy is 0.119MeV. The characteristic drop at the end of the scattering is visible at approximately 0.3MeV. So, the spectrum for scattering as discussed, should stop at maximum 0.3MeV. However the silicon recoils corresponding to scattering, reach energies higher than 0.5MeV. This is the same phenomenon observed for the C detector, due to the non negligible dimensions of the detector some neutrons undergo double scattering, thus depositing higher energy in the detector.

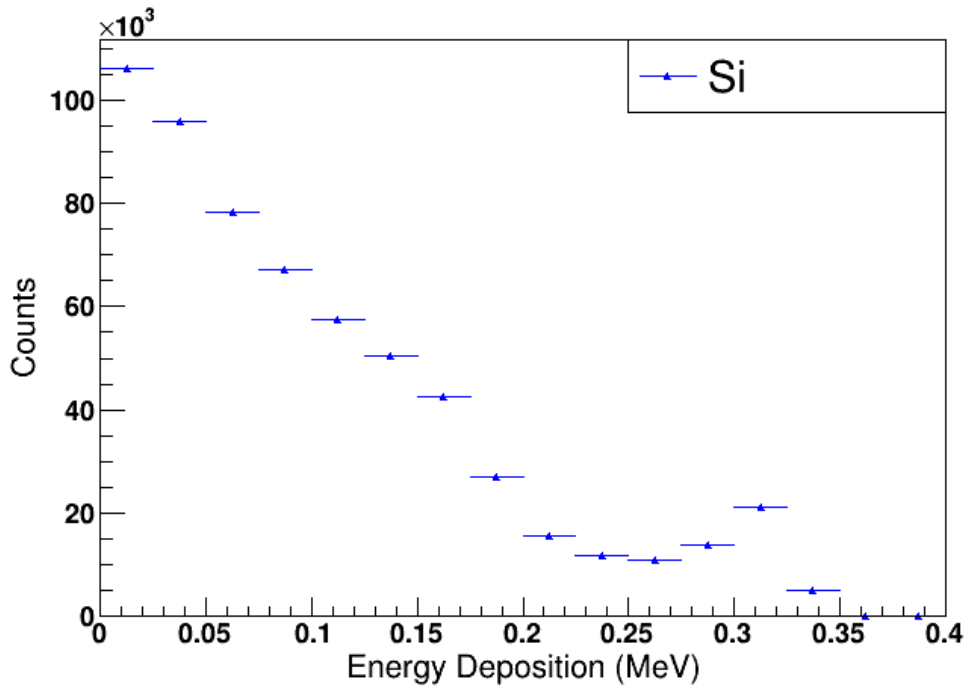
Apart from the scattering in silicon we observe (n, α) reactions. Due to their small cross section, for 10^9 neutrons GEANT4 calculates only 5 counts of α particles and ^{26}Mg recoils. The Q value of the reaction is nearly zero and that is why there are some

counts in the maximum neutron energy (2.45MeV). From this reaction the recoil ^{26}Mg nucleus is expected with energies 0-0.6MeV while the alpha particle from 1.7-2.3MeV. We see that the energy ranges in the spectrum are in agreement with the theoretical calculations, so we conclude that the GEANT4 successfully calculates the kinematics of the reactions. As we can also see from similar theoretical studies, in figure 2.4 the spectrum in low energies matches the results from GEANT4.

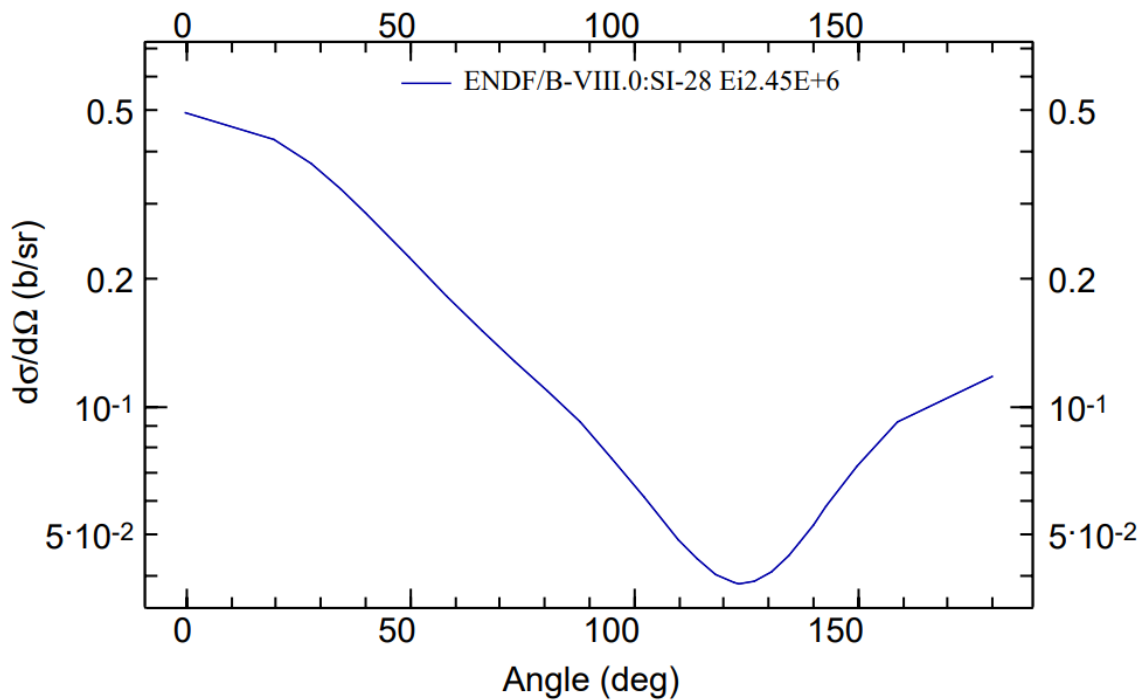
For silicon both inelastic and elastic scattering are possible due to the shape of the cross section as shown in figure 2.3. In these energies we observe many resonances, in contrast with the C detector where the cross section follows a smooth shape. These resonances increase or drop the cross section which directly affects the probability in which the interaction occurs as well as the energy deposition spectrum. While neutrons lose part of their initial energy in the target volume, the probability of interacting varies by a big factor in a small energy range. Due to these resonances, the interactions and thus recoil production are not favoured in contrast to C interactions. This is imprinted in the total counts: for Si the total counts (602727) recorded were far less than the diamond (809014 counts). We conclude that in these energy ranges neutron interactions favour the C detector over the Si.

The examination of the angular distribution is allowed to cross check the shape of the energy deposition spectrum. The evaluated data from ENDF database, for neutron angular distribution deriving from elastic scattering with ^{28}Si were compared to the simulated spectrum for the recoil nucleus energy deposition zoomed in the primary elastic region as shown in figure 3.7.

The behaviour is similar to the C case. In scattering angles from 0° to 100° neutrons lose a small fraction of their energy, hence the recoil nucleus corresponds to low energy depositions. The distribution then follows a characteristic counts decrease as expected in the neutron angular distribution spectrum 3.7b. In higher angles due to the higher fraction of energy that neutrons lose, the recoil nuclei 3.7a correspond to higher energy depositions but with a small rate. In Si due to the highly asymmetrical shape of the angular distribution and the intense resonances observed in the neutron cross section, the thickness of the sensor doesn't play a significant role as in C case, so the two graphs seem to be in good agreement.



(a) Simulated 2.45 neutron energy deposition spectrum for a 50 μ m Si detector, zoom in the primary scattering region



(b) Angular distribution of 2.44MeV neutrons deriving from elastic scattering with ^{28}Si . Data obtained from ENDF database

Figure 3.7: Comparison of 2.45MeV neutron angular distribution 3.7b with a 50 μ m Si detector and the recoil nucleus energy deposition spectrum 3.7a for the elastic scattering of ^{28}Si . The two distributions seem to be in complete agreement.

For the air contamination, the following spectrum was collected, including the tracking

of ^{14}N , ^{14}C , ^{11}B , ^{16}O and the charged protons and alpha particles, produced from the reactions shown in table 3.1.

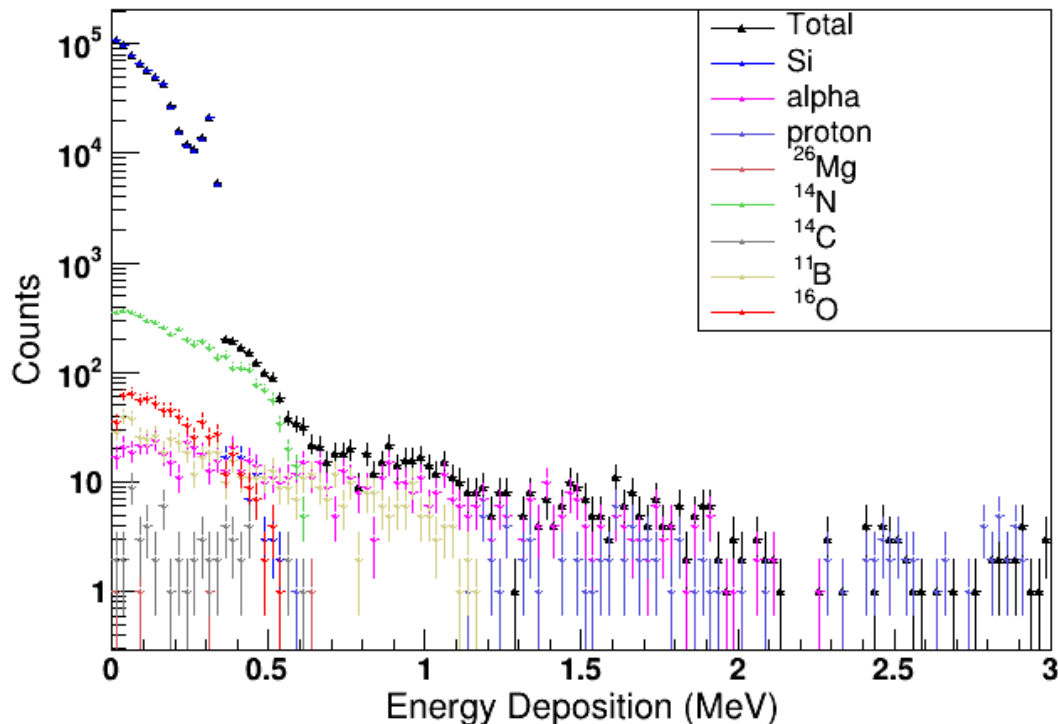


Figure 3.8: Energy deposition spectrum for a $50\mu\text{m}$ silicon detector for 2.45MeV neutrons in air (total of 603013 counts). ^{28}Si recoil nucleus from elastic scattering are observed as well as ^{14}N , ^{14}C , ^{11}B , ^{16}O recoil nucleus with the produced charged particle (alpha or proton), deriving from nuclear reactions with the basic air elements, as shown in 3.1. The detector from the neutron source has 1cm distance.

It is obvious that the nuclear reactions happening in air are the same as in the C detector 3.5. The spectrum deriving from elastic scattering is once again dominant and has the same shape as in void (figure 3.6). The contamination from ^{14}N , ^{16}O follows the same energies as proposed by kinematics. Of course once again a small number of ^{26}Mg recoils is observed due to $^{29}\text{Si}(n, a)^{26}\text{Mg}$.

3.2.3 Silicon Carbide Detector

A $4\text{mm} \times 4\text{mm} \times 50\mu\text{m}$ silicon carbide detector interacting with a 2.45MeV neutron pencil beam including 10^9 primary particles both in void and in air was examined. The collected energy deposition spectrum in void is presented in figure 3.9.

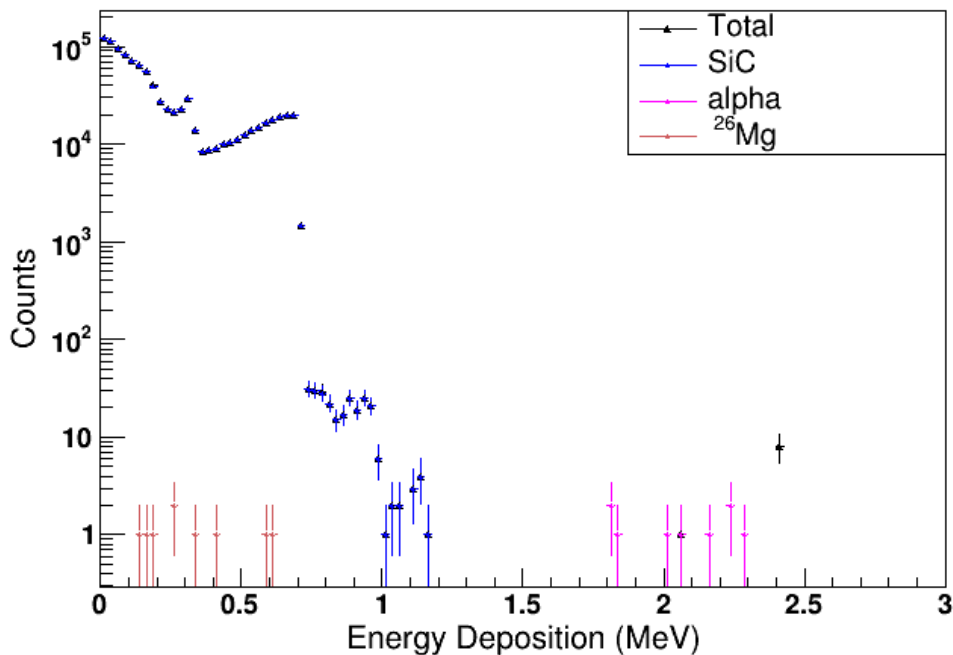


Figure 3.9: Energy deposition spectrum for a 50 μm SiC detector for 2.45MeV neutrons in void, total of 971113 counts. The blue and brown point represent the silicon and ^{26}Mg recoils, the purple the alpha particles and the black the total energy deposition

SiC interactions with neutrons combines the spectra of both C and Si. In the low energy region, neutrons undergo elastic scattering with the carbon nuclei as well as elastic and inelastic with the silicon nuclei. There is the characteristic drop around 0.3MeV where the scattering from Si recoils stops and at 0.7MeV which marks the end of the elastic scattering with C. A small number of (n,a) reactions is observed (9 in total) which occur with ^{29}Si . Their number is a bit higher than pure Si due to the larger density of SiC ($\rho_{\text{SiC}} = 3.21\text{g}/\text{cm}^3$, $\rho_{\text{Si}} = 2\text{g}/\text{cm}^3$) We observe that counts in SiC (971113) are higher than diamond (809014), which is logical if we think that interactions are favoured due to the presence of both Si and C as well as the higher density.

The SiC spectrum in **air** is shown in figure 3.10. The elastic scattering region formed by SiC recoils follows the same shape as the spectrum in void (figure 3.9) and the air contamination has the same distribution as in both Si and diamond detectors as expected.

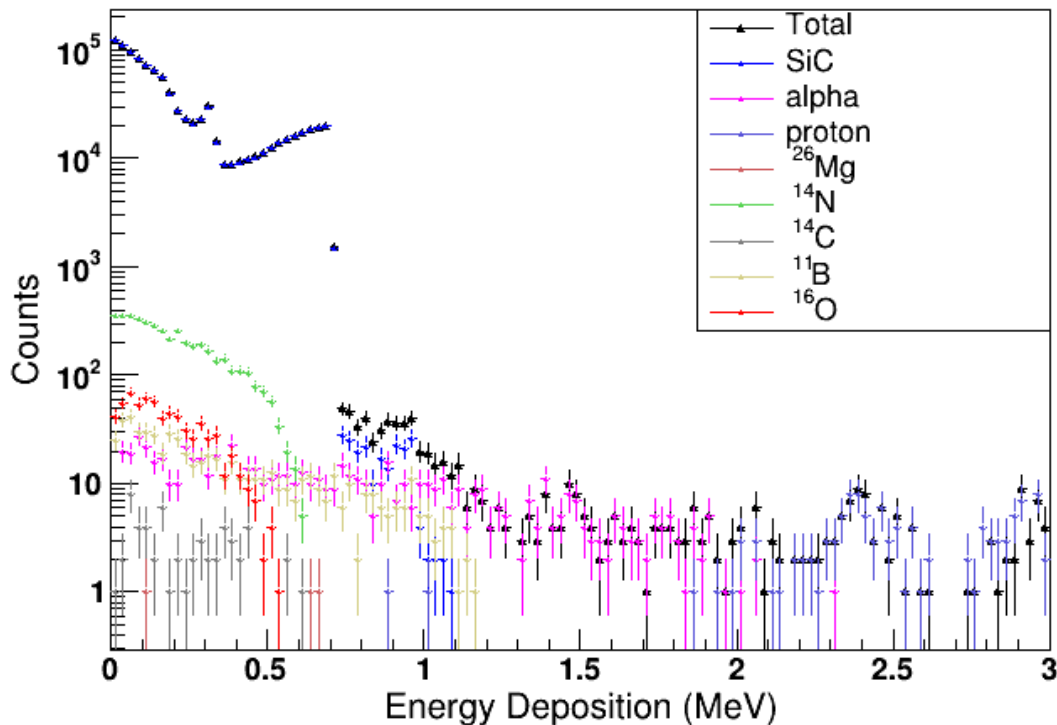


Figure 3.10: Energy deposition spectrum for a 50 μm SiC detector for 2.45MeV neutrons in air (total of 971472 counts). ^{28}Si and ^{12}C recoil nucleus from elastic scattering are observed as well as ^{14}N , ^{14}C , ^{11}B , ^{16}O recoil nucleus with the produced charged particle (alpha or proton), deriving from nuclear reactions with the basic air elements, as shown in 3.1. The detector from the neutron source has 1cm distance.

3.3 Simulated gamma ray energy deposition in semiconductor sensors

Gamma rays are produced by transitions from excited states in a nucleus. Such excited states can be created by nuclear reactions and by radioactive decay. When de-excitation follows in lower energy states in the same nucleus, either α or γ particle is emitted, or the energy is transferred to an atomic electron. Gamma rays have typical energies from a few keV to approximately 8MeV, the electromagnetic radiation with the energy above 100 keV is referred to as γ -radiation. High energy experiments as well as both fusion and fission reactors are gamma ray sources. They can contaminate the spectrum of the detector response in neutron detection applications. As mentioned in subsection 2.1 neutron detectors must be able to distinguish neutrons with photons, so low Z materials are preferable. Their signals are able to overlap with the neutron spectrum and lower the efficiency and increase deviations. Neutron diagnostics are usually accompanied by thresholds to reject the emitted gamma rays, typically at 0.5MeV.

Gamma rays mainly interact through photoelectric effect, Compton scattering and pair production. During **photoelectric effect** a photon of a few hundreds keV interacts with an atom, in which the photon disappears completely and a photoelectron is rejected by the atom in one of its bound shells. The photoelectron appears with an energy given

by: $E_e = hv - E_b$, where E_b corresponds to the binding energy of the photoelectron. In **pair production** gamma rays above 1.02MeV are required. It becomes predominant as the energies increase to the many MeV range. In this process a photon disappears and is replaced by an electron-positron pair. After losing its kinetic energy the positron combines with the electron in an annihilation process which releases two gamma rays of 0.511keV. These photons may interact further with the material or escape.

Compton scattering takes place between the incident gamma ray photon and an electron of the material. The photon is deflected through an angle ϑ and transfers a portion of its kinetic energy to the electron recoil. The interaction is possible in all the angles, so the energy transferred can vary from zero to a large fraction of the gamma ray. The amount of energy exchanged is given by the formula:

$$\frac{1}{E'} - \frac{1}{E} = \frac{1}{m_e c^2} (1 - \cos\theta) \quad (3.1)$$

or

$$E' = \frac{E}{1 + \frac{(1-\cos\theta)E}{m_e c^2}} \quad (3.2)$$

- E is the energy of the incident photon
- E' is the energy of the outgoing photon, which escapes the material
- m_e is the electron mass
- ϑ is the photon deflection angle

The amount of interest is the energy transfer, $E_T = E - E'$ which varies according to the deflection angle: as ϑ approaches zero, none of the energy is transferred. The maximum amount of energy is transferred when ϑ approaches 180° where:

$$E_{compton} = E_{Tmax} = \frac{2E^2}{m_e c^2 + 2E} \quad (3.3)$$

It is impossible for the photon to transfer any more energy via this process, hence there is a sharp cutoff at this energy, which is called Compton edge.

The relative importance of these three major types of gamma ray interactions is presented below [29]:

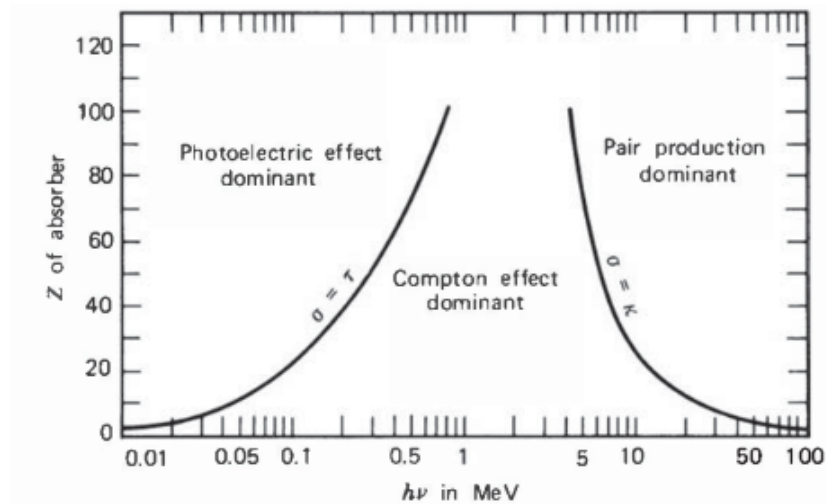


Figure 3.11: Relative importance according to Z , of pair production, Compton scattering and pair production. The lines show the values of Z and photon energies for which the two neighbouring effects are equal.

It is essential for any neutron detector to know how well it can distinguish gamma rays from neutron signals. To this end, three typical gamma ray energies were selected: 500keV, 1MeV and 2MeV and their energy deposition spectrum was collected for the diamond, Si and SiC detector. The aim of these spectra was to examine a possibility for a threshold, in order to receive only the desired neutron pulses. The spectra for the three materials are presented in figures 3.12,3.13,3.14.

It is worth mentioning that for 2.45MeV neutrons, gamma rays are produced during the inelastic scattering of Si. For $^{28}\text{Si}(n, n')^{28*}\text{Si}$ a gamma ray of 1.779MeV is produced. For $^{29}\text{Si}(n, n')^{29*}\text{Si}$ a 1.273MeV gamma ray is produced while for $^{30}\text{Si}(n, n')^{30*}\text{Si}$ a 2.235MeV. Of course for higher neutron energies a bigger variety of interaction channels are allowed, with the possibility of producing more energetic gamma rays.

500keV, 1MeV and 2MeV gamma rays mainly interact with Compton scattering according to 3.11. So in order to examine the produced spectra, equations 3.2 and 3.3 were used. For 0.5MeV gamma ray the Compton edge was found $E_{Tmax} = 0.33\text{MeV}$, for 1MeV gamma ray $E_{Tmax} = 0.79\text{MeV}$ which corresponds exactly to the simulated results. For 2MeV gamma rays the expected value of Compton edge is 1.77MeV, which is much higher than the simulated 0.8MeV. The reason behind this, is that the interaction probability and charge deposition with gamma rays drops significantly with increasing energy, or decreasing thickness. With photon energy above 1 MeV the interaction probability for a 500 μm sensor is below 1% [21], so at 50 μm sensors we don't expect contributions as the photon energy further increases.

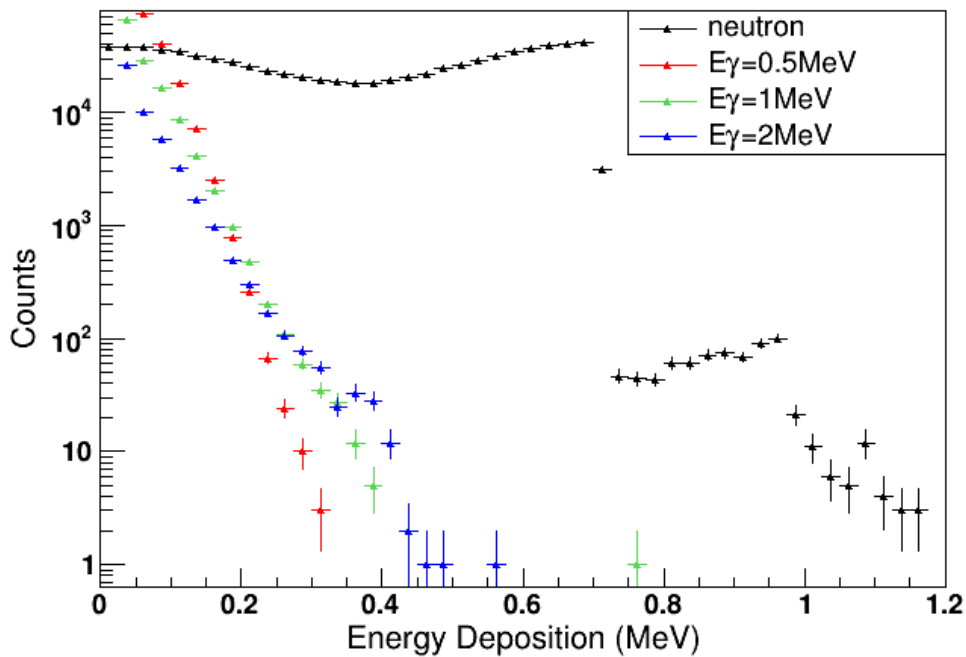


Figure 3.12: Energy deposition spectrum for 500keV, 1MeV and 2MeV gamma rays in a 50µm C detector. Neutron energy deposition spectrum is presented as well, with black points. We observe a possible threshold around 0.4MeV.

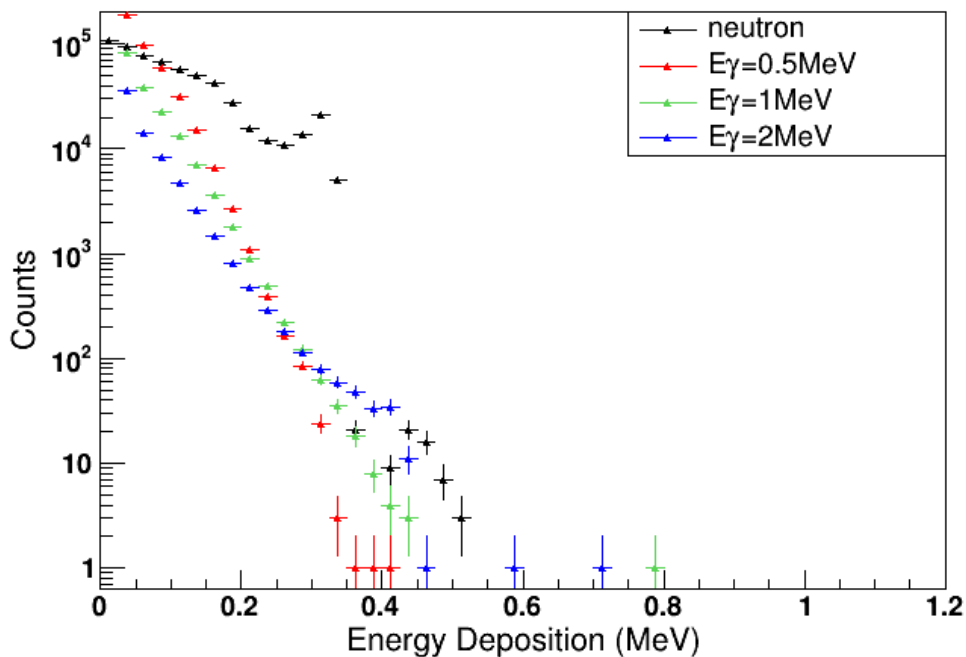


Figure 3.13: Energy deposition spectrum for 500keV, 1MeV and 2MeV gamma rays in a 50µm Si detector. Neutron energy deposition spectrum is presented as well, with black points. We observe that there is no clear threshold, the gamma spectra and the neutron overlap in almost all the energy ranges.

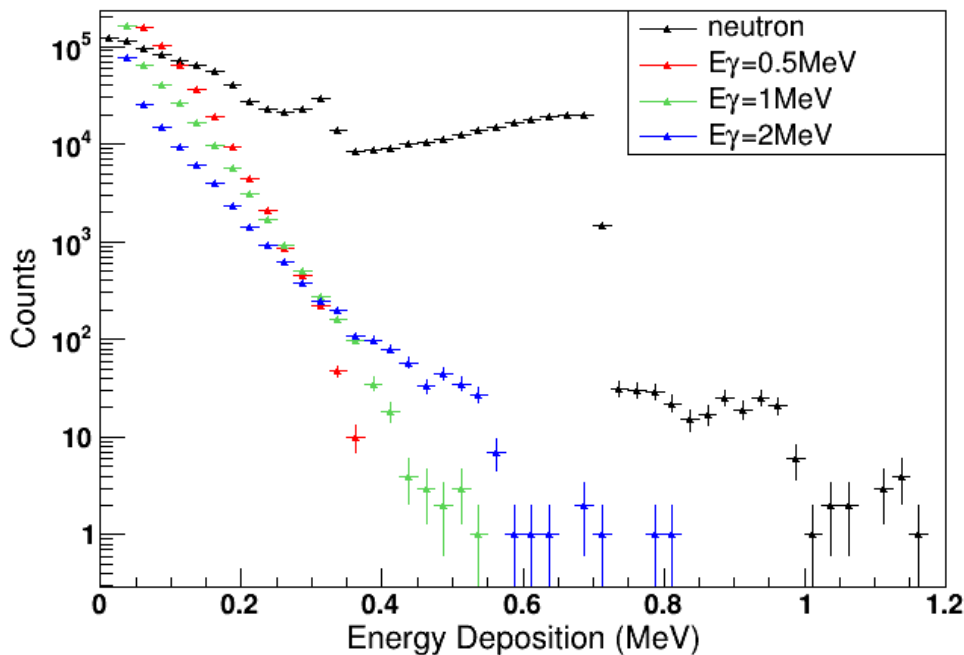


Figure 3.14: Energy deposition spectrum for 500keV, 1MeV and 2MeV gamma rays in a $50\mu\text{m}$ SiC detector. Neutron energy deposition spectrum is presented as well, with black points. We observe a possible threshold around 0.4MeV.

An important property of the diamond detector is the low interaction probability with gamma rays due to the low Z of the material. In figure 3.12 we observe a clear threshold around 0.4MeV. In these energies the gamma rays counts drop orders of magnitude and the neutron distribution become clear. In diamond technology it is obvious that we can obtain precise neutron spectra with a threshold even below 0.5MeV.

For the Si detector the gamma ray energy deposition spectrum is presented in figure 3.13. Although in intermediate energies, neutron spectrum is above the gammas, we observe that both in low and in higher energies neutrons overlap with the photons. Due to the higher Z than diamond, the low neutron energy and interaction probability, a clear gamma ray threshold cannot be obtained in Si.

SiC interactions with gamma rays are seen in figure 3.14. Due to the presence of carbon we observe once again a clear threshold around 0.4MeV. SiC as mentioned combines the interactions of both Si and C, so gamma rays interactions can easily be disguised in SiC based neutron detection.

Chapter 4

Preparation of experiment at the NCSR “Demokritos”

In this chapter the experimental setup of the TANDEM accelerator of the Institute of Nuclear and Particle Physics of the NCSR "Demokritos" and the simulation including the experimental proton line and the (p,n) reactions leading to a quasi-monoenergetic neutron beam are described. The biasing techniques used as well as the deviations from the corresponding analogue case are examined in great detail and finally, the resulting detector's response function and the efficiency are presented.

4.1 Experimental setup

The experimental setup is going to be neutron production facility of the TANDEM accelerator at NCSR "Demokritos". It consists of a linear accelerator based on a Van de Graaff generator, able to produce neutrons from charged particles. The basics of its operation are described in [30].

The neutron production facility produces quasi-monoenergetic neutron beams by the interaction of light ions with gaseous or solid targets, depending on the neutron energy of interest. For the production of 2.45 MeV neutrons, the ${}^3\text{H}(p, n)$ reaction is used. The accelerated proton beam interacts with a TiT target as shown in figure 4.1 producing a neutron beam. The proton beam comes through two small holes in order to align the beam, called collimators. The materials used as the collimators have high coulomb barrier, so nuclear reactions and further contamination is avoided. When the beam passes through two successive collimators, an alignment of a few mm is achieved. Antiscatterers are also in place to prevent further energy loss of the initial proton beam. The protons then enter the aluminium flange, where a TiT target is placed and through ${}^3\text{H}(p, n)$ reactions a quasi-monoenergetic neutron beam is produced.

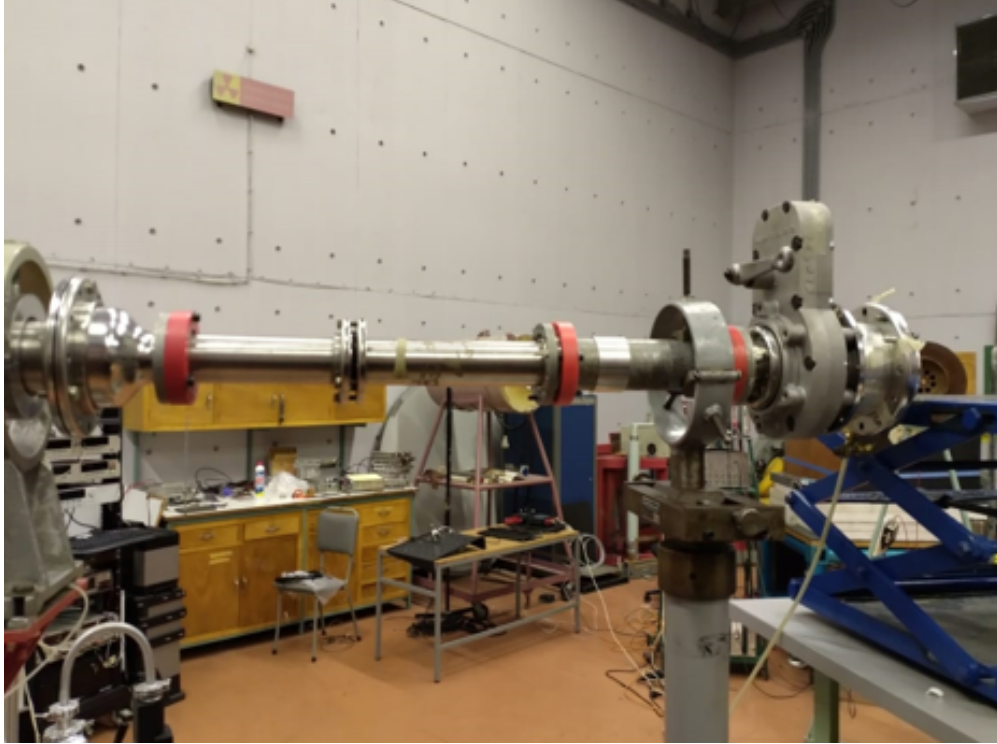


Figure 4.1: The end of the irradiation line in the experimental hall of the TANDEM accelerator Laboratory of NCSR "Demokritos" including the TiT target.

4.1.1 The neutron beam production

As mentioned above neutrons are produced through (p,n) reactions with the tritium the aluminium flange. Inside the flange three targets are in place. Protons first interact with a thin molybdenum foil followed by the main tritiated titanium target and then a thick copper target. The main neutron production occurs from (p,n) reactions with the 3H target, however (p,n) reactions may occur with Mo, Cu or Ti isotopes inside the flange. The probability of these reactions is low compared to 3H as shown in the following figures. The initial proton energy which was used in the simulations, was calculated with S.R.I.M. at 3.805MeV in order to produce 2.45MeV neutrons.

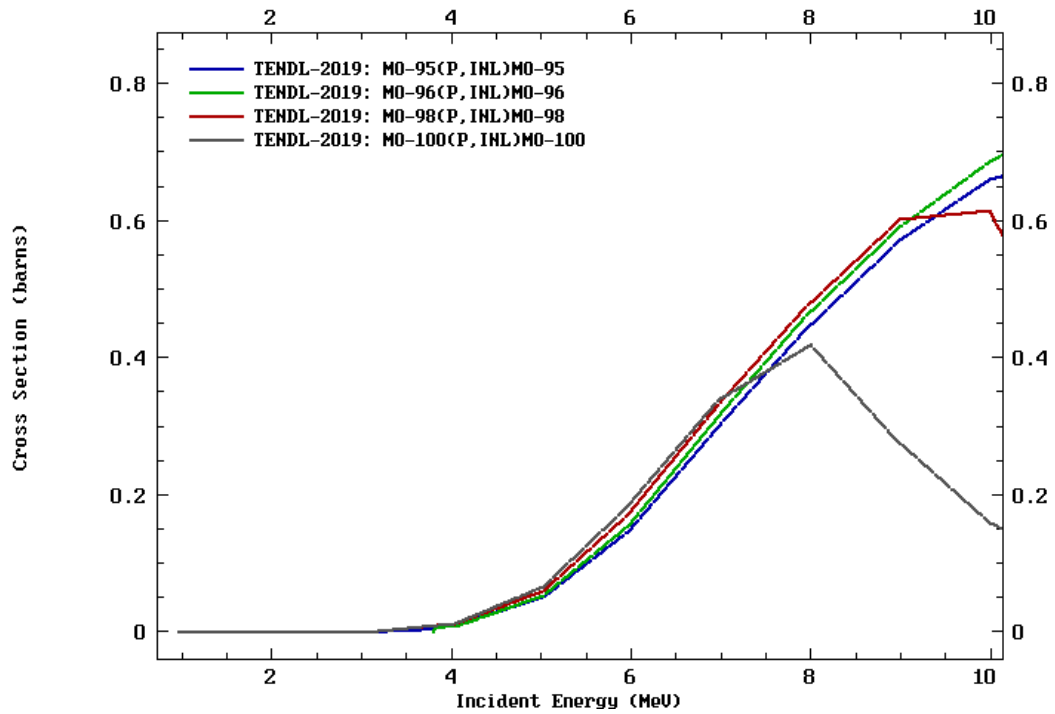


Figure 4.2: Cross section of the (p,n) reaction with Mo isotopes with incident proton energy. Evaluated data provided by TENDL database.

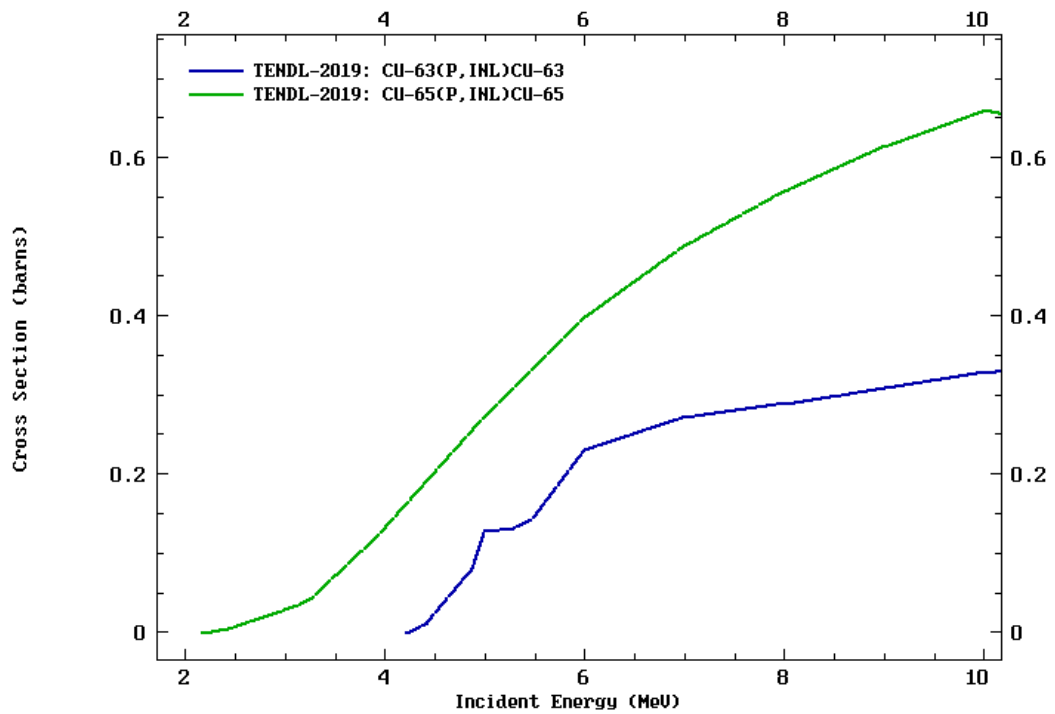


Figure 4.3: Cross section of the (p,n) reaction with Cu isotopes with incident proton energy. Evaluated data provided by TENDL database.

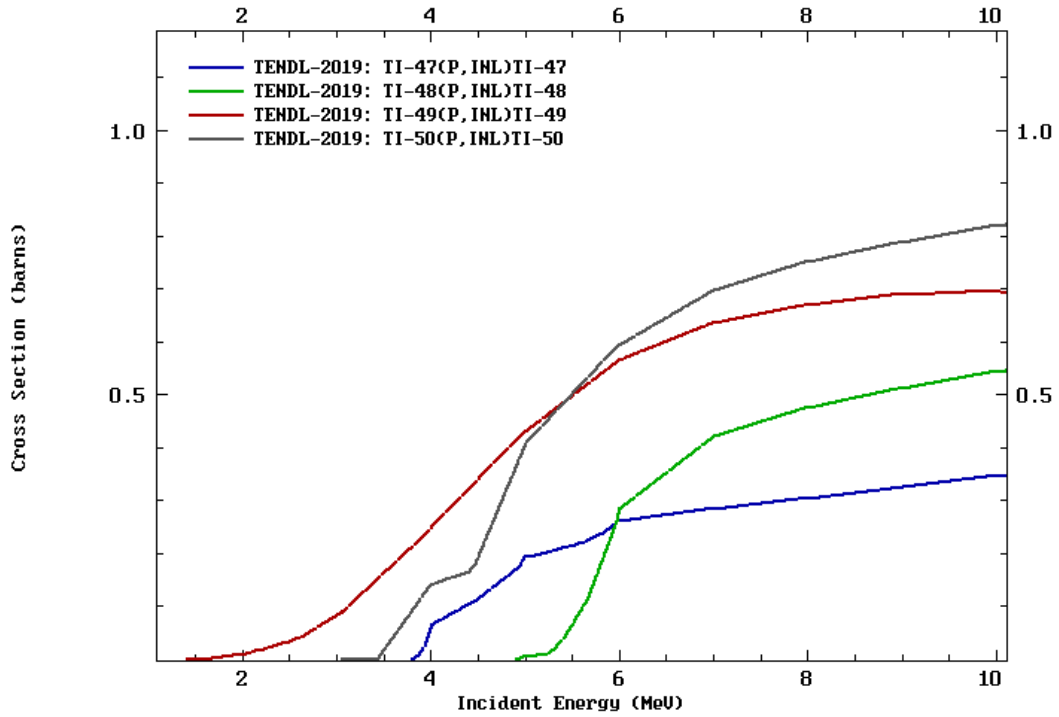


Figure 4.4: Cross section of the (p,n) reaction with Ti isotopes with incident proton energy. Evaluated data provided by TENDL database.

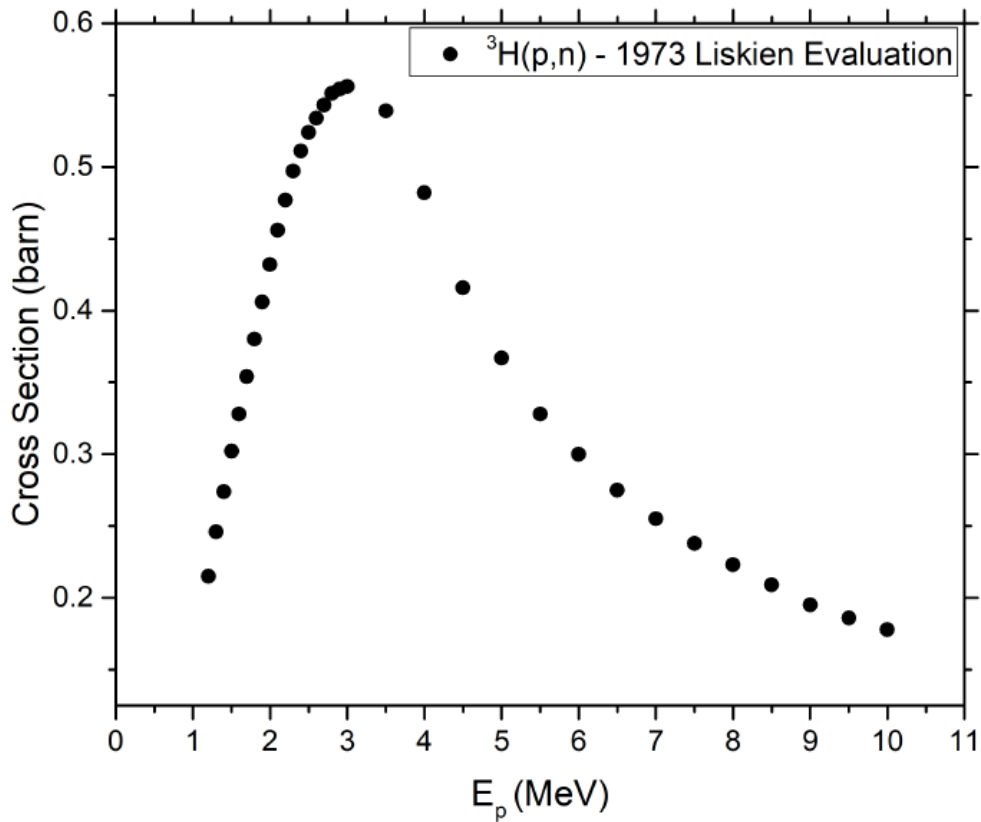


Figure 4.5: Cross section of the (p,n) reaction with ^3H with incident proton energy. Data provided by Liskien.

Protons enter the Mo target with energy $E_p=3.805\text{MeV}$. Observing the figure 4.2 for the Mo isotopes, the (p,n) reaction cross section is approaching zero so the contribution is at a minimum.

Inside the Mo target protons lose 491keV energy and they enter the TiT target with $E_p'=3.314\text{MeV}$. For the Ti isotopes a similar behaviour to Mo is observed and although the cross section is above zero the contribution is once again negligible. On the other hand a clear maximum is observed at the cross section of ${}^3\text{H}(p, n)$ as shown in figure 4.5 at approximately 3MeV, which makes this reaction favourable for neutron production. In addition the values of ${}^3\text{H}(p, n)$ cross section are bigger than all the other (p,n) reactions so the conclusion that neutrons originate from ${}^3\text{H}(p, n)$ is valid.

Inside the TiT target protons lose 152.054keV so they enter the Cu target with $E_p''=3.1619\text{MeV}$. For the Cu isotopes, as shown in figure 4.3 the cross section has small values for low energetic protons and it seems to be significant above approximately 5MeV or higher proton energy. Of course in higher neutron energies the parasitic neutrons generated by the other isotopes cannot be avoided.

4.1.2 The detector setup

The detector geometry is provided by CIVIDEC Instrumentation GmbH. The whole detector is shown at figure 4.6.

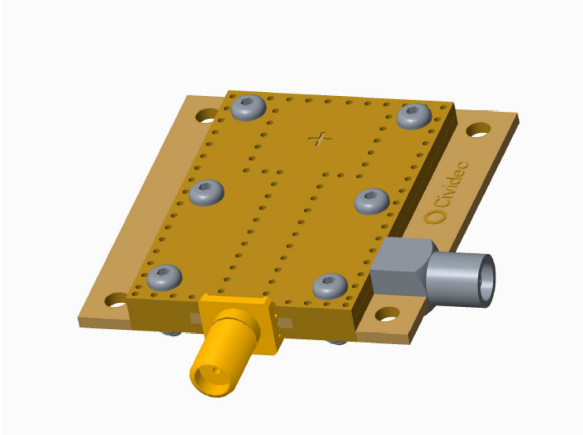


Figure 4.6: Detector geometry provided by CIVIDEC Instrumentation GmbH.

It consists of the main diamond, silicon or silicon carbide sensor and a sequence of Au,Cu and FR4 metalization layers. FR4 is a material used for electronic applications containing epoxy (H_2C_2) and SiO_2 so ohmic contacts will be provided between the detector layers.

The detector must interact with a high flux of the 2.45MeV monoenergetic neutron beam in order to provide high statistics. For this to be possible, the target must be placed in the right distance from the flange. This information derives from the differential cross section of the (p,n) reactions in ${}^3\text{H}$. ${}^3\text{H}(p, n)$ produces neutrons in a certain angular distribution deriving from Liskien [31] according to the

following formula:

$$\frac{d\sigma}{d\omega} = \frac{d\sigma}{d\omega}(0^\circ) \sum_i A_i P_i \quad (4.1)$$

Where:

- $\frac{d\sigma}{d\omega}(0^\circ)$: differential cross section at (0°)
- A_i : Legendre coefficients

- P_i : Legendre polynomials

The differential cross section in the laboratory system peaks at low angles and drops at 90° and higher. The neutron energy also drops and stops being monoenergetic for higher detecting angles. It can be shown that between an angular opening of $\pm 10^\circ$ the neutron beam behaves as a monoenergetic isotropic beam [32]. So the detector must be placed in close distance from the neutron source in order to receive a high flux but with a small angular opening, in order to interact with monoenergetic neutrons. For this work the detector was placed at 1cm distance from the neutron source. In this distance the neutron flux is high and the angular opening is at $\pm 10^\circ$, so these values consist the ideal conditions to achieve a relative monoenergetic and isotropic beam.

4.2 Geant4 simulations

In order to proceed with the simulations, the geometry described in sections 4.1 and 4.1.1 was build. The setup includes the experimental line presented in figure 4.1, thus the path of protons as they undergo (p,n) reactions is portrayed as shown in figure 4.7.

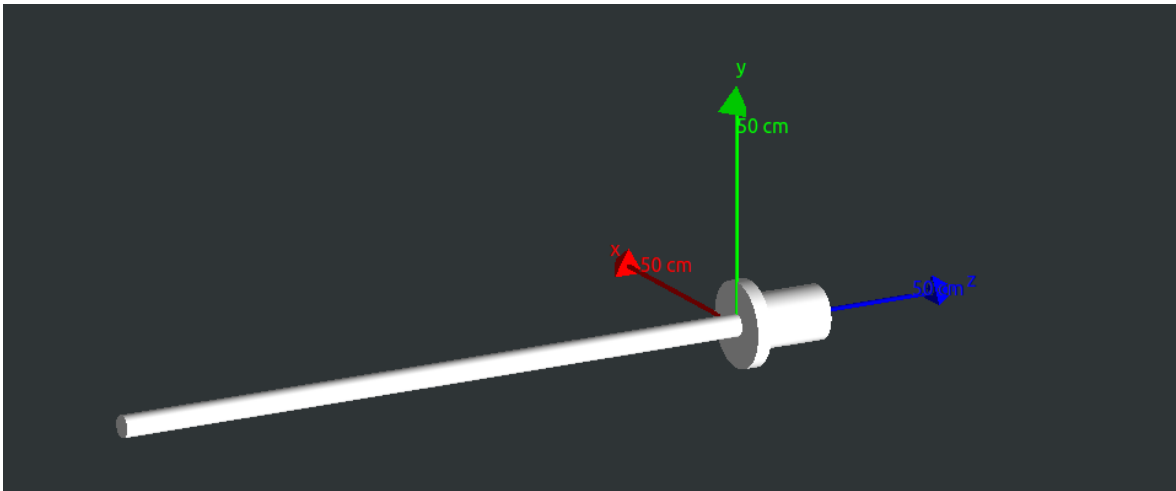


Figure 4.7: Geometry of the experimental line as drawn using GEANT4.

As mentioned the proton beam produced in the accelerator, interacts with a TiT target through (p,n), producing the desired neutron beam. In this setup first the **experimental line** was build by concentric cylinders with maximum diameter 3.18cm made of stainless steel. Inside this line, the **collimator** made of tantalum and its bases made of aluminium are built in order to align the proton beam. An **antiscatterer** was built, with a 1.4cm external radius made also of tantalum as well as its base, made of aluminium, to prevent further proton scattering and energy loss.

Next the aluminium **flange**, the main component of the set up, was built. As previously mentioned the first material the protons encounter when entering the flange, is a **molybdenum** foil with total thickness of 0.0005cm radius of 1.425cm. Molybdenum acts as the entrance window and depending on the proton energy, the first (p,n) reactions may occur. Its role is to moderate proton energy so the desired value of the ${}^3\text{H}(p,n)$ cross section is achieved. Immediately after the molybdenum, the **TiT** solid target is

placed, where the main (p,n) reactions occur and the majority of neutrons is produced. This target constitutes of 42.8% tritium and 57.1% titanium with a density of $3.75g/cm^3$, thickness 0.000285cm and radius of 1.27cm. Molybdenum also has the role to confine the 3H gas of the target. Right after the TiT target a foil of **copper** is placed, with thickness 0.05cm and 1.425cm radius. This foil acts as the beam stop for protons and if the energy is sufficient (p,n) reactions may occur with low probability as shown in section 4.1.1.

the detector with dimensions $4mm \times 4mm \times 50\mu m$ was placed at 1cm distance from the end of the flange. The material was carbon, silicon or silicon carbide respectively for simulating the desirable detector.

In the simulation the proton beam with $E_p=3.805MeV$ containing 10^9 primaries is generated in the beginning of the line, while scoring the neutron energy deposition in the sensor. Unfortunately due to the very low cross section only 4 to 5 neutrons were produced. The number of neutrons has to be high, at least 10^6 counts, in order to produce a realistic energy deposition spectrum in the thin detectors. In order for this simulation to be successful and to obtain high statistics, the implementation of biasing techniques were necessary.

4.2.1 Biasing Technique

Biasing techniques are used when rare events take place, due to the physics, meaning the low cross sections, or even the setup itself. Finding the efficiency of a very thin detector or generating a large number of particles from a low probability reaction constitute examples of rare events problems. An analogue simulation is very inefficient to address these problems, usually due to the extremely high computing time. Enhancing those rare events by the use of biasing results in achieving high statistics with significantly reduced CPU time.

There are two main methods of biasing:

- Importance Biasing: The probability distribution functions (pdfs) are modified enhancing the important parts of them and a different sample according to Monte Carlo method is achieved in favour of the rare events.
- Splitting (& Killing): The pdfs remain the same but the particles can be split or killed by moving towards the region of interest defined by the user.

When using biasing, the physical modeling is the same as the detailed simulation one. Biasing is simply another way to process the full detailed physics, so results obtained with biasing are statistically the same than the ones obtained with a large/huge processing of the standard simulation. However, when the physical processes are accessed, in order to achieve a small computing time, difficulties arise. With biasing all events don't have the same weight which causes most of the time convergence problems. An event with big weight may come, and change drastically the estimated analogue mean value. While the Monte Carlo efficiency increases, fluctuations are not correctly predicted. Deviations from the analogue case when the biasing techniques are used is an inescapable disadvantage, thus biasing should be used with caution.

In hardonic physics the option of cross section biasing is available in the GEANT4 simulation code, in order to enhance low cross sections. This process takes advantage

of the mean free length (λ) between two consecutive interactions that the particles undergo in a certain volume. The mean free length is given with the probability of each reaction through:

$$\lambda_t = \int_0^{\infty} xp(x) dx \quad (4.2)$$

Where:

- x: the mean distance the particle goes through matter until it interacts
- p(x): the probability of the interaction

The probability of a particle interacting at a length of dx, depends on total macroscopic cross section of the reaction according to:

$$p(x) = \Sigma_t e^{-\Sigma_t x} dx \quad (4.3)$$

The total macroscopic cross section is given by the microscopic cross section via the following equations:

$$\Sigma_t = \sum \Sigma_i \quad (4.4)$$

$$\Sigma_i(m^{-1}) = N(Nucleus/m^3)[\sigma_i(m^2)] \quad (4.5)$$

The microscopic cross section is affected by the energy of the incoming particle and the interacting nucleus, holding all the important physical parameters, thus it determines the interaction.

The macroscopic cross section is connected with the mean free path length via the equation 4.6:

$$\Sigma_t = \frac{1}{\lambda} \quad (4.6)$$

During the code development, the analogue cross section was defined as shown in equation 4.6. The biasing implementation was achieved by multiplying the value of $\frac{1}{\lambda}$ by a factor, called **biasing factor**. With this procedure the value of the macroscopic cross section is increased, while the mean free path length is decreased. The new biased cross section is then used at a specific volume according to the users need. The code was based on a GEANT4 example extended/biasing/GB01 and was updated so primary and secondary particles as well as many particle types in many different volumes can be biased.

While the increase of the cross section is desperately needed this type of biasing interferes with the distance in which the interaction takes place, altering some of the physical processes. As mentioned in the previous paragraph the mean interaction length is decreased, thus the particles interact in smaller depths in the given target. An increase in the biasing factor results to all the possible interactions taking place in the surface of the target. In this way the kinematics and the energy distribution can be significant altered and deviate from the analogue simulation. This deviation is depending on the shape of the cross section. When the interaction length is reduced the particle is forced to interact in the target's surface and thus with a different energy than the analogue case. If the cross section is relatively smooth this energy difference will cause small deviations, however in a shape where intense resonances are observed, the differences with the unbiased case will dramatically increase. In the case of a thin volume, where

the particles lose a small portion of their initial energy it would be likely to apply a high biasing factor, however the shape of the cross section must always be examined.

As mentioned when using biasing techniques a deviation from the analogue case is expected. A detail investigation is needed to determine the least acceptable deviation. In the next sections this analysis takes place, in order to extract the neutron response function for the diamond, silicon and silicon carbide detector with the realistic neutron source.

4.2.1.1 Biasing the neutron production

Using the experimental setup described in section 4.2 biasing techniques were used for enhancing the neutron production. In order to achieve a large number of (p,n) reactions the primary proton beam was biased inside the TiT target. As mentioned the produced neutrons, from 10^9 proton pencil beam, are in the order of 4 to 5, so a large biasing factor must be implemented to increase the neutron production by orders of magnitude.

From the discussion in section 4.2.1 it is clear that a thin target with a favourable cross section could withstand a large biasing factor. TiT has a thickness of 0.000285cm and the ${}^3H(p, n)$ cross section, shown in figure 4.5, presents no intense resonances. In the extremely thin TiT target protons will lose only 0.152MeV of their initial energy, so the value of the cross section will not be greatly affected. In conclusion, a large biasing factor can be implemented for biasing the primary protons inside the TiT target.

The simulation for testing the biasing in the neutron production, involves 10^9 primary protons which are born in the beginning of the experimental line, the biased TiT target and a 50 μ m diamond detector for scoring the neutron energy deposition. The diamond detector was chosen because no intense resonances are observed in the neutron elastic scattering cross section as shown in figure 4.14. Since the neutron energy deposition was measured, due to the low statistics the neutrons were biased inside the C sensor with a biasing factor of nbf=100 (see section 4.2.1.2) in order to be able to observe deviations.

A number of different biasing factors in the TiT target were used, resulting in better statistics but higher deviations from the analogue case in the energy deposition spectrum. In this particular stage of the simulation, concerning the neutron production, the analogue case would require an extremely high number of primary protons, resulting in an unrealistic large computing time (run for weeks even months). Proton biasing factor pbf=100 is expected to exhibit the lowest deviation possible not in the expense of the computing time or statistics. So, a simulation with pbf=100 (23831 counts) was chosen as the analogue case for biasing the TiT target. The value of the pbf in the TiT target, obviously will not affect by the other two detector materials (Si,SiC).

So, various tests including the biasing factor, the energy deposition of the C detector and the deviation from the "analogue" case were made as shown in table 4.1. The whole geometry was tested only in void.

Proton Biasing Factor	Counts	Deviation %
900	183387	16.95
700	146981	13.49
500	110932	7.41
400	90660	5.14
300	69024	3.57
150	35599	0.41

Table 4.1: Different proton biasing factors with the recorded counts leaving energy deposition in a 50 μ m C detector and the deviation from the analogue case of biasing factor=100.

We observe that with decreasing biasing factor the deviation as well as the counts decrease. In this process emphasis is given on the number events produced in the detector as well as the shape of the collected spectrum for each biasing factor. The shapes must be in agreement with the "analogue" case to ensure that the physical processes are the same. For each biasing factor this exact comparison is made in the following figures.

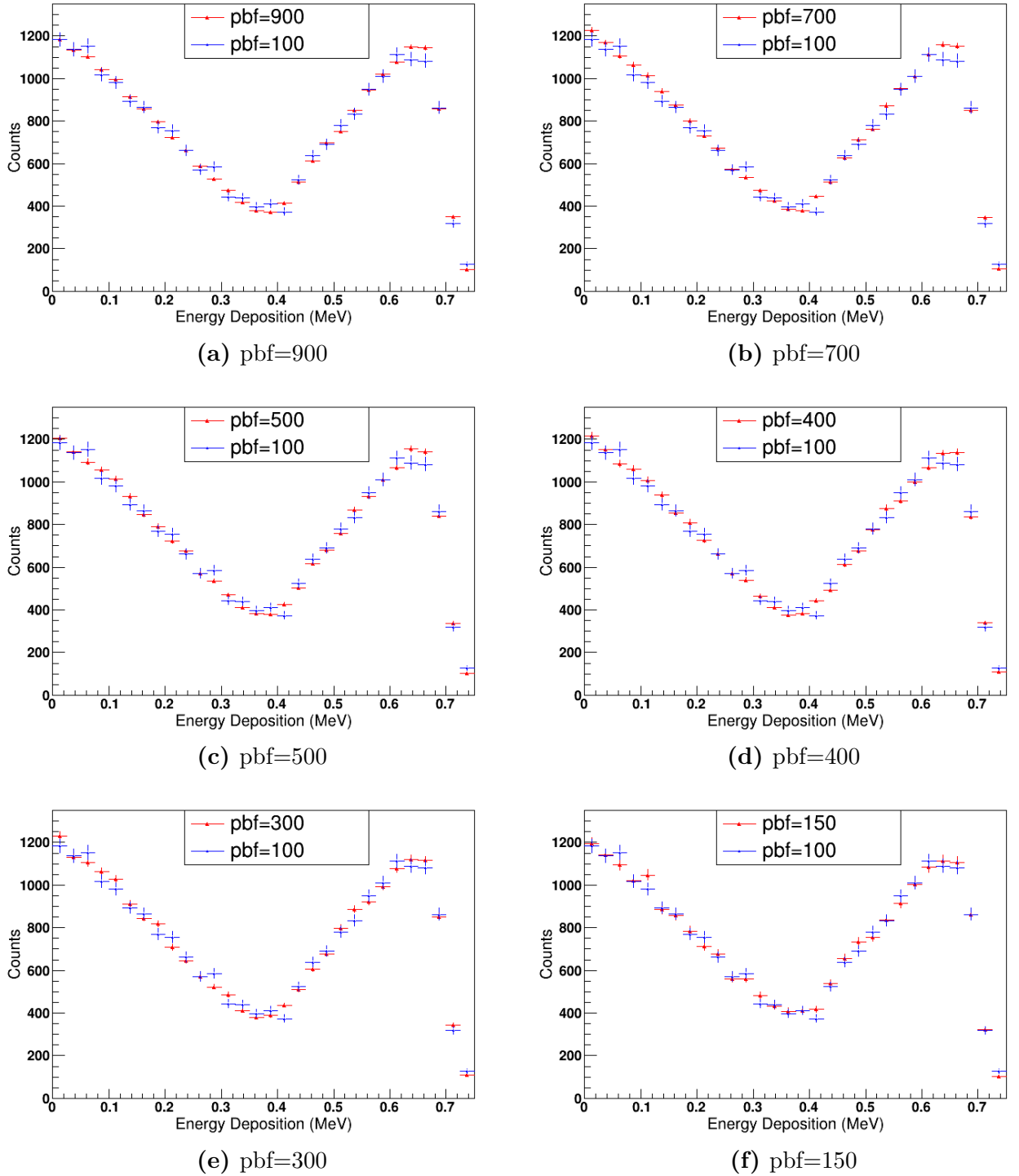


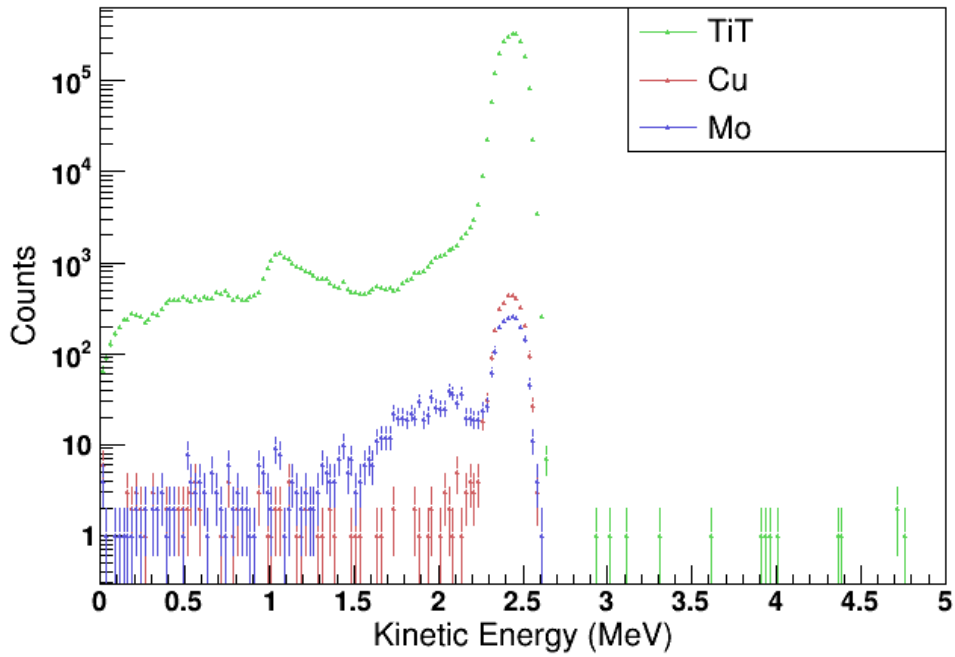
Figure 4.8: 2.45MeV neutron energy deposition spectrum for different proton biasing factors compared to proton biasing factor=100 in a 50 μ m diamond detector. The spectrum is zoomed in the primary elastic region. All the figures are normalised to biasing factor=100.

We observe that the spectra follow a similar distribution. This leads to the conclusion that the physical processes happening are the same for each biasing factor with deviations shown at table 4.1. The counting rate needs to be as high as possible to generate enough neutrons so they can produce a realistic energy deposition spectrum. With all

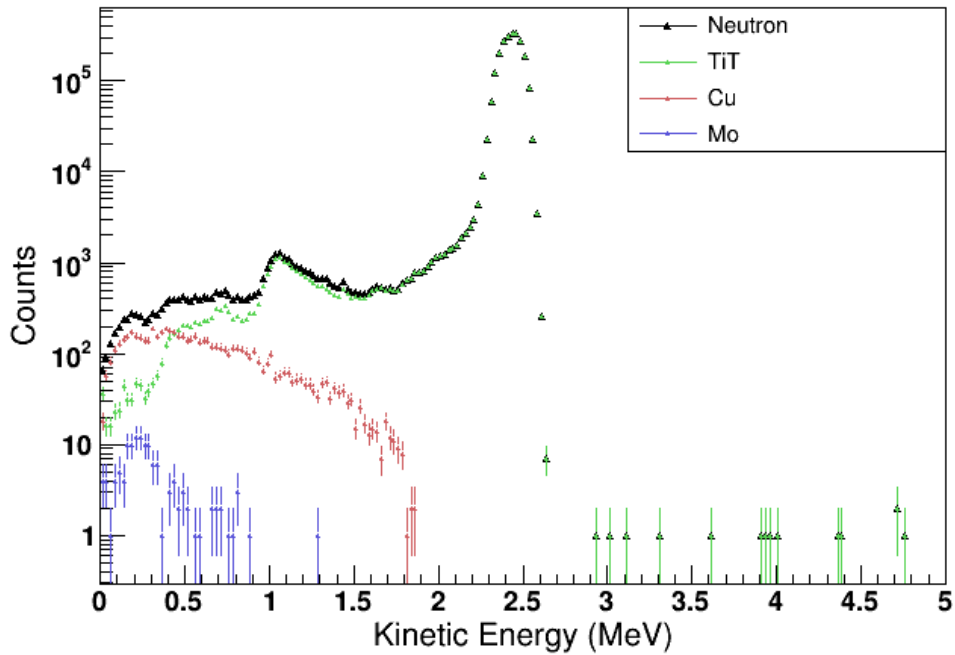
of the above in mind the biasing factor $\text{pbf}=900$ was selected. The deviation up to 16.95% was determined tolerable in this stage of the simulation.

Producing neutrons with biasing the TiT target will result in a realistic neutron beam interacting with the given detector. In order to analyse the neutron beam, all the targets inside the aluminium flange must be biased. So proton biasing factor 900 was implemented separately in Mo and Cu targets. Their contribution in neutron production is very low, however these reactions must be taken into account for the complete neutron spectrum. The assumption that Mo thin target can withstand such high biasing factor is correct, in contrast to the thick Cu target where biasing should be analysed differently. However the low, almost negligible contribution for the Cu target, provides the freedom for implementing a high biasing factor without affecting the final neutron beam.

So, three different runs were performed, each time biasing the Cu, Mo, TiT target respectively. The effect caused by each target in the neutron production is shown in the following figures.



(a) Neutron beam produced by biasing the protons by $\text{pbf}=900$ inside the TiT, Cu, Mo targets in three different runs.



(b) Final neutron beam deriving from biasing the TiT target by $\text{pbf}=900$, with contributions from Mo and Cu target.

Figure 4.9: Realistic quasi-monoenergetic neutron beam produced by (p,n) reactions at the experimental setup of NCSR "Demokritos" for a $50\mu\text{m}$ detector.

We observe that the main neutron production is from the TiT target as suspected in section 4.1.1. The clear peak at 2.45MeV is the production of 3.314MeV protons

interacting via the ${}^3H(p, n){}^3He$ reaction. This peak is observed in all three materials (figure 4.9a), as expected and it holds the majority of the counts. When the biased target is the Mo or Cu the protons still favour the interactions with 3H , leaving the characteristic peaks in both of the materials with obviously reduced counts.

The high energy neutrons observed in the biased TiT spectrum exhibit a certain interest. Due to the large number of neutrons produced, an equal large number of 3He is also produced. Due to these high numbers, through quantum channelling fusion between 3H and 3He can be achieved with $Q_{value}=2.47MeV$. This exothermic reaction can generate a few neutrons with energies up to 5MeV.

The low energy neutrons are attributed to the secondary reactions with the other targets as well as the variety of neutron energies produced in the ${}^3H(p, n){}^3He$ reaction, from 0.58MeV to 3.026MeV according to kinematics. Also struggling of the proton beam [29] as goes through the Mo or TiT targets, or the scatterings from the aluminium surrounding the flange, could cause a variation in the neutron energies produced.

In figure 4.9b the biased TiT target with $pbf=900$ is shown in greater detail. The neutrons born in the Cu and Mo targets are represented as well and we can see that their contribution is minor in contrast to TiT neutrons. The black points are the final neutron beam, which will interact with the three detector materials.

In this stage of the simulation a realistic neutron beam was produced. The figures in 4.9 demonstrate all the different energies in which neutrons will interact with the C, Si and SiC detector. The counting number has effectively been increased, however the number of neutrons interacting with the three materials and leading to energy deposition is extremely low. In order to collect the energy deposition spectra with sufficient statistics, additional biasing in the neutron detection is necessary.

4.2.1.2 Biasing the neutron detection

After producing a realistic neutron beam, as shown in 4.9, by biasing the (p,n) reactions in the TiT target, the statistics have improved, however 10^7 unbiased neutrons are not enough to produce the energy deposition spectrum. From 10^9 primary protons biased with a proton biasing factor $pbf=900$ only 5 to 10 neutrons manage to leave energy in the target. So the implementation of biasing in the neutron detection was deemed necessary. In contrast to section 4.2.1.1 the analogue case for neutron detection is, by good approximation, the 10^9 neutron pencil beam with $En=2.45MeV$ energy deposition spectrum which was studied in section 3.2.

For the **C detector** various combinations of primary neutrons and neutron biasing factors were made, measuring the counts leaving energy deposition as well as the deviation from the analogue case (10^9 unbiased neutrons). The primary particles and the biasing factors were chosen accordingly, so that their product will be 10^9 . For example: 10^6 primary neutrons times 1000 biasing factor = 10^9 neutrons. Biasing factor works as a multiplier of the primary particles, so with the right combination we expect the same distribution as the analogue case. Deviations of course are expected due to the variation in kinematics caused by biasing. The results for the C detector are shown in the table below.

Primary Particles	Biasing Factor	Counts	Deviation %
10^6	1000	554498	31.46
$2 \cdot 10^6$	500	665376	17.75
$2.5 \cdot 10^6$	400	690268	14.68
$3.33 \cdot 10^6$	300	716810	11.40
$5 \cdot 10^6$	200	746168	7.77
10^7	100	775672	4.12
$5 \cdot 10^8$	2	806940	0.26

Table 4.2: Different combinations of neutron biasing factors and primary neutrons with the measured counts leaving energy deposition and the deviation from the analogue case of 10^9 unbiased neutrons for a 50 μ m C detector.

We observe that as the number of primary particles increases and the biasing factor decreases, the deviation from the analogue case decreases as well. The recorded counts increase with the primary particles, as expected, and their numbers are of the order of 10^6 , so the statistics is already improved. In this stage of the simulation emphasis was given to a small deviation from the analogue case, in order to produce an accurate energy deposition spectrum. A deviation of 10% maximum was considered acceptable in these results. As mentioned in section 4.2.1 with the implementation of biasing, computing time is decreased. The unbiased case of 10^9 neutrons was running an average of 7h, whereas the computing time for the biased tests containing 10^6 to 10^8 primary particles was from 3min to 15min respectively.

In table 4.2 we observe that the deviation drops below 10% for bf=200. This leads to the conclusion that a relatively high biasing factor without changing the physical processes involved, can be used in the carbon detector. For visualisation of these results the unnormalised figures for each combination of biasing factor and primary particles were made and compared with the analogue case, as shown in figure 4.10.

The large deviation is clear for the small numbers of primary particles and high biasing factors. As the nbf drops to 100 4.10f the biased and the unbiased spectra almost overlap and the deviation is 4.12%. For the lowest biasing factor possible (bf=2) fig 4.10g, an even better agreement with the analogue case is observed. Taking into account the small deviation and the counts/computing time gain from a large biasing factor, bf=100 was chosen for the C detector.

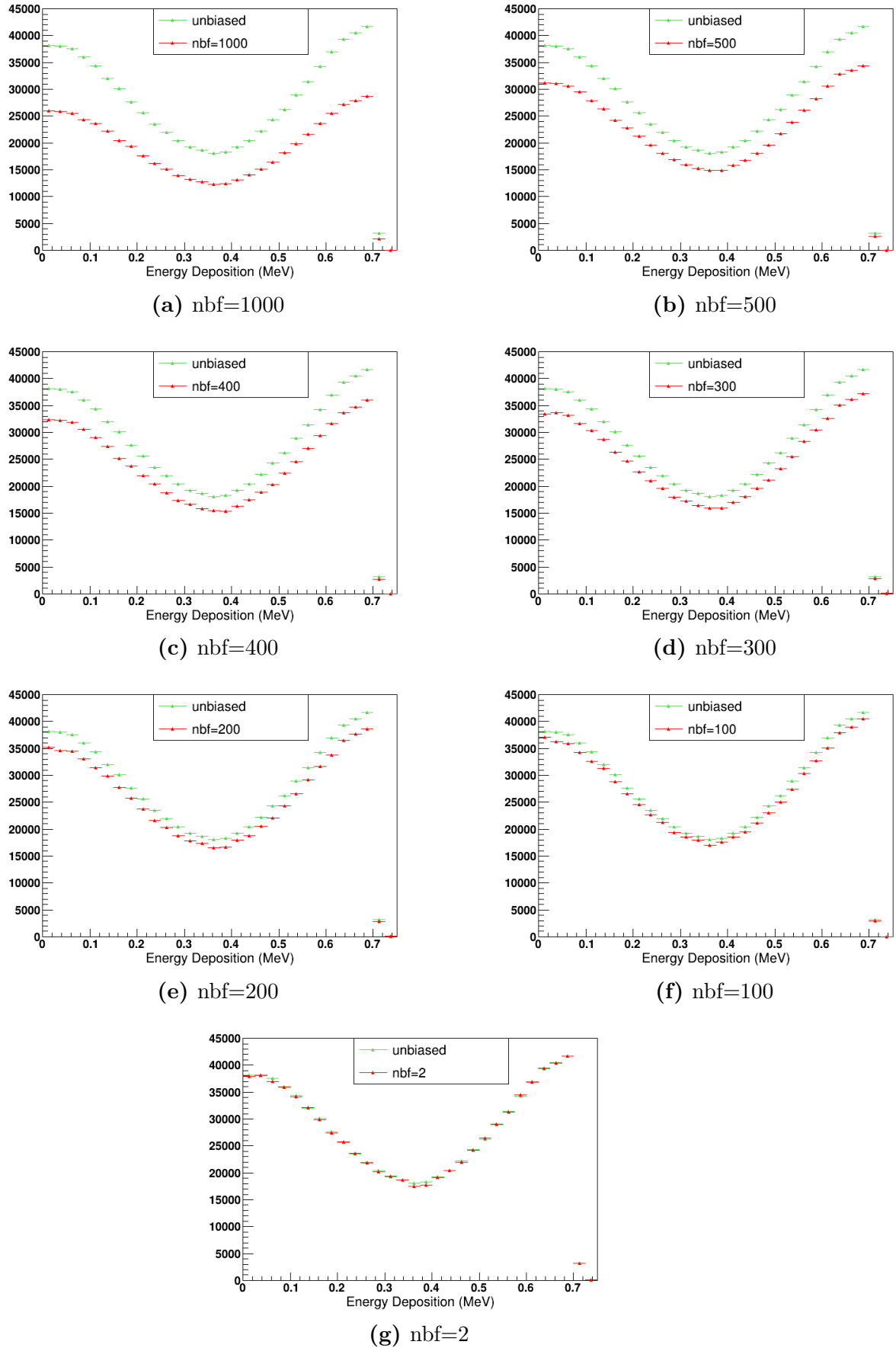


Figure 4.10: 2.45MeV neutron energy deposition spectrum for different neutron biasing factors compared to the unbiased spectrum for a 50 μ m C detector. The spectrum is zoomed in the primary elastic region.

A similar work was made for **Si detector**. The right combination of primary neutrons and biasing factor was made, recording the counts of energy deposition in the detector as well as the deviation from the analogue case, of 10^9 unbiased particles interacting with the Si target as discussed in **3.2**. The results are shown in the table below.

Primary Particles	Biasing Factor	Counts	Deviation %
10^6	1000	371707	38.33
$2 \cdot 10^6$	500	414580	31.22
$2.5 \cdot 10^6$	400	423771	29.69
$3.33 \cdot 10^6$	300	443105	26.48
$5 \cdot 10^6$	200	444764	26.21
10^7	100	455485	24.43
$2 \cdot 10^7$	50	462051	23.34
10^8	10	476937	20.87
$5 \cdot 10^8$	2	533025	11.56

Table 4.3: Different combinations of neutron biasing factors and primary neutrons with the measured events leaving energy deposition and the deviation from the analogue case of 10^9 unbiased neutrons for a $50\mu\text{m}$ Si detector.

Due to higher deviations observed from C detector, more tests were necessary for the Si case. Implementing each time a higher number of primary particles and a lower biasing factor. It seems that the physical processes happening in Si are greatly affected by the biasing techniques which will be explained in the following figures. With high biasing factors fig. 4.11 the distributions exhibit large shifts from the analogue case. With lower biasing factors, fig. 4.12, the deviations continue to be high and only with $\text{bf}=2$ 4.12d the biased and unbiased spectra seem to be in agreement. We are lead to the conclusion that the smallest possible biasing factor can be used, $\text{bf}=2$, adding a deviation of 11.56% to the acquired spectra.

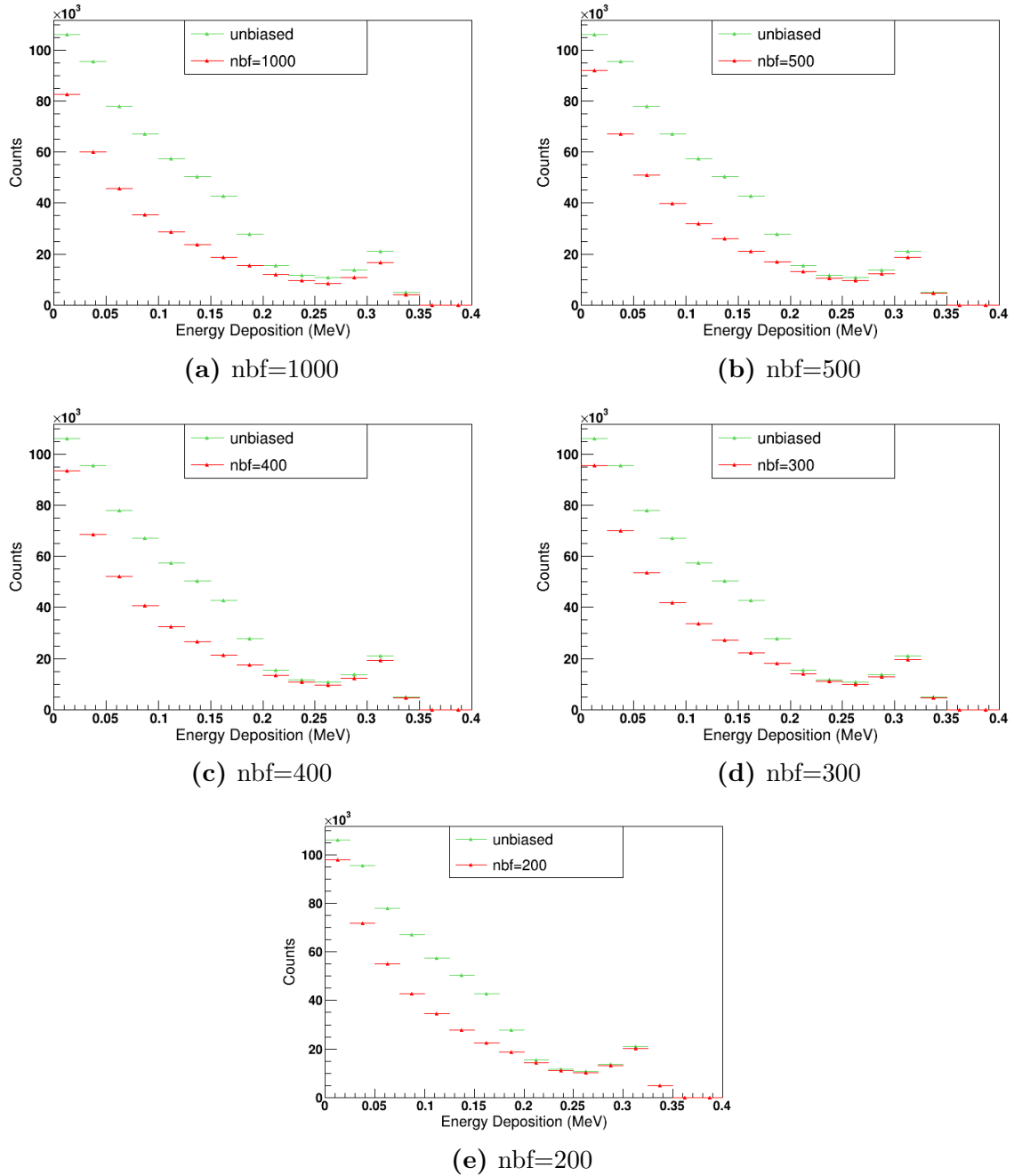


Figure 4.11: 2.45MeV neutron energy deposition spectrum for neutron biasing factors: 1000,500,400,300,200 compared to the unbiased spectrum for a 50 μ m Si detector. The spectrum is zoomed in the primary elastic region.

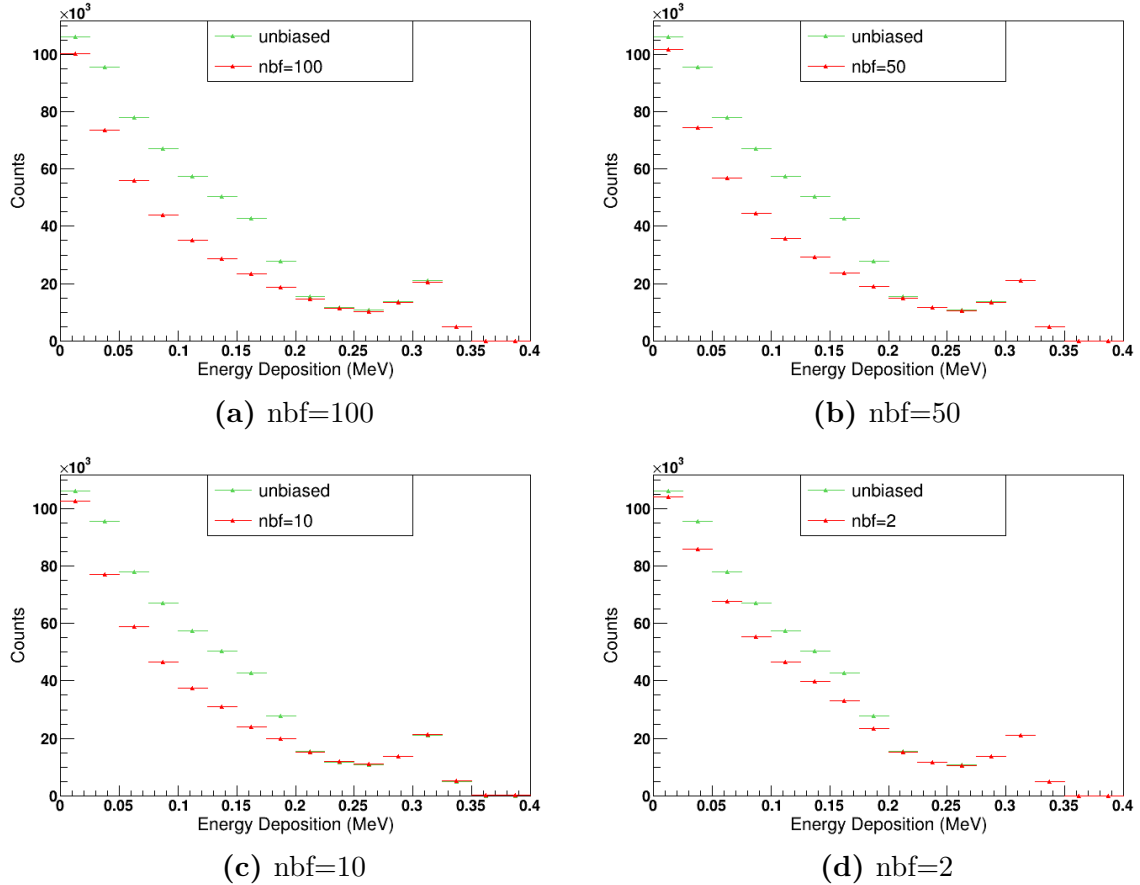


Figure 4.12: 2.45MeV neutron energy deposition spectrum for neutron biasing factors: 100,50,10,2 compared to the unbiased spectrum for a 50 μ m Si detector. The spectrum is zoomed in the primary elastic region.

For the **SiC detector** the resulting deviations from the analogue case are shown in table 4.4. Once again higher deviations are observed in contrast to the C detector, however as the biasing factor decreases lower deviations than the Si case are recorded. The obtained spectra and the comparison with the analogue case are shown in figure 4.13. In energies below 0.3MeV, where the silicon scattering dominates the spectra, high shifts are observed, similar to the Si sensor’s energy deposition spectra as shown in figures 4.11, 4.12. Above the 0.3MeV limit it is safe to assume that all the interactions occur with carbon nuclei. In these energy regions the shifts seem to be in better agreement with the analogue case as the biasing factor decreases. However, as the biasing factor decreases the deviations from the analogue case remain high, only in figure 4.13h the two spectra seem to be in agreement. The conclusion is the same as in the Si case that only the smallest biasing factor, $bf=2$, possible can be used so the smallest deviation of 7.03% is achieved.

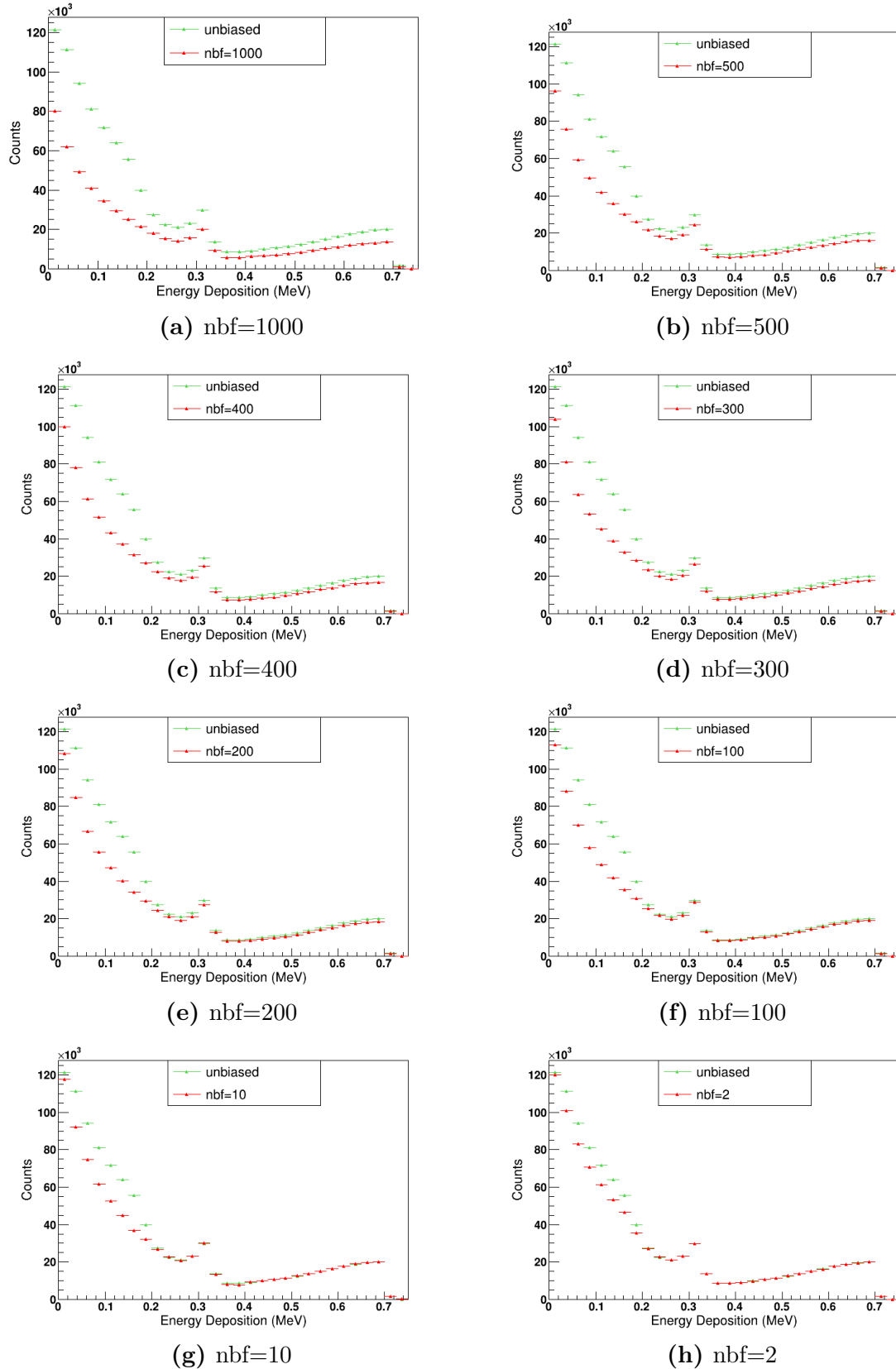


Figure 4.13: 2.45MeV neutron energy deposition spectrum for different neutron biasing factors compared to the unbiased spectrum, for a 50 μ m SiC detector. The spectrum is zoomed in the primary elastic region.

Primary Particles	Biasing Factor	Counts	Deviation %
10^6	1000	566785	41.64
$2 \cdot 10^6$	500	684304	29.53
$2.5 \cdot 10^6$	400	710550	26.83
$3.33 \cdot 10^6$	300	739154	23.89
$5 \cdot 10^6$	200	770258	20.68
10^7	100	802878	17.32
10^8	10	845549	12.93
$5 \cdot 10^8$	2	902857	7.03

Table 4.4: Different combinations of neutron biasing factors and primary neutrons with the measured events leaving energy deposition and the deviation from the analogue case of 10^9 unbiased neutrons for a $50\mu\text{m}$ SiC detector.

Comparison of the neutron detection in the three materials and explanation: we observe that carbon favours large values of biasing factor, in contrast to silicon and silicon carbide. In section 4.2.1 a reference was made to the physical quantities which affect the biasing factor. The shape of the cross section as well as the density of the materials seem to play a vital role in the tests performed. The biasing technique in our case, increases the macroscopic cross section while simultaneously reducing the mean interaction free length, thus the incident particles will be forced to interact closer to the target’s surface with a higher energy than the analogue case. The cross section depends strongly on the incoming particle’s energy. So different incident energies correspond to different values of the cross section, which leads to different physical processes and energy distributions.

In the analogue/unbiased case the neutrons interact with the three detectors with 2.45MeV. According to the mean interaction length (λ) inside the target, neutrons lose a part of their energy through collisions before interacting with the given nucleus, in a distance x , with $\sigma(E)$. Biasing forces the interactions to smaller λ , hence in higher energies than the analogue case, resulting in a different cross section $\sigma(E')$. All the important parameters responsible for the energy distribution belong to the value of the cross section. If this value is altered deviations will be observed by default. The degree of deviation depends strongly on the shape of the cross section, also the target thickness and the density of the material can play a vital role. With a smooth cross section, a thin target and a small density, the resulting spectra are not expected to significantly deviate.

In order to better understand this effect, the elastic cross section with neutrons is examined more carefully for C and Si. The neutron cross section with ^{12}C and ^{28}Si is first shown in 2.1 and 2.3. Focusing in the elastic and inelastic cross section and zoom in the energies near 2.45MeV figures 4.14 and 4.15 are obtained.

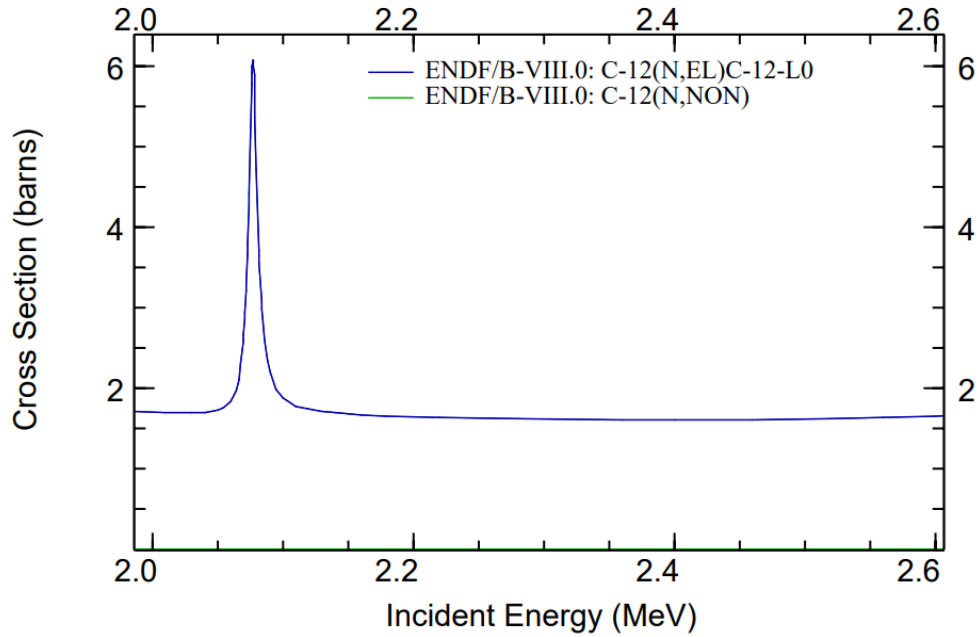


Figure 4.14: Neutron elastic cross section with ^{12}C zoomed in the energies of interest. Data obtained from ENDF database.

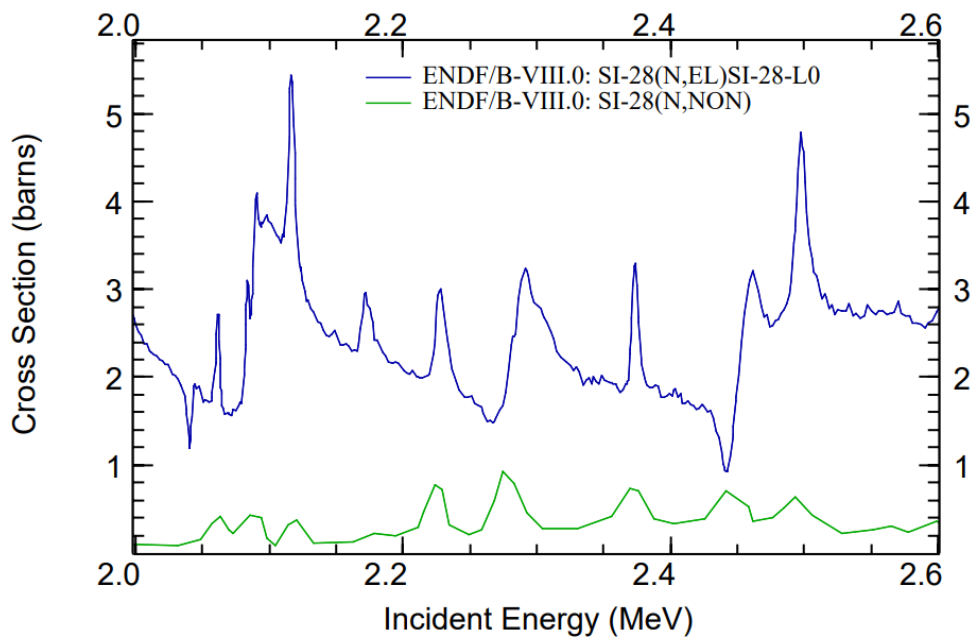


Figure 4.15: Neutron elastic cross section with ^{28}Si zoomed in the energies of interest. Data obtained from ENDF database.

For ^{12}C we observe that the elastic cross section follows almost a straight line until 2.1 MeV where a resonance is observed. The smooth shape of the cross section indicates that a small shift in the incident neutron energy will not affect the cross section values, hence the number and energies of the emitted particles. So in the case of C biasing factor doesn't affect the physical processes in such a high degree.

The cross section of ^{28}Si for neutron elastic and inelastic scattering is greatly different than the C case. Intense resonances are observed in very close energies. This means that a small shift in the energies due to biasing will have a huge effect as is imprinted in the deviations found.

Silicon carbide combines the features discussed in the previous paragraphs. The intense resonances of ^{28}Si affect the high deviations, however they are smaller due to the smooth cross section of ^{12}C . The effect of the high density of SiC ($3.2\text{g}/\text{cm}^3$) in contrast to the other two elements ($\rho_{\text{C}} = 2.1\text{g}/\text{cm}^3$, $\rho_{\text{Si}} = 2.3\text{g}/\text{cm}^3$) cannot be ignored. With higher density the incident particles come across a thick target, which affect both the energy distribution and the number of interacting neutrons.

4.2.1.3 Optimum combined result

In sections 4.2.1.1 and 4.2.1.2 various tests were performed to determine the most suitable biasing factor for neutron production and detection respectively. The aim of biasing is to construct a distribution as close as possible to the unbiased case, reducing significantly the computing time, while explaining the fluctuations between them. In order to enhance the neutron production, a biasing factor was implemented in the incident protons inside the TiT target. By choosing a high proton biasing factor (pbf) the neutron production is respectively high. In this stage pbf=900 was chosen (the highest of the factors used) with a deviation 16.95% from the analogue case. While the statistics of the neutron production was improved, still the counts of the energy deposition spectra for the three detectors was of the order of 10. So biasing the neutron detection with a neutron biasing factor (nbf) was implemented. The value of nbf was selected according to the smaller deviation from the analogue case, so the collected energy deposition spectrum would be as realistic as possible. In this section the optimum pbf and nbf for the C,Si and SiC detector is presented, also the deviations from the unbiased case are explained.

For the C sensor nbf=100 was chosen with a deviation up to only 4.12%. The cross section of neutron elastic scattering with ^{12}C nuclei has a smooth shape, as shown in figure 4.14, so high biasing factors can be used while causing low deviations. The resulting spectrum is presented in figure 4.16, where an immediate comparison to the unbiased neutron spectrum was made. The unbiased spectrum represents the simulations with a 2.45MeV monoenergetic neutron pencil beam, described in section 3.2, while the biased spectrum results from the quasi-monoenergetic neutron beam as shown in figure 4.9b including neutron energies from 0 to approximately 2.5MeV and a mean value of 2.405MeV.

The systematic error for the biased simulation was calculated from the corrections due to the biasing in the neutron production and detection through $1.1695 \cdot 1.0412$ at $\sigma_{\text{systematic}} = 21.76\%$ (biasing underestimates the recorded counts so all the corrections are amplifying the results). The statistical error was found $\sigma_{\text{stat}} = 0.23\%$.

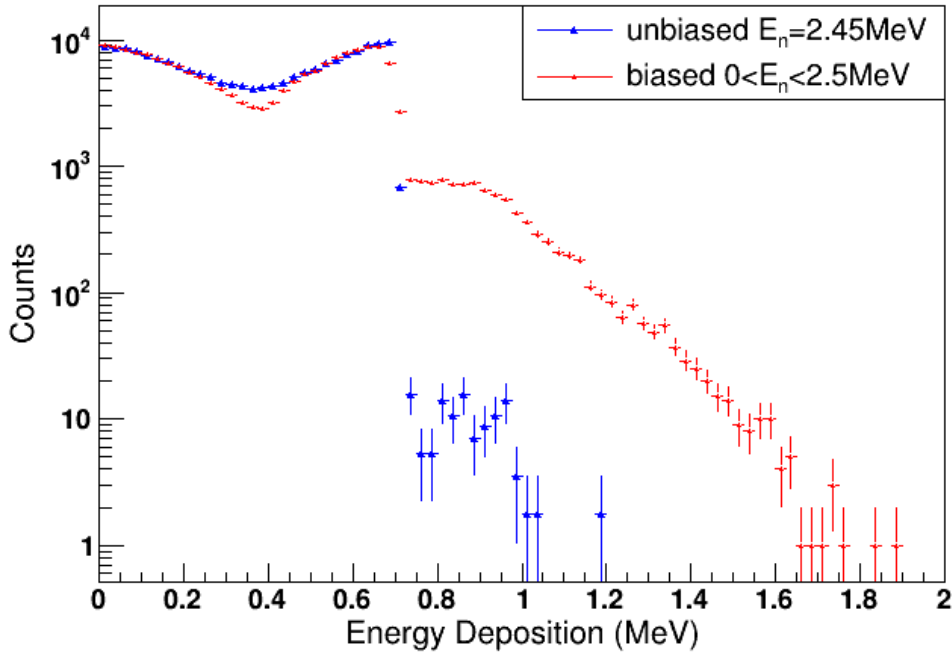
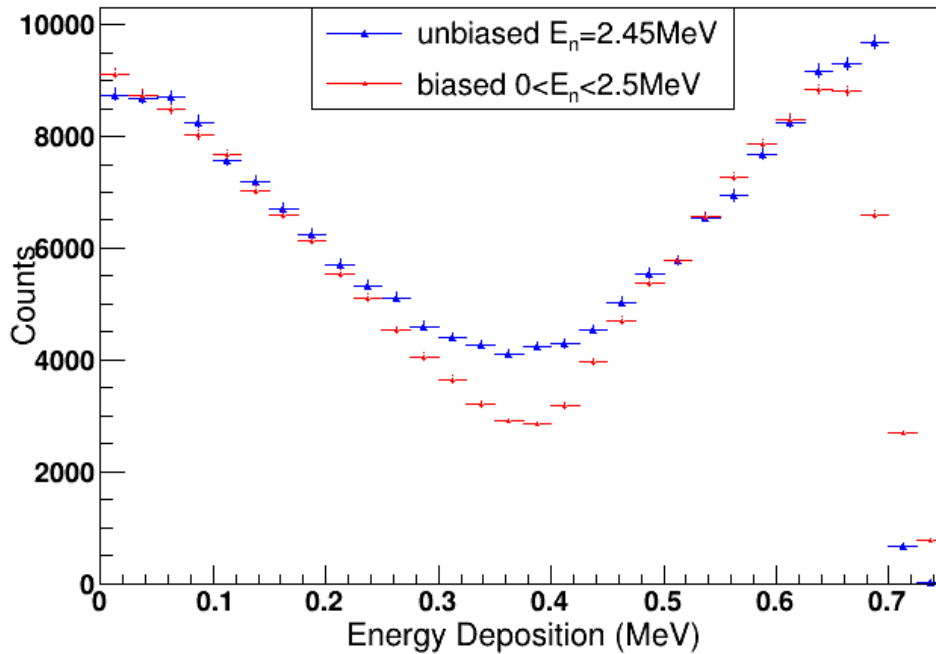


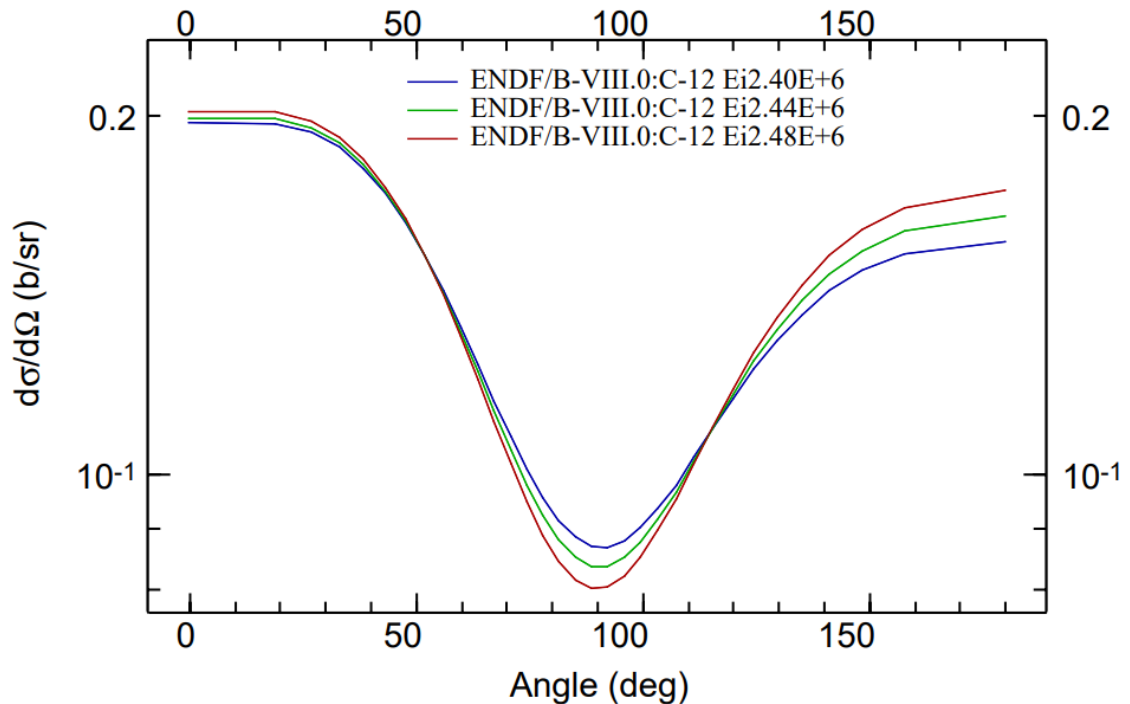
Figure 4.16: Biased neutron energy deposition spectrum, with $\text{pbf}=900$ and $\text{nbf}=100$, compared to the unbiased neutron spectrum for a $50\mu\text{m}$ C detector. The blue points derive from a 2.45MeV monoenergetic neutron beam with 10^9 primary neutrons. The red points are formed by 10^9 primary protons interacting with the TiT target, producing a variety of neutrons with mean energy of 2.405MeV as shown in figure 4.9b.

For C many differences are observed between the optimum biased and unbiased spectrum. First, in figure 4.16 the biased spectrum extends to higher energies than the unbiased. Implementing a high biasing factor will cause the majority of interactions to occur in the target’s surface. Because of the favourable cross section and the thickness of the sensor, the probability for two or three consecutive elastic scatterings inside the C sensor is increased. So, multiple scatterings are observed inside the target, thus leaving a higher energy deposition compared to the unbiased case.

In the low energy regions, the distributions show some significant fluctuations. In order to examine them closer, the shape analysis of figure 4.16 was performed, with a comparison to the neutron angular distribution for the elastic scattering with ^{12}C as shown in figure 4.17.



(a) Biased neutron energy deposition spectrum, with $\text{pbf}=900$ and $\text{nbf}=100$, compared to the unbiased neutrons for a $50\mu\text{m}$ C detector in linear scale. The blue points derive from a 2.45MeV monoenergetic neutron beam with 10^9 primary neutrons. The red points are formed by 10^9 primary protons interacting with the TiT target, producing a variety of neutrons with mean energy of 2.405MeV as shown in figure 4.9b.



(b) Angular distribution for neutron elastic scattering with ^{12}C for 2.4MeV , 2.44MeV , 2.48MeV neutron energy. Data obtained from the ENDF database.

Figure 4.17: Comparison of the energy deposition spectrum with the angular distribution for neutron elastic scattering with ^{12}C in multiple neutron energies.

In figure 4.17a the biased and the unbiased spectrum is shown in linear scale in the primary elastic region. Here the deviations are observed more clearly. Both in the small energy regions (0-0.2) and in the high (0.5-0.7), some counts from the biased spectrum seem above or below the unbiased case, while in the intermediate energies (0.2MeV-0.5MeV) the biased spectrum is clearly below the unbiased.

If we make the connection of these two spectra with the angular distribution in figure 4.17b, the unbiased neutron spectrum corresponds to the green line of 2.45MeV, the higher energetic neutrons 2.48MeV are represented with the red line and the lower 2.4MeV with the blue. It is obvious that these three neutron energies exhibit different behaviours throughout the distribution. If we chose higher or lower neutron energies similar angular distributions arise due to the smooth cross section. With this approach the comparison of the unbiased spectrum deriving from 2.45MeV monoenergetic neutron beam and the biased spectrum deriving from the quasi-monoenergetic neutron beam is made. The neutron angular distribution from elastic scattering has an immediate connection to the energy deposition spectrum.

In figure 3.3b, in small angles the 2.48MeV neutrons are observed above the 2.45MeV while 2.4MeV below which means that more energetic neutrons have a higher probability of emission in small angles. Applying the direct connection in the energy deposition spectrum in figure 4.17a, looking at the low energy regions (0-0.1MeV), which correspond to low neutron scattering angles, we observe some biased counts above and below the unbiased case, as the angular distribution suggests. Moving on to higher angles (up to 50°) the three spectra decrease and seem to overlap which is imprinted in the energy distribution spectrum at 0.1-0.2MeV energies where the decrease is observed and the biased and unbiased spectra almost overlap.

Above 100° a small rise and a similar overlapping is observed between the three neutron energies. The energy deposition spectrum 4.17a shows the same behaviour at energies approximately above 0.5MeV. Moving to even higher energies some points are above and some below the unbiased case, leaving the interpretation that both lower and higher energetic neutrons contribute to the spectrum.

In figure 3.3b we observe that in the intermediate angles from 70° to 100° the probability drops intensely for all the neutron energies. 2.48MeV neutrons are below 2.45MeV while 2.4MeV seem to be above all of them. It is expected that in figure 4.17a a similar behaviour should be observed, the lower energetic neutron, meaning the biased spectrum should be above the unbiased. However, the exact opposite is happening.

At 0.3MeV-0.5MeV energies, a big gap is observed with the biased spectrum being below the unbiased. This valley is due to the neutrons lost to double and triple scattering which are found in the tail of the C spectrum as shown in figure 4.16. Because of the high biasing factor used (nbf=100) and the thickness of the detector the consecutive elastic scatterings increase, causing the valley at intermediate energies. If we reduce the sensor's thickness the probability of these elastic scatterings decrease and the valley is shifted. This is shown in figure 4.18 where a 5µm with the same conditions is simulated in comparison with the 50µm. With decreasing thickness the drop of the distribution in the intermediate energies decreases and the spectrum is in better agreement with the angular distribution

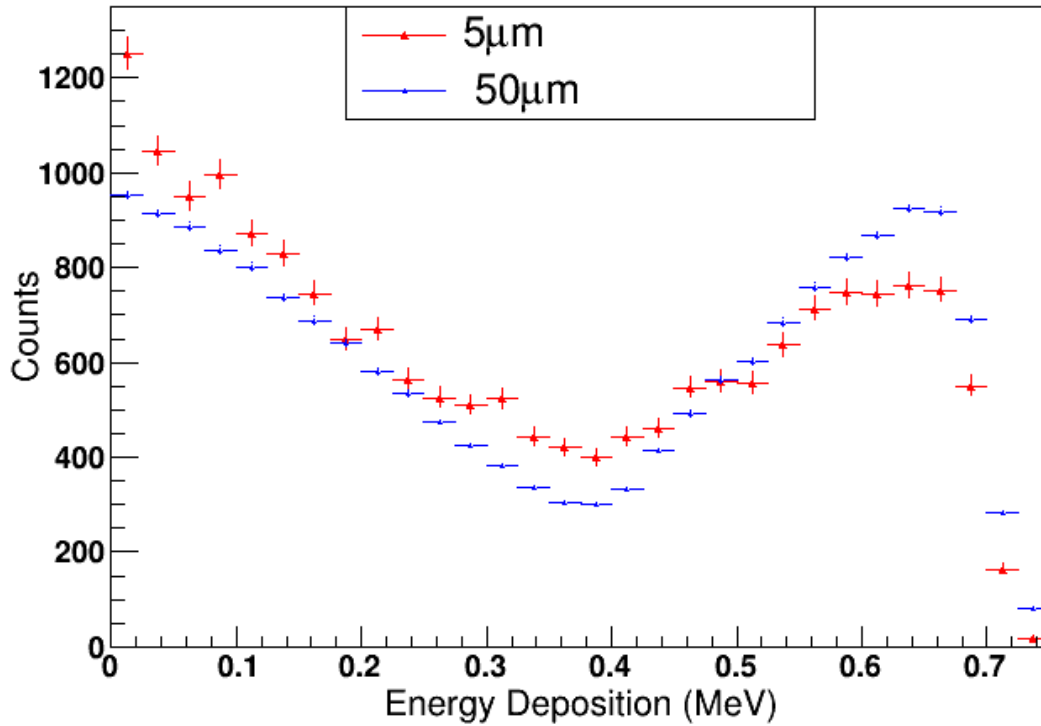


Figure 4.18: Biased neutron energy deposition spectrum, with $\text{pbf}=900$ and $\text{nbf}=100$, for a $50\mu\text{m}$ (blue points) and $5\mu\text{m}$ (red points) C sensor.

The same analysis happened for the **Si** sensor. In the neutron production the biasing factor remains the same since its dependence lies on the TiT target. For the neutron detection the smallest biasing factor $\text{nbf}=2$ with a high deviation of 11.56% was chosen. The intense resonances observed in the cross section of neutron elastic scattering with ^{28}Si nucleus, as shown in figure 4.15, cause fluctuations in the energy distribution with the use of a high neutron biasing factor. The final results for $\text{pbf}=900$ and $\text{nbf}=2$ are shown in the figures below.

The systematic error for the Si biased simulation was calculated from the corrections due to the biasing in the neutron production and detection through $1.1695 \cdot 1.1156$ at $\sigma_{\text{systematic}} = 30.46\%$. The statistical error was a bit higher than the C sensor due to the lower biasing factor used with the value of $\sigma_{\text{stat}} = 1.77\%$.

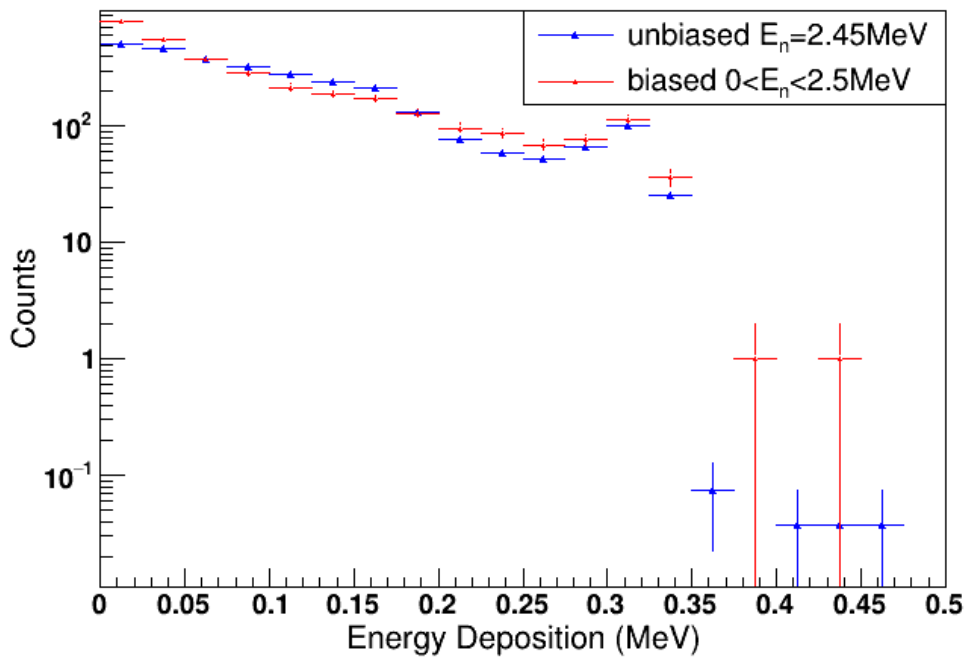
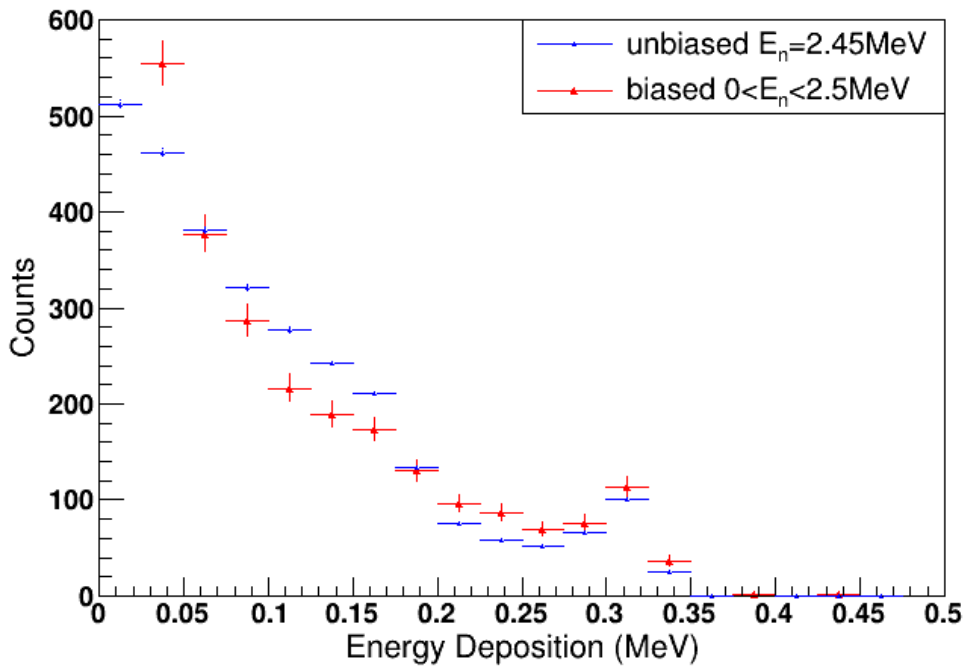


Figure 4.19

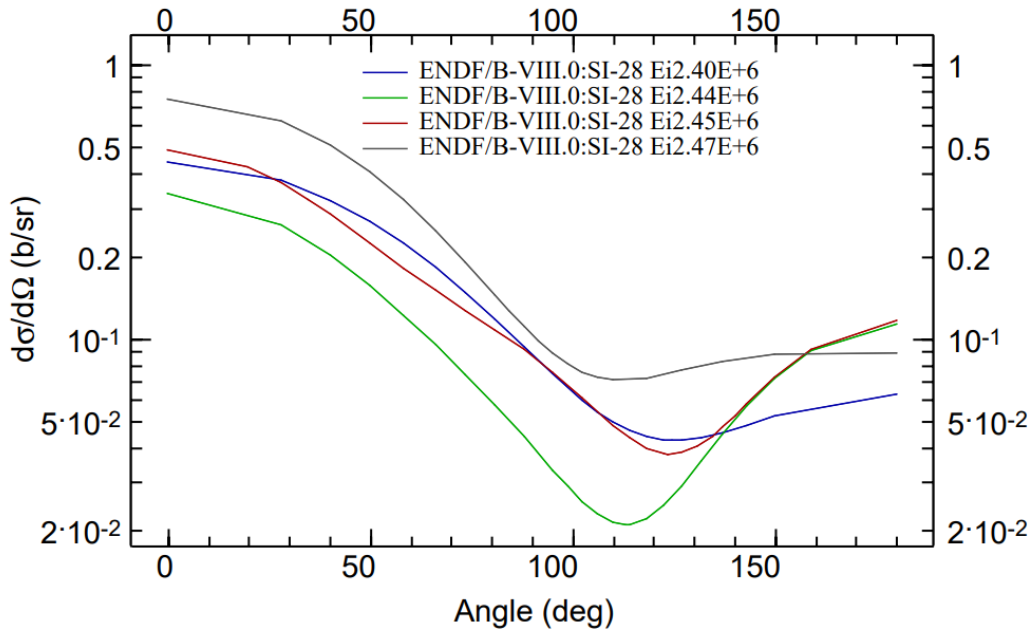
Figure 4.20: Biased neutron energy deposition spectrum, with $\text{pbf}=900$ and $\text{nbf}=2$, compared to the unbiased for a $50\mu\text{m}$ silicon detector. The blue points derive from a 2.45MeV monoenergetic neutron beam with 10^9 primary neutrons. The red points are formed by 10^9 primary protons interacting with the TiT target and producing a variety of neutrons with mean energy of 2.4MeV as shown in figure 4.9b.

Similar deviations are observed as the C case with a significant difference. The biased spectrum seem to stop in the same energy as the unbiased instead of extending in higher energies. Due to the shape of the cross section the multiple scattering effect cannot occur.

For the deviations between the biased and unbiased case the same reason was followed as the C sensor. The neutron angular distribution for elastic scattering with ^{28}Si was examined in four different energies as shown in 4.21b. Similar energies were chosen with the C analysis, so the neutrons above and below 2.45MeV can be examined.



(a) Biased neutron energy deposition spectrum, with $\text{pbf}=900$ and $\text{nbf}=2$, compared to the unbiased neutrons for a $50\mu\text{m}$ Si detector in linear scale. The blue points derive from a 2.45MeV monoenergetic neutron beam with 10^9 primary neutrons. The red points are formed by 10^9 primary protons interacting with the TiT target, producing a variety of neutrons with mean energy of 2.405MeV as shown in figure 4.9b.



(b) Neutron elastic scattering with ^{28}Si angular distribution for 2.41MeV (blue line), 2.44MeV (green line), 2.45MeV (red line) and 2.47MeV (gray line) neutron energy. Data obtained from the ENDF database.

Figure 4.21: Comparison of the energy deposition spectrum with the angular distribution for neutron elastic scattering in Si sensor at multiple neutron energies.

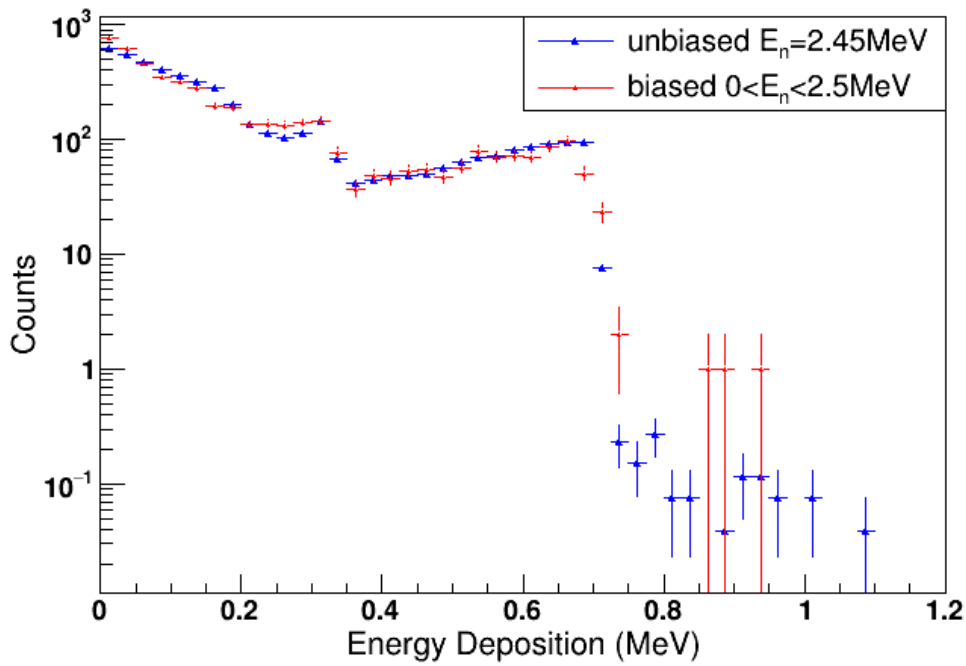
Due to the intense fluctuations in the cross section, angular distribution for slightly different energies is affected in a high degree, so four neutron energies were chosen: 2.41MeV, 2.44MeV, 2.45MeV and 2.47MeV. We observe that even at 2.47MeV neutron energies, intense deviations from the 2.45MeV neutrons are observed.

The unbiased spectrum of 2.45MeV neutron energy which is represented with the red line, is in some angles above or below the higher and lower energetic neutrons respectively. The same behaviour is observed at the energy deposition spectrum in figure 4.19 where some biased counts are above and some below the unbiased case. Specifically from 0-0.2MeV we see that the mean energy of the unbiased spectra, 2.4MeV, dominates the shape of the energy deposition whereas at higher energies the higher energetic neutrons play a vital role.

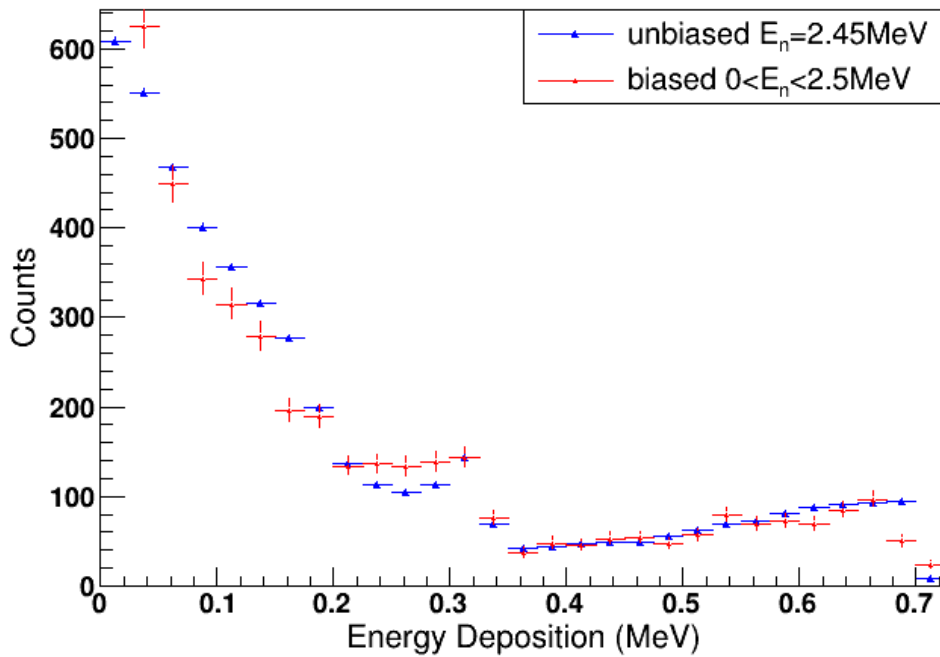
This analysis for the C and Si detector shows the accuracy in which GEANT4 conducts the calculations of interaction emission angles and energies. All the results found can be interpreted through basic kinematics.

For the **SiC** sensor a similar behaviour to the Si was found when conducting the biasing factor analysis, as shown in tables 4.3 and 4.4. The neutron biasing factor could not take high values due to high deviations from the analogue case, so the smallest neutron biasing factor possible $\text{nbf}=2$ for neutron detection with a deviation of 7.03% was used, while for the neutron production $\text{pbf}=900$ was implemented. For these values the spectra shown in figure 4.22 were collected in logarithmic and linear scale.

The energy deposition spectrum for SiC is the combination of C and Si spectra, so similar deviations of the biased protons and the unbiased neutrons are observed as in the previous cases. Some biased counts are above and some below the unbiased, due to the use of a realistic quasi-monoenergetic neutron beam and the contribution of a variety of neutron energies. Also no tail region is observed in higher energies, due to small biasing factor used.



(a)



(b)

Figure 4.22: Biased neutron energy deposition spectrum, with $\text{pbf}=900$ and $\text{nbf}=2$, compared to the unbiased neutrons in linear (a) and logarithmic scale (b) for $50\mu\text{m}$ SiC detector. The blue points derive from a 2.45MeV monoenergetic neutron beam with 10^9 primary neutrons. The red points are formed by 10^9 primary protons interacting with the TiT target and producing a variety of neutrons with mean energy of 2.4MeV as shown in figure 4.9b.

4.3 Comparison of the sensors’ response

Completing the simulations and figuring out, throughout extensive tests, the optimum biasing factor for neutron production and detection, a presentation of each sensor’s response function can be made. Neutron detectors face challenges, mainly due to the small cross section of neutron interactions. The detector’s efficiency must be as high as possible in order to collect the desirable spectrum and it must exhibit low gamma-ray sensitivity in order for the neutron and gamma signals to be distinguishable. These two major factors must be taken into for the correct selection of a neutron detector for the detection of 2.45MeV neutrons for fusion applications.

Neutron interactions with gamma rays for the Si,SiC and C sensor were analysed in section 3.3. While the energy thresholds for SiC and C were clearly at 0.4MeV, for Si there was no clear cut-off for gamma-rays. This leads to the conclusion that for 2.45MeV neutron, Si is not a suitable detector since the gamma and neutron signals will overlap as shown in figure 3.13.

The two remaining contestants are SiC and C and their response function is shown at figure 4.23. Both these materials exhibit excellent electrical and mechanical properties with increased resiliently in extreme environmental conditions, in which 2.45MeV fusion neutrons will be detected. During the simulations a high biasing factor of $nbf=100$ was implemented for the C sensor leading to high statistics while on SiC only $nbf=2$ was used resulting in two orders of magnitude less counts. The chosen biasing factor was affected by the fact that neutron cross section with C is quite smooth, even in these low neutron energies, as shown in figure 4.14 in contrast to SiC which, due to the presence of Si, shows abnormalities as shown in figure 4.15. For 2.45MeV neutron energy both spectra are dominated by neutron elastic scattering. In the following figure the response function for the C and SiC sensor is shown, where the counts are normalised to SiC in order to be able to compare the two materials.

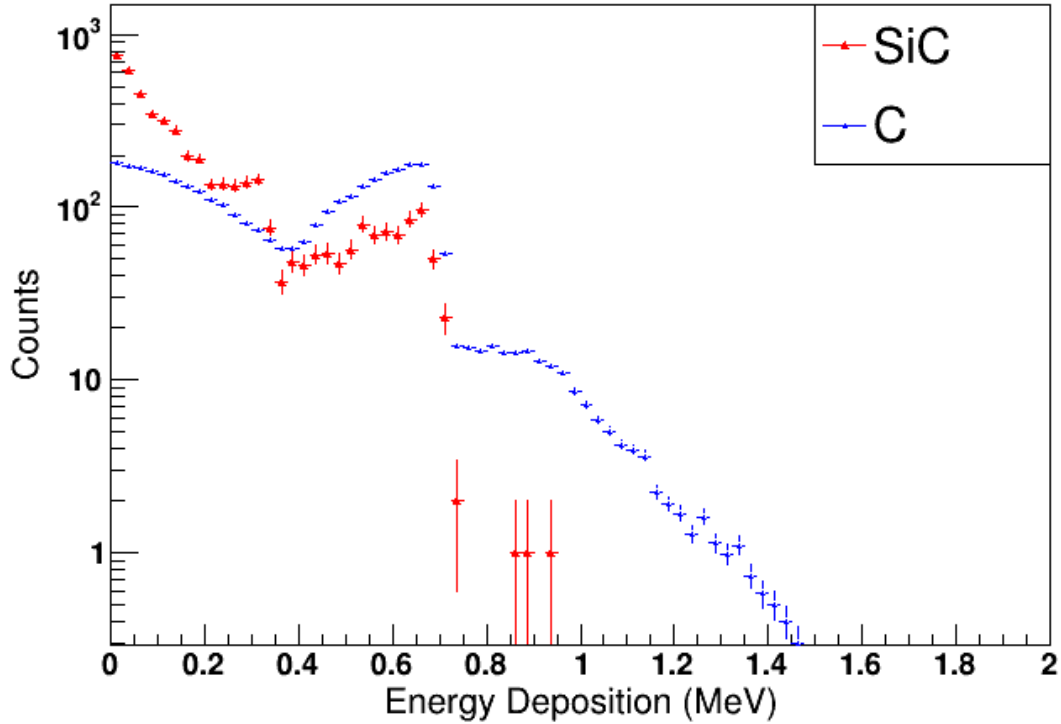


Figure 4.23: Comparison of the normalised response functions of a 50µm C and a SiC sensor to a quasi-monoenergetic neutron beam with mean value 2.405MeV. The neutron production has a biasing factor of pbf=900. The neutron biasing factor for C was nbf=100 while for SiC nbf=2.

We observe that in the small energy regions from 0 to approximately 0.3MeV SiC counts are higher than C, while for higher energies C spectrum is above the SiC. This is caused by the extra presence of Si at the SiC sensor, with positive contribution in the low energy events due to additional Si scattering and negative in the higher energies following the behaviour of the cross section. With the implementation of threshold at 0.4MeV the corrected intrinsic efficiencies and the statistical errors for the two detectors are shown in the table below:

Sensor	Efficiency	Statistical Error
C	0.0812%	0.0019%
SiC	0.0370 %	0.0013%

Table 4.5: Intrinsic efficiency and statistical error for a C and SiC sensor to 2.45MeV neutrons with threshold implementation at 0.4MeV.

We observe the C sensor has almost double efficiency than the SiC due to the threshold implementation. The final efficiency is calculated by taking account the systematic error of the simulation, caused by biasing the neutron detection. For C in the neutron production nbf=100 was used leaving a 4.12% deviation and for SiC nbf=2 with 7.03%.

The number of counts is underestimated, because with biasing implementation the results counts are fewer than the analogue case. The corrected efficiency derives from correcting the entering neutrons with the corresponding factor for the two sensors.

Of course the numbers of the systematic errors shown here is only an estimation. Additional corrections derive from the uncertainty of the shape in the neutron production, because through biasing it is slightly changed with respect to the analogue case. Additional uncertainties arise due to the fact that the analogue case, in which the deviations are calculated, for both the neutron production and detection is not accurate. For biasing the neutron production another biasing simulation of pbf=100 was used as the analogue case, due to the unrealistically long computing time. For biasing the neutron detection a neutron pencil beam was used, which doesn't represent the real angular distribution from (p,n) reactions. Also by the threshold implementation the correction factor for the efficiency will be slightly different, because the deviations were considered isotropic in all the spectrum.

Chapter 5

Conclusions and future perspectives

For the future of thermonuclear fusion, efficient diagnostics systems using the latest technological advances must be installed in the fusion facilities such as ITER, which provide the highest efficiency and resiliency. This work has been conducted to study the C, Si, SiC sensor's response function to 2.45MeV neutrons deriving from D-D fusion. All three detectors exhibit unique characteristics enabling them to be used for neutron applications and in extreme environmental conditions.

Using GEANT4 simulations the neutron interactions of the three materials in void and air were studied, collecting the energy deposition spectrum. The energy ranges and shapes of each spectra are explained with kinematics. Also a review on the gamma ray contamination was made for the typical energies of 0.5MeV, 1MeV and 2MeV, excluding Si due to overlapping signals.

With code development, the neutron production of the I.N.P.P. of the NCSR Demokritos was build, where the experiment will be conducted. The realistic neutron source deriving from (p,n) reactions with a TiT target was simulated and studied. The use of biasing techniques was a necessity, in order to reduce the computing time to a maximum of 8h and increase the produced counts. A number of tests were carried out to determine the behaviour of biasing and the deviations occurred, using a variety of biasing factors and comparing the shapes of the angular distributions with the energy deposition spectra.

Biasing factor has a strong dependence on the cross section, the thickness and the density of the target. The results contain the optimum biasing factor for the neutron production and detection and the final energy deposition spectrum for each sensor. For the C sensor a high biasing factor of 100 was used providing high statistics and efficiency and low deviations. In the SiC sensor large deviations were observed from the analogue case resulting in the use of a lower biasing factor of only 2. Both those materials show promising behaviour in low energy neutron detection.

The future perspectives for the continuation of this work include:

- Developing the GEANT4 code so the input file will be the neutron beam deriving from (p,n) reactions in the TiT target, thus reducing both the systematic error of

the simulation as well as the computing time.

- Development of the realistic geometry of the detector including the metallisation layers, instead of considering the detector as a simple box.
- Verifying the results of the simulation by conducting the experiment at NCSR Demokritos
- Further testing for 14MeV neutrons deriving from the main D-T fusion.

Bibliography

- [1] Kenneth S Krane. *Introductory nuclear physics*. John Wiley & Sons, 1991.
- [2] Mitsuru Kikuchi, Karl Lackner, and Minh Quang Tran. fusion physics. 2012.
- [3] Jacob Eriksson, Sean Conroy, E Andersson Sundén, and Carl Hellesen. calculating fusion neutron energy spectra from arbitrary reactant distributions. *Computer Physics Communications*, 199:40–46, 2016.
- [4] L Bertalot, R Barnsley, MF Direz, JM Drevon, A Encheva, S Jakhar, Y Kashchuk, KM Patel, AP Arumugam, V Udintsev, et al. Fusion neutron diagnostics on iter tokamak. *Journal of Instrumentation*, 7(04):C04012, 2012.
- [5] V Krasilnikov, L Bertalot, R Barnsley, and M Walsh. Neutron detector needs for iter. *Fusion Science and Technology*, 71(2):196–200, 2017.
- [6] 4RB3/6R03 Med Phys 4RA3. Radioisotopes and radiation methodology. https://www.science.mcmaster.ca/radgrad/images/6R06CourseResources/4RA34RB3_Lecture_Note_7_Semiconductor_Detectors.pdf.
- [7] Consuelo Guardiola. Novel silicon sensors for neutron detection. *PhD Dissertation*, 2012.
- [8] DM Mattox. Thin film metallization of oxides in microelectronics. *Thin Solid Films*, 18(2):173–186, 1973.
- [9] DS McGregor, WJ McNeil, SL Bellinger, TC Unruh, and JK Shultis. Microstructured semiconductor neutron detectors. *Nuclear Instruments and Methods in Physics Research Section A: Accelerators, Spectrometers, Detectors and Associated Equipment*, 608(1):125–131, 2009.
- [10] M Angelone. Diamond detectors for neutrons. *IAEA TECDOC SERIES*, page 25, 2020.
- [11] Filippo Nava, Giuseppe Bertuccio, A Cavallini, and E Vittone. Silicon carbide and its use as a radiation detector material. *Measurement Science and Technology*, 19(10):102001, 2008.
- [12] Consuelo Guardiola, Celeste Fleta, Giulio Pellegrini, Francisco Garcia, David Quirion, Joaquin Rodriguez, and Manuel Lozano. Ultra-thin 3d silicon sensors for neutron detection. *Journal of Instrumentation*, 7(03):P03006, 2012.
- [13] Timothy R Garcia, Ashutosh Kumar, Benjamin Reinke, Thomas E Blue, and Wolfgang Windl. Electron-hole pair generation in sic high-temperature alpha particle detectors. *Applied Physics Letters*, 103(15):152108, 2013.

-
- [14] Maurizio Angelone and Claudio Verona. Properties of diamond-based neutron detectors operated in harsh environments. *Journal of Nuclear Engineering*, 2(4):422–470, 2021.
- [15] Christina Weiss. *A CVD diamond detector for (n, a) cross-section measurements*. PhD thesis, TU Vienna, 2014.
- [16] Paul W May. Diamond thin films: a 21st-century material. *Philosophical Transactions of the Royal Society of London. Series A: Mathematical, Physical and Engineering Sciences*, 358(1766):473–495, 2000.
- [17] Markku Tilli, Mervi Paulasto-Krockel, Matthias Petzold, Horst Theuss, Teruaki Motooka, and Veikko Lindroos. *Handbook of silicon based MEMS materials and technologies*. Elsevier, 2020.
- [18] Jérémie Lefèvre, Jean-Marc Costantini, Stéphane Esnouf, and Guillaume Petite. Silicon threshold displacement energy determined by photoluminescence in electron-irradiated cubic silicon carbide. *Journal of Applied Physics*, 105(2):023520, 2009.
- [19] Fausto Franceschini and Frank H Ruddy. *Silicon carbide neutron detectors*. INTECH Open Access Publisher, 2011.
- [20] Gheorghe Brezeanu, Marian Badila, Florin Draghici, Razvan Pascu, Gheorghe Pristavu, Florea Craciunoiu, and Ion Rusu. High temperature sensors based on silicon carbide (sic) devices. In *2015 International Semiconductor Conference (CAS)*, pages 3–10. IEEE, 2015.
- [21] Pavel Kavrigin. *Neutron spectroscopy with sCVD diamond detectors*. PhD thesis, TU Vienna, 2018.
- [22] R Schütz, G Fehrenbacher, JP Biersack, M Wielunski, and W Wahl. Energy deposition distributions caused by fast neutrons in converter type silicon detectors. *Radiation effects and defects in solids*, 157(4):427–444, 2002.
- [23] Jean-Luc Autran and Daniela Munteanu. Electronics reliability assessment of future power fusion machines: neutron interaction analysis in bulk silicon. *Microelectronics Reliability*, 126:114223, 2021.
- [24] O Obraztsova, L Ottaviani, A Klix, T Döring, O Palais, and A Lyoussi. Comparing the response of a sic and a scvd diamond detectors to 14-mev neutron radiation. *IEEE Transactions on Nuclear Science*, 65(9):2380–2384, 2018.
- [25] Sea Agostinelli, John Allison, K al Amako, John Apostolakis, H Araujo, Pedro Arce, Makoto Asai, D Axen, Swagato Banerjee, GJNI Barrand, et al. Geant4—a simulation toolkit. *Nuclear instruments and methods in physics research section A: Accelerators, Spectrometers, Detectors and Associated Equipment*, 506(3):250–303, 2003.
- [26] Geant4 example application with rich features and small footprints. <http://www.physino.xyz/gears/examples/output/>, 2000. Accessed 31/5/2022.
- [27] Geant4 collaboration homepage physicslistguide. https://geant4-userdoc.web.cern.ch/UsersGuides/PhysicsListGuide/html/reference_PL/QGSP_BIC.html, 2021. Accessed 31/5/2022.

- [28] Atomic weights and isotopic compositions with relative atomic masses. <https://www.nist.gov/pml/atomic-weights-and-isotopic-compositions-relative-atomic-masses>, 2021. Accessed 31/5/2022.
- [29] Glenn F Knoll. *Radiation detection and measurement*. John Wiley & Sons, 2010.
- [30] S. Chasapoglou. Experimental study of (n, 2n) reactions in the natural isotopes of iridium. Master's thesis, N.T.U.A, 2017.
- [31] Horst Liskien and Arno Paulsen. Neutron production cross sections and energies for the reactions t (p, n) ^3he , d (d, n) ^3he , and t (d, n) ^4he . *Atomic Data and Nuclear Data Tables*, 11(7):569–619, 1973.
- [32] G. Gkatis. Study of $^3\text{h}(p, n)^3\text{he}$ reaction for neutron production at ncsr demokritos and application at $^{232}\text{th}(n, f)$ reaction. Master's thesis, N.T.U.A, 2021.